

JOINT INVERSION OF GPR AND ER DATA

by

Diego Domenzain

A dissertation
submitted in partial fulfillment
of the requirements for the degree of
Doctor of Philosophy in Geophysics
Boise State University

December 2019

© 2019

Diego Domenzain

ALL RIGHTS RESERVED

BOISE STATE UNIVERSITY GRADUATE COLLEGE

DEFENSE COMMITTEE AND FINAL READING APPROVALS

of the thesis submitted by

Diego Domenzain

Thesis Title: Joint Inversion of GPR and ER Data

Date of Final Oral Examination: 4 December 2019

The following individuals read and discussed the dissertation submitted by student Diego Domenzain, and they evaluated the students presentation and response to questions during the final oral examination. They found that the student passed the final oral examination.

John Bradford Ph.D. Chair, Supervisory Committee

Jodi Mead Ph.D. Co-Chair, Supervisory Committee

Dylan Mikesell Ph.D. Member, Supervisory Committee

Donna Calhoun Ph.D. Member, Supervisory Committee

The final reading approval of the thesis was granted by John Bradford Ph.D., Chair of the Supervisory Committee. The thesis was approved by the Graduate College.

DEDICATION

To all who have believed in me.

ACKNOWLEDGMENT

I would like to thank my advisors John Bradford and Jodi Mead for their firm and stoic leadership. Since I first visited Boise they saw the geophysicist in me before I could see him myself. I will forever be grateful for that.

I would also like to thank my other advisor Dylan Mikesell, for always listening to what I had to say and 9/10 replying with something smart, for welcoming me into his seismic research group, for helping me drag radar antennas, and for sharing expresos, spirits and laughs.

During my stay in TU-Delft I was warmly welcomed by Evert Slob and Dominique Ngan-Tillard. I fondly remember the picnic Dominique and I had surrounded by sheep doing fieldwork in the country side. I am specially thankful to the Geophysics PhD students I met while in TU-Delft. Surrounded by free lattes and Nerf guns, they all made me feel I was home.

My visits to Colorado School of Mines were brightly colored by Adam Mangel's laughter and fruitful discussions. Thank you for being my academic half brother.

Most of the work presented in this work was performed in the Electrical Engineering Department's computational cluster *Kestrel*. Without their parallel electrons at my disposal, I would have finished months later.

Support for this work was given by NSF Computational Mathematics grants NSF-DMS-1418714 and NSF-DMS-1720472, and by the Department of Earth Sciences

Graduate Teaching Assistanship program.

AUTOBIOGRAPHICAL SKETCH

Adventures are lived, not written.

ABSTRACT

Imaging the subsurface can shed knowledge on important processes needed in modern day Human's life such as ground-water exploration, water resource monitoring, contaminant and hazard mitigation, geothermal energy exploration and carbon-dioxide storage. As computing power expands, it is becoming ever more feasible to increase the physical complexity of Earth's exploration methods, and hence enhance our understanding of the subsurface.

We use non-invasive geophysical active source methods that rely on electromagnetic fields to probe the depths of the Earth. In particular, we use Ground penetrating radar (GPR) and Electrical resistivity (ER). Both methods are sensitive to electrical conductivity while GPR is also sensitive to electrical permittivity. We combine both types of data and let the different physical sensitivities of both methods cooperate in order to account for non-uniqueness of the subsurface image.

Full-waveform inversion (FWI) of GPR is a promising technique for recovering permittivity and conductivity of the subsurface by using the full response of the electromagnetic wave. While many advances have been made to FWI by the seismic exploration community, using FWI on GPR surface acquired data is a young and growing field of research. Using the full response of ER data is a more common practice in the geophysical community. However, the spatial resolution of the recovered conductivity lacks high spatial-frequency content due to the inherent sensitivity of

the data.

Fortunately, the sensitivities of GPR and ER are complimentary. GPR is sensitive to conductivity through reflection and attenuation while ER is directly sensitive to conductivity. GPR is sensitive to high spatial-frequency content while ER is sensitive to low spatial-frequency content.

We present a novel non-linear joint inversion that iteratively combines the sensitivities of both GPR and ER surface acquired data. Our algorithm uses both GPR and ER sensitivities in order to effectively alleviate the non-uniqueness of the recovered electrical parameters. We join GPR and ER sensitivities within the same computational grid and without the need of petrophysical relationships. By further assuming structural similarities between permittivity and conductivity, we are able to relax a priori assumptions about the subsurface and accurately recover parameters in regions where the GPR data has a signal-to-noise ratio close to one. Furthermore, assuming a good initial model is available our algorithm makes no assumption of the underlying geometry.

The demanding computing requirements of GPR-FWI entail an unfeasible amount of memory for existing ER inversion methods. This is due to the very fine discretization of the subsurface required by GPR-FWI. We develop a 2.5d ER adjoint method inversion that is capable of recovering accurate subsurface conductivity from field data and relaxes the amount of required memory. We test our method on field data from an alluvial aquifer site and find agreeable results with existing measurements in the literature. Having feasible computational methods for both GPR and ER inversions is an important step for using our joint inversion algorithms on field data.

TABLE OF CONTENTS

DEDICATION	iv
ACKNOWLEDGMENT	v
AUTOBIOGRAPHICAL SKETCH	vii
ABSTRACT	viii
LIST OF FIGURES	xiv
LIST OF TABLES	xxi
LIST OF ABBREVIATIONS	xxiii
1 INTRODUCTION	1
1.1 Preliminaries	6
1.2 Joining sensitivities of full-waveform GPR and ER data	7
1.3 Enhancing low frequency and exploiting structural similarities	7
1.4 Inversion of 2.5D electrical resistivity data using the adjoint method .	8
2 PRELIMINARIES	9
2.1 Introduction	9
2.2 Joining two sensitivities	10

2.3	The envelope of a waveform	12
2.4	Structural constraints	14
3	JOINING SENSITIVITIES OF FULL-WAVEFORM GPR AND ER DATA	17
3.1	Introduction	18
3.2	Inversion methods	25
3.2.1	GPR inversion	25
3.2.2	ER inversion	32
3.3	Joint inversion	35
3.4	Examples	42
3.4.1	Subsurface models	42
3.4.2	Data acquisition	46
3.4.3	Noise	47
3.4.4	GPR inversions	47
3.4.5	ER inversions	48
3.4.6	Joint inversions	48
3.5	Conclusions	59
4	ENHANCING LOW FREQUENCY AND EXPLOITING STRUCTURAL SIMILARITIES	63
4.1	Introduction	64
4.2	GPR and ER forward models and inversions	67
4.2.1	Ground penetrating radar	68
4.2.2	Electrical resistivity	69
4.2.3	GPR inversion	69

4.2.4	ER inversion	71
4.3	Joint inversions	72
4.3.1	Joint inversion of ER and GPR data	72
4.3.2	Joint inversion of GPR envelope and ER data	75
4.3.3	Joint inversion with cross-gradients	77
4.3.4	Joint inversion of GPR envelope and ER data with cross-gradient	84
4.4	Subsurface simulations	87
4.4.1	Experiments	89
4.4.2	Results	93
4.5	Discussion	107
4.6	Conclusions	112
5	INVERSION OF 2.5D ELECTRICAL RESISTIVITY DATA USING THE ADJOINT METHOD	114
5.1	Introduction	115
5.2	Methods	119
5.2.1	ER 2D forward model	119
5.2.2	Inversion of 2D ER data	120
5.2.3	ER 2.5D forward model	121
5.2.4	Inversion of 2.5D ER data	123
5.3	Examples	129
5.3.1	Synthetic data example	129
5.3.2	Field data example	132
5.4	Conclusions	137

6 CONCLUSIONS	142
6.1 Discussion	145
REFERENCES	147
APPENDIX A OPTIMALLY PERTURBING	162
APPENDIX B ER GRADIENT	163
APPENDIX C ENVELOPE GPR GRADIENT	166
APPENDIX D MINIMIZING Θ_τ	169
APPENDIX E INITIAL MODELS FOR THE SYNTHETIC ALLUVIAL AQUIFER	172
APPENDIX F FOURIER COEFFICIENTS FOR 2.5D TRANSFORM . . .	176

LIST OF FIGURES

1.1	Field acquisition, a and b , and examples of their respective observed data, c and d	2
2.1	Optimizing individual objective functions in a and b . The joint objective function in c . The big blue dot indicates the initial model parameters, the yellow dot the recovered parameters, and the red star the true solution.	12
2.2	Waveform data (solid line) and its envelope transform (dashed line) in time a and in the frequency domain b in black the data and in grey the envelope.	13
2.3	Structural transformation of the parameters keeping black constant in a , and blue constant in b . The dashed lines indicate the original parameters.	15
3.1	Frequency dependent conductivity and attenuation coefficients of various earth materials. Solid and dashed lines represent (real) effective and DC conductivity respectively. In a and b are low conductivity materials where GPR data has a large signal-to-noise ratio. In c and d are high conductivity materials where GPR data has a low signal-to-noise ratio.	24

3.2	Algorithms for computing the updates $\Delta\boldsymbol{\varepsilon}$ and $\Delta\boldsymbol{\sigma}_w$	31
3.3	Algorithm for computing the update $\Delta\boldsymbol{\sigma}_{dc}$	36
3.4	Inversion algorithms for a GPR and b ER.	37
3.5	Algorithm for computing the update $\Delta\boldsymbol{\sigma}$ as explained in Section Joint Inversion	43
3.6	Diagram of weights a_w and a_{dc} as a function of iterations. An initial value for a_{dc} is chosen following condition (0) . If a_{dc} decreases over iterations, or Θ_{dc} increases, condition (1) , or (3) , are activated to increase a_{dc} . Once a_{dc} reaches the value 1, a_w is forced to steadily decrease with condition (2) . If $\Theta_{w,\sigma}$ increases over iterations, condition (4) is activated and a_w is increased but regulated by condition (2) . . .	44
3.7	Joint inversion algorithm as explained in Section Joint Inversion . .	45
3.8	Subsurface models used for our inversions. The size of the box is 1×1 m. a The permittivity background, bottom reflector and box have values of 4, 9 and 6 respectively. The conductivity background and box have values of 1 and 4 mS/m for the low conductivity b and 4 and 20 mS/m for the high conductivity c respectively. An example of GPR receivers and source are depicted in green and red in b and ER electrodes are depicted in green in c	51
3.9	GPR data for one source noise free and with added noise.	52
3.10	a All ER data noise free and the clusters used for adding noise depicted with symbols +, •, and ×. b Pseudo-section of a dipole-dipole survey noise free and c with added noise.	52

3.11	Recovered permittivity for the low-conductivity scenario with just GPR data a and with GPR and ER data b .	53
3.12	Recovered permittivity for the high-conductivity scenario with just GPR data a and with GPR and ER data b .	54
3.13	Recovered low conductivity using a just GPR data, b just ER data, and c both GPR and ER data. Each inversion was run for 50 iterations.	55
3.14	Recovered high conductivity using a just GPR data, b just ER data, and c both GPR and ER data. Each inversion was run for 50 iterations.	56
3.15	Update weights history over iterations for the low-conductivity scenarios a and normalized objective functions history over iterations d .	57
3.16	Update weights history over iterations for the high-conductivity scenarios a and normalized objective functions history over iterations d .	58
4.1	Inversion algorithm for Joint and JEN. We differentiate Joint and JEN by how we compute $\Delta\sigma_w$ and $\Delta\epsilon$.	73
4.2	Qualitative optimal shape for weights throughout iterations for all inversion schemes (Joint, JEN, JOIX and JENX).	74
4.3	Inversion algorithm for JOIX and JENX. We differentiate JOIX and JENX by how we compute $\Delta\sigma_w$ and $\Delta\epsilon$.	79
4.4	Illustration of cross-gradient possibilities. Given estimates ϵ and σ in a and b , Θ_τ is minimized by updating both ϵ and σ in c and d , updating ϵ and keeping σ fixed in e , and updating σ keeping ϵ fixed in f . The dashed circles are constant markers for the widths and centers of the Gaussian shapes in the given estimates of ϵ and σ .	80

4.5	True permittivity a and conductivity for the low b and high c conductivity scenario. In a , GPR source and receivers layout for line # 7. In b , all electrodes used for our ER experiment.	88
4.6	Synthetic alluvial aquifer true and initial parameters. True a and initial b permittivities. True c and initial d conductivities. The cyan lines represent boreholes B1, B2 and B3 from left to right.	89
4.7	GPR shot gather # 7 of the low and high-conductivity scenarios and their respective best recovered parameters as given by Figures 4.10-4.11 d for the low-conductivity and 4.12-4.13 d for the high-conductivity scenario. Amplitudes are clipped to 1.5% of the maximum amplitude in the data.	91
4.8	ER data of the low a and high b conductivity scenarios and their respective best recovered parameters.	92
4.9	Residuals of GPR shot-gather #7 for the synthetic alluvial aquifer. Residual of initial model and observed in a , and of recovered and observed in b . Recovered data correspond to the JOIX method. Amplitudes are clipped to 1.5% of the maximum amplitude in the data. . .	93
4.10	Recovered permittivity with low conductivity using Joint in a , JEN in b , JOIX in c and JENX in d	94
4.11	Recovered low conductivity using Joint in a , JEN in b , JOIX in c and JENX in d	95
4.12	Recovered permittivity with high conductivity using Joint in a , JEN in b , JOIX in c and JENX in d	98

4.13 Recovered high conductivity using Joint in a , JEN in b , JOIX in c and JENX in d .	99
4.14 Recovered permittivity for the synthetic alluvial aquifer using Joint in a , JEN in b , JOIX in c and JENX in d .	102
4.15 Recovered conductivity for the synthetic alluvial aquifer using Joint in a , JEN in b , JOIX in c and JENX in d .	103
4.16 Recovered permittivity of the synthetic alluvial aquifer using the JOIX method on boreholes B1, B2 and B3 in a , b and c respectively. True is solid black and initial model is dashed blue.	105
4.17 Recovered conductivity of the synthetic alluvial aquifer using the JOIX method on boreholes B1, B2 and B3 in a , b and c respectively. True is solid black and initial model is dashed blue.	106
4.18 Synthetic alluvial aquifer data. Observed a and recovered b GPR data for shot-gather #7. In c observed and recovered ER data. Recovered data correspond to the JOIX method. Amplitudes are clipped to 1.5% of the maximum amplitude in the data.	107
4.19 Inversion weights of the synthetic alluvial aquifer using the JOIX method. In a values of weights a_w and a_{dc} over iterations. In b objective function values for $\Theta_{w,\sigma}$ and Θ_{dc} .	111
5.1 Memory needed to compute ER sensitivities as a function of domain size. In gray, using the Hessian of the objective function. In black, using our 2.5D approximation.	118
5.2 Algorithm for computing the 2.5D electric potential given a source s and conductivity σ .	122

5.3	Algorithm for finding the 2.5D gradient \mathbf{g}	125
5.4	2.5d inversion algorithm.	128
5.5	True \mathbf{a} , recovered \mathbf{b} and appraised \mathbf{c} conductivity for the synthetic example. The dashed cyan line in \mathbf{a} represents a borehole location. The dashed black line (in \mathbf{b} and \mathbf{c}) represents the contour of the cylinder.	130
5.6	True (black) and recovered (red) conductivity at the center borehole for the synthetic example. The dashed gray line shows the cut-off for our appraised solution.	131
5.7	Geographic location of the Boise Hydrological Research Site (BHRs). The red dots denote the existing boreholes. Our survey line crossed boreholes B5, A1 and B2 as shown by the green line.	133
5.8	Dipole-dipole pseudo section with a-spacing equal to 1m from the BHRs.	134
5.9	Wenner pseudo-section of the BHRs.	135
5.10	Recovered conductivity from the BHRs with topographic correction. The dashed cyan line represents the water table depth as measured on site (1m deep). The solid cyan lines represent the borehole positions.	138
5.11	Observed vs recovered ER data acquired at the BHRs.	138
5.12	Normalized recovered conductivities (red) and borehole neutron porosity (black) at borehole locations in the BHRs. The dashed gray line shows the cut-off for our appraised solution.	139
5.13	Recovered ER (with our method - in red) and capacitive conductivities (black) at borehole locations in the BHRs. The dashed gray line shows the cut-off for our appraised solution.	140

LIST OF TABLES

3.1	Frequency dependent and DC conductivities at 250MHz given by the Cole-Cole model. Most earth materials present an increase of at most 5 between DC and (real) effective conductivity.	25
3.2	Reference for the notation used in the discretized inverse problems. Symbols common in both GPR and ER experiments are stripped from their subscripts to avoid clutter.	38
3.3	Parameters for our joint inversions that were found empirically and remained fixed throughout the inversions. An increase in h favors $\Delta\sigma_{dc}$ more than $\Delta\sigma_w$. Conversely, a decrease in h favors $\Delta\sigma_w$ more than $\Delta\sigma_{dc}$	44
3.4	Inversion parameters used for the low and high-conductivity scenario.	46
3.5	Ratio of maximum zero-lag cross-correlation between recovered and observed parameters for the low and high-conductivity scenarios. Closer to 1 is better. The joint inversion outperforms the GPR and ER recovered conductivities.	50
4.1	Reference for the notation used in the discretized inverse problems. Symbols common in both GPR and ER experiments are stripped from their subscripts to avoid clutter.	70
4.2	Inversion parameters for the low-conductivity scenario.	96

LIST OF ABBREVIATIONS

BHRS Boise Hydrological Research Site

ER Electrical resistivity

FWI Full waveform inversion

GPR Ground penetrating radar

JEN Joint and envelope inversion

JENX Joint, envelope and cross-gradients inversion

Joint Joint inversion

JOIX Joint and cross-gradients inversion

CHAPTER 1:

INTRODUCTION

Electrical properties of the subsurface such as permittivity and conductivity, hold relevant information about the subsurface. Applications of such properties can be found in water resource monitoring, hazard mitigation, geothermal energy exploration and carbon-dioxide storage. With the environmental strain climate change is causing in the water cycle and the increased concentration of carbon-dioxide in the atmosphere, the importance of these applications for every-day human life is paramount. Understanding the shallow subsurface ($\approx 100\text{m}$ in depth) structure of our planet can help mitigate and prevent these clear and present dangers to our way of life.

GPR is sensitive to electrical permittivity through reflectivity and velocity, and also sensitive to electrical conductivity through reflectivity and attenuation. ER is directly (and only) sensitive to electrical conductivity. Despite the broad range of applications for mapping electrical properties of the subsurface using GPR and ER methods, often a choice has to be made in using either method because of their contrasting sensitivities.

Fortunately GPR and ER data have a complimentary relationship. GPR is sensitive to what ER is not (permittivity) and ER is directly sensitive to what GPR is only sensitive by weak reflections and attenuation (conductivity). Moreover, GPR data gives a higher space-frequency resolution image of the media of interest in contrast

with the lower space-frequency image obtained with the ER data. Figure 1.1 gives an example of field acquisition and observed data.

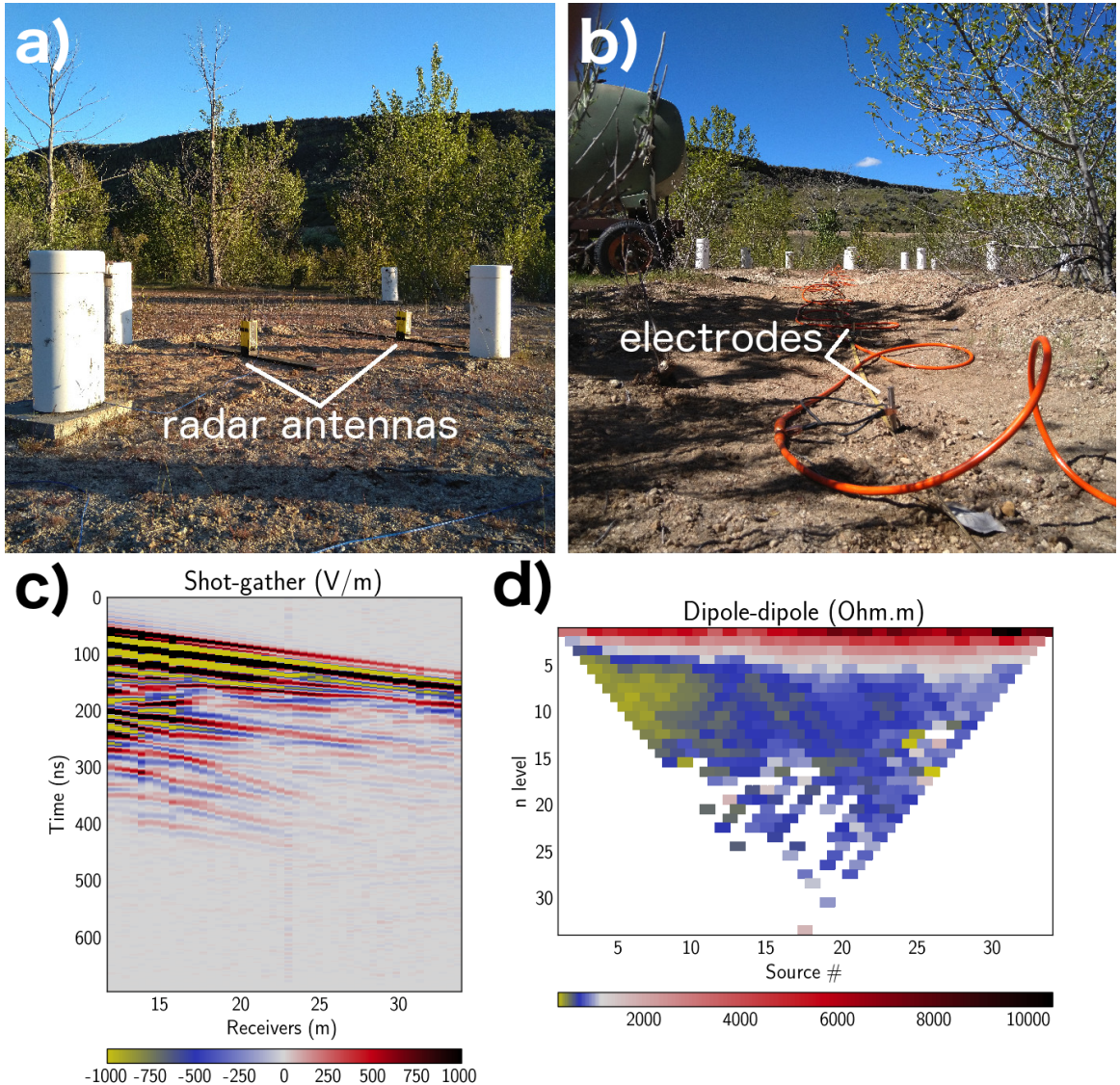


Figure 1.1: Field acquisition, a and b, and examples of their respective observed data, c and d.

Joining data from different types of geophysical imaging methods holds the promise of reducing the non-uniqueness of characterizing subsurface material properties (Ogunbo

et al., 2018). Different approaches coupling the subsurface material properties have been developed in order to join different types of sensitivities (Moorkamp, 2017). Broadly, the material properties coupling can be done via geologic structure, where different material properties are assumed to share the same geometry (Haber & Oldenburg, 1997; Gallardo & Meju, 2003; Haber & Gazit, 2013), or linked by petrophysical relationships (Ghose & Slob, 2006). More specifically, Linde *et al.* (2006) use GPR and ER cross-hole data assuming structural similarities of electromagnetic properties and simplifying the physics of the GPR to only use travel times.

We have developed a full-physics, multi-parameter, geometry free, non-linear joint inversion algorithm that accounts for both permittivity and conductivity of the subsurface using GPR and ER surface-acquired data. Our joint inversion algorithm uses the adjoint method (commonly referred to as *full-waveform inversion* in the case of radar) for both GPR and ER data sensitivities. It accounts for both permittivity and conductivity of the subsurface at each pixel of our discretized subsurface – a two-dimensional slice in depth. Our algorithm does not rely on petrophysical relationships between permittivity and conductivity and we apply no additional regularization to the inversion beyond the joint objective function itself and the cross-gradients constraint.

Since its original introduction in the acoustic regime (Tarantola, 1984), Full waveform inversion (FWI) has been widely used in the seismic community. Due to the full use of the wavefield in the inversion, the recovered parameters of the subsurface are greatly improved compared with methods that only account for travel-time. By using the full wavefield to compute the data sensitivities, FWI inherently takes into account all wave phenomena such as reflections, refractions, waveguides, and multiples that

travel-time methods struggle to resolve. Therefore, by using FWI we can significantly enhance our ability to characterize the subsurface.

However promising, FWI holds many challenges for retrieving good quantitative models of the subsurface. Using the full wavefield makes the inversion process highly non-linear and it is easy to misinterpret local minima as solutions. In the context of seismic FWI, many efforts have been made to relieve the ailments that make the problem ill-posed. For example, it is well known that low frequencies in the waveform data help the inversion avoid local minima (Virieux & Operto, 2009; Baeten *et al.*, 2013), so Bozdağ *et al.* (2011) and Liu & Zhang (2017) have also helped reduce this problem. In Bozdağ *et al.* (2011), the authors propose using the analytic signal of the observed waveform in order to isolate the instantaneous phase and amplitude (i.e. envelope) information of the data and modify the FWI objective function accordingly. In Liu & Zhang (2017) the authors join first arrival travel-time with early arrival envelope data to build a rich low spatial-frequency initial velocity model that is then used in the FWI routine. Both works find that the low frequency content of the envelope waveform data is good for enhancing the low frequency spatial content of the recovered velocity.

Previous work on GPR-FWI has mostly focused on transillumination data (Ernst *et al.*, 2007a; Meles *et al.*, 2010; Klotzsche *et al.*, 2014; Gueting *et al.*, 2017), and only recently Lavoué *et al.* (2014) on surface-acquired data. Using GPR-FWI for surface-acquired data in the presence of strong attenuative media remains an important challenge (Lavoué *et al.*, 2014). In this work we use the envelope waveform data of GPR and further join it with ER data to alleviate low spatial frequencies in both electrical permittivity and conductivity.

Joining data from different types of geophysical imaging methods holds the promise of reducing the non-uniqueness of characterizing subsurface material properties (Ogunbo *et al.*, 2018). Different approaches coupling the subsurface material properties as well as different algorithmic workflows have been developed in order to join different types of sensitivities (Moorkamp, 2017). Broadly, the material properties coupling can be done via geologic structure, where different material properties are assumed to share the same geometry (Haber & Oldenburg, 1997; Gallardo & Meju, 2003; Haber & Gazit, 2013), or linked by petrophysical relationships (Ghose & Slob, 2006). Our approach for joint inversion is able to assume or ignore structural properties and in neither do we use petrophysical relationships since the GPR and ER data are physically linked through conductivity with Maxwell's equations. We are able to increase the amplitude and spatial frequency resolution of the inverted electrical properties in a joint inversion compared with individual inversions of surface-acquired data. In this way the GPR and ER optimization problems effectively regularize each other while honoring the physics.

Although in this work we focus specifically on GPR and ER data, there are other geophysical exploration methods that have complementary sensitivities and share physical parameters in their governing physics, i.e. gravity and elastic waves, temperature and elastic waves (and gravity), magnetotellurics and electrical resistivity (and radar), controlled source electromagnetics and electrical resistivity (and radar). Through our joint inversion of GPR and ER data we have demonstrated how using the adjoint method for computing data sensitivities can make use of the full physical response in the data to cooperatively enhance the solution of the physical parameters. In an even broader scale, we have demonstrated how different types of data that are

inherently linked by their governing partial differential equations can be joined in a non-linear inverse method to improve their individual sensitivities.

In order to develop our joint inversion algorithm, we have written a self-contained code with both GPR and ER forward models, as well as all inversion routines. Because of the heavy computational burden of using the adjoint method on Maxwell's equations, our code is best suited for parallel implementation using high performance computing techniques.

This dissertation develops the theory and implementation of our joint inversion. We present synthetic examples with varying levels of difficulty to better illustrate the attributes and caveats of our methods. In order to facilitate the understanding of our inversion algorithms, we present an intuitive explanation of our methods with limited detail in Chapter 2. Our joint inversion algorithm itself is broken down in three chapters. Chapter 3 builds the foundations of our joint update. Chapter 4 enhances the low spatial-frequency and accuracy of our solution by using the envelope of the GPR data and the cross-gradients constraint. Chapter 5 develops a low storage 2.5D ER inversion scheme tested with field data.

1.1 Preliminaries

Our joint inversion is based on three ideas, (i) use the physics in Maxwell's equations to join the sensitivities of GPR and ER data, (ii) transform the GPR data to exploit low frequency content, and (iii) assume the subsurface electrical parameters are structurally similar. We give simple one-dimensional examples for each of these three ideas with minimal implementation details. Idea (i) is thoroughly explored in the second chapter. Ideas (ii) and (iii) are fully implemented in the third chapter.

1.2 Joining sensitivities of full-waveform GPR and ER data

We first compute sensitivity updates separately for both the GPR and ER data using the adjoint method, and then we sum these updates to account for both types of sensitivities. The sensitivities are added with the paradigm of letting both data types always contribute to our inversion in proportion to how well their respective objective functions are being resolved in each iteration. Our algorithm makes no assumption of the subsurface geometry nor structural similarities between parameters with the caveat of needing a good initial model. We find that our joint inversion outperforms both GPR and ER separate inversions and determine that GPR effectively supports ER in regions of low conductivity while ER supports GPR in regions with high conductivity (i.e. strong attenuation).

1.3 Enhancing low frequency and exploiting structural similarities

We propose three non-linear inverse methods for recovering electrical conductivity and permittivity of the subsurface by joining GPR and electrical resistivity (ER) data acquired at the surface. All methods use ER data to constrain the low spatial-frequency of the conductivity solution. The first method uses the envelope of the GPR data to exploit low frequency content in full-waveform inversion and does not assume structural similarities of material properties. The second method uses cross-gradients to manage weak amplitudes in the GPR data by assuming structural similarities between permittivity and conductivity. The third method uses both the envelope

of the GPR data and the cross-gradient of the model parameters. By joining ER and GPR data, exploiting low frequency content in the GPR data, and assuming structural similarities between electrical permittivity and conductivity we are able to recover subsurface parameters in regions where the GPR data has a signal-to-noise ratio close to one.

1.4 Inversion of 2.5D electrical resistivity data using the adjoint method

We present a 2.5D inversion algorithm of electrical resistivity (ER) data that handles realistic field experiments using low storage requirements. We use the adjoint method directly in the discretized Maxwell's steady state equation that governs the physics of the ER data. In doing so we make no finite difference approximation on the Jacobian of the data and avoid the need to store large and dense matrices. Rather, we exploit matrix-vector multiplication of sparse matrices and find satisfactory results using gradient descent for our inversion routine without having to resort to the Hessian of the objective function. Moreover, our algorithm does not need extra padding of the domain since it robustly accounts for boundary conditions in the subsurface. Given the low storage requirements, our algorithm can be used for joint inversion with other geophysical methods that may impose finer grid constraints (and larger memory requirements) without the need of interpolating the sensitivities of the domain. We tested our algorithm on field data acquired in an alluvial aquifer and were able match the recovered conductivity to borehole observations.

CHAPTER 2:

PRELIMINARIES

Our joint inversion algorithms presented in Chapter 3 and Chapter 4 regularize the inverse problem of finding electrical parameters of the subsurface by (i) transforming the sensitivities of the data, (ii) transforming the GPR data, and (iii) transforming the model parameters. Each of these three types of transform (i) use the inherent dependence of conductivity in both the GPR and ER data given by Maxwell's equations, (ii) exploit low frequency content of the GPR data by using the envelope of the waveform, and (iii) iteratively exchange structural information of the electrical parameters using the cross-gradients constraint. We observe that (i) reduces the non-uniqueness of the inverse problem by eliminating local minima present in individual inversions, (ii) enhances low-frequency information of the waveform data, and (iii) enhances spatial frequency resolution of the recovered parameters.

2.1 Introduction

Regularizing the objective function is necessary when the observed data offer a non-unique solution to the inverse problem. In the case of geophysical methods, it is often the case that not enough data coverage is available to constrain a unique solution. For differentiable objective functions, the non-uniqueness of the inverse problem arises when the solution converges to a local minima. In any real valued function, as is the

case for a typical objective function, local minima arise when the function is non-linear (of degree larger than two).

Different methods exist for regularizing the objective function, i.e. reducing the non-uniqueness of the inverse problem. Describing all of them is well beyond the scope of this work. However, we mention that most approaches rely on introducing a priori knowledge of the solution (Haber & Oldenburg, 1997; Gallardo & Meju, 2003), or modifying the data to locally reduce the non-linearity of the objective function (Bunks *et al.*, 1995; Pratt *et al.*, 1998; Meles *et al.*, 2012). In this work we use both approaches and develop a new method: directly enhancing the sensitivities of different types of data that are sensitive to the same parameter.

2.2 Joining two sensitivities

We present a simplified example of the GPR and ER inversions. Assume our forward models in discrete notation are of the form,

$$\begin{aligned} \mathbf{L}_w \mathbf{u}_w &= \mathbf{s}_w \\ d_w &= \mathbf{M}_w \mathbf{u}_w \\ \mathbf{L}_{dc} \boldsymbol{\varphi} &= \mathbf{s}_{dc} \\ d_{dc} &= \mathbf{M}_{dc} \mathbf{u}_{dc} \end{aligned} \tag{2.1}$$

where \mathbf{s}_w and \mathbf{s}_{dc} are 2×1 vectors (assumed known), and \mathbf{M}_w and \mathbf{M}_{dc} are linear operators that collapse the dimension of the fields \mathbf{u}_w and $\boldsymbol{\varphi}$ (of dimensions 2×1) onto the data d_w and d_{dc} (both scalars). Both \mathbf{L}_w and \mathbf{L}_{dc} are different 2×2 matrices that depend non-linearly on both σ_w and σ_{dc} (both scalars). For only this chapter,

we will write

$$\boldsymbol{\sigma} = \begin{bmatrix} \sigma_w \\ \sigma_{dc} \end{bmatrix}, \quad (2.2)$$

a 2×1 vector. We denote the observed data d_w^o and d_{dc}^o .

Let the objective functions for d_w^o and d_{dc}^o be respectively,

$$\begin{aligned} \Theta_w(\boldsymbol{\sigma}; d_w^o) &= \|d_w - d_w^o\|_2^2, \\ \Theta_{dc}(\boldsymbol{\sigma}; d_{dc}^o) &= \|d_{dc} - d_{dc}^o\|_2^2. \end{aligned} \quad (2.3)$$

We define the joint objective function that depends both on d_w^o and d_{dc}^o as,

$$\Theta(\boldsymbol{\sigma}; d_w^o, d_{dc}^o) = \Theta_w + \Theta_{dc}. \quad (2.4)$$

We use gradient descent for inverting all objective functions (Θ_w , Θ_{dc} , and Θ) with respect to $\boldsymbol{\sigma}$. The path of parameter iterations over the different objective function surfaces are plotted in Figure 2.1. In this simplified example, we see that the surfaces Θ_w and Θ_{dc} exhibit non-uniqueness of the solution $\boldsymbol{\sigma}$ as entire level curves of local minima.

Although the gradient descent algorithm finds the true descent direction, it fails to converge to the true solution. This is due to the strong non-linearity of the objective functions Θ_w and Θ_{dc} : a first-order inverse method does not capture the correct descent direction.

However, the surface Θ has been relieved of these local minima curves. In this case, the gradient descent algorithm can correctly traverse the parameter space and find the true solution. This is due to the local descent direction being accurately

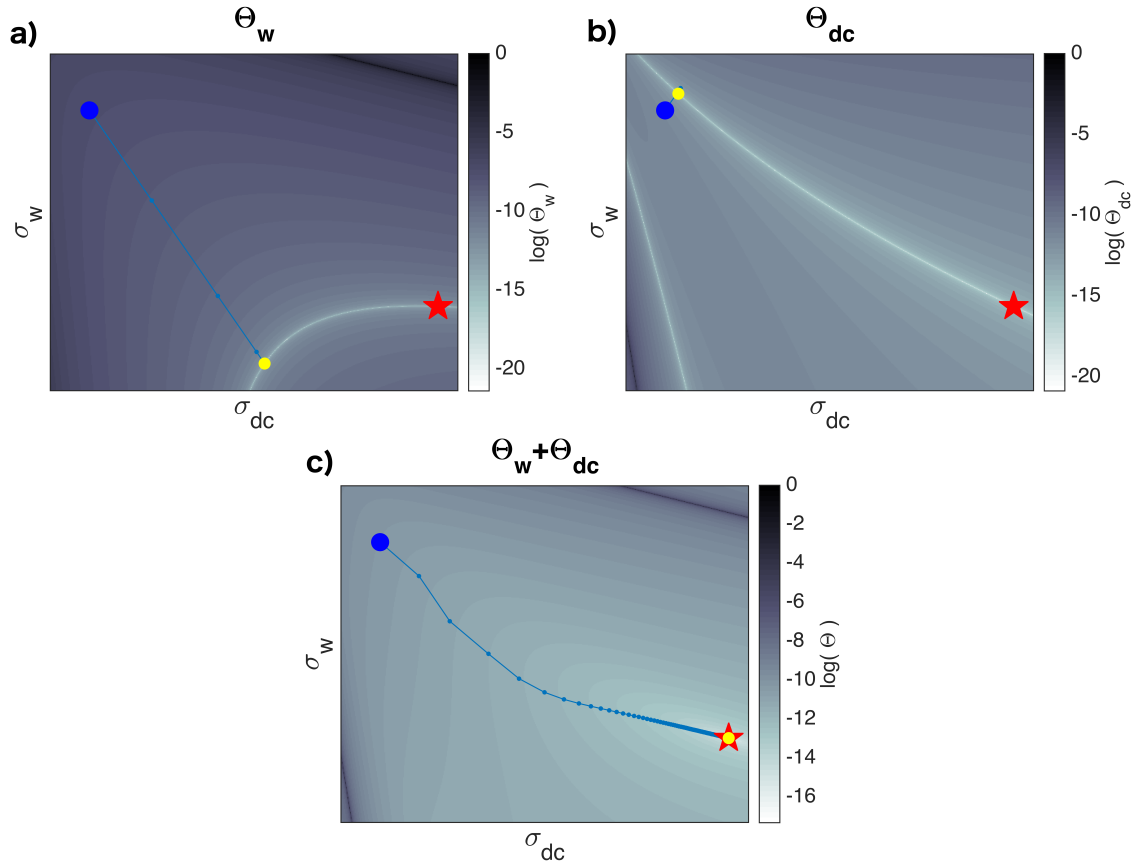


Figure 2.1: Optimizing individual objective functions in a and b. The joint objective function in c. The big blue dot indicates the initial model parameters, the yellow dot the recovered parameters, and the red star the true solution.

approximated by a first-order inverse method. Hence, we have reduced the local non-linearity of inverting Θ_w and Θ_{dc} by considering Θ instead.

2.3 The envelope of a waveform

In the context of FWI, low frequency content in the data is essential for avoiding local minima in the objective function (Bunks *et al.*, 1995; Pratt *et al.*, 1998; Meles *et al.*, 2012; Bozdağ *et al.*, 2011). Physically, convergence to a local minima can be

manifested when the residual of synthetic vs observed data is small, but the recovered parameters are such that the synthetic data is off by a cycle or more with respect to the observed data. This phenomena has been coined as *cycle skipping* in the literature.

Enhancing the low frequency information in the waveform data can be a powerfull tool to mitigate local minima in the solution. We use the approach of Bozdağ *et al.* (2011), where the authors use the envelope of the waveform in a modified FWI scheme. The full discussion of this approach is discussed in Chapter 4. In this section we present an example of a single waveform and its envelope.

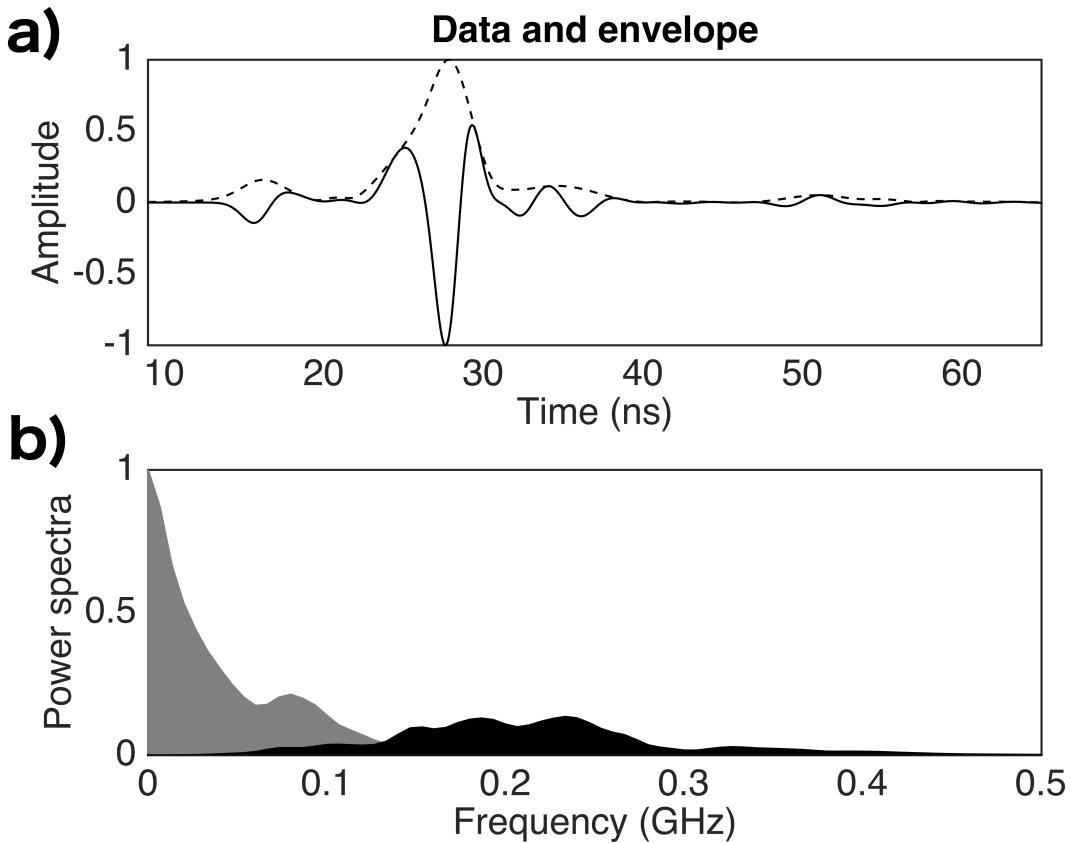


Figure 2.2: Waveform data (solid line) and its envelope transform (dashed line) in time a and in the frequency domain b in black the data and in grey the envelope.

Figure 2.2 displays an observed trace and its envelope. In Figure 2.2-**b** we see that the power spectra of the envelope is more heavily weighted towards low frequencies when compared to the observed data. Furthermore, we note that the DC component in the power spectra of the envelope can be intuitively explained by the lack of oscillations in the time domain. Analytically, we can deduce this DC component by approximating the envelope in time as a linear combination of gaussian functions and subsequently use the properties of the Fourier transform (i.e. linearity, time-shift and the gaussian having a gaussian as its Fourier transform).

Although the frequency content of the data changes under the envelope, this approach does not impose a priori information on the inversion. As shown in Chapter 4, this approach improves low spatial frequency of the recovered parameters.

2.4 Structural constraints

Assuming structural similarities of the subsurface parameters between two model parameters can be a powerfull tool for relieving the non-uniqueness of the inverse problem Haber & Oldenburg (1997); Gallardo & Meju (2003); Ogunbo *et al.* (2018). The cross-gradients constraint is a usual approach for informing two different parameters of their respective structure. Since the geophysical methods sensitive to either of the two parameters need not be the same, assuming structural similarities can benefit from different physical sensitivities.

Commonly, the implementation of the cross-gradients constraint modifies both parameters by weighing their structures equally. However, since different geophysical methods offer different sensitivities to material properites, this approach does not take into account the stronger sensitivity in the data towards one parameter over the other. Our inversion approach is able to more heavily weigh the structure of one

parameter over the other. For a full discussion of this idea see Chapter 4. In this section we present a simple one dimensional example.

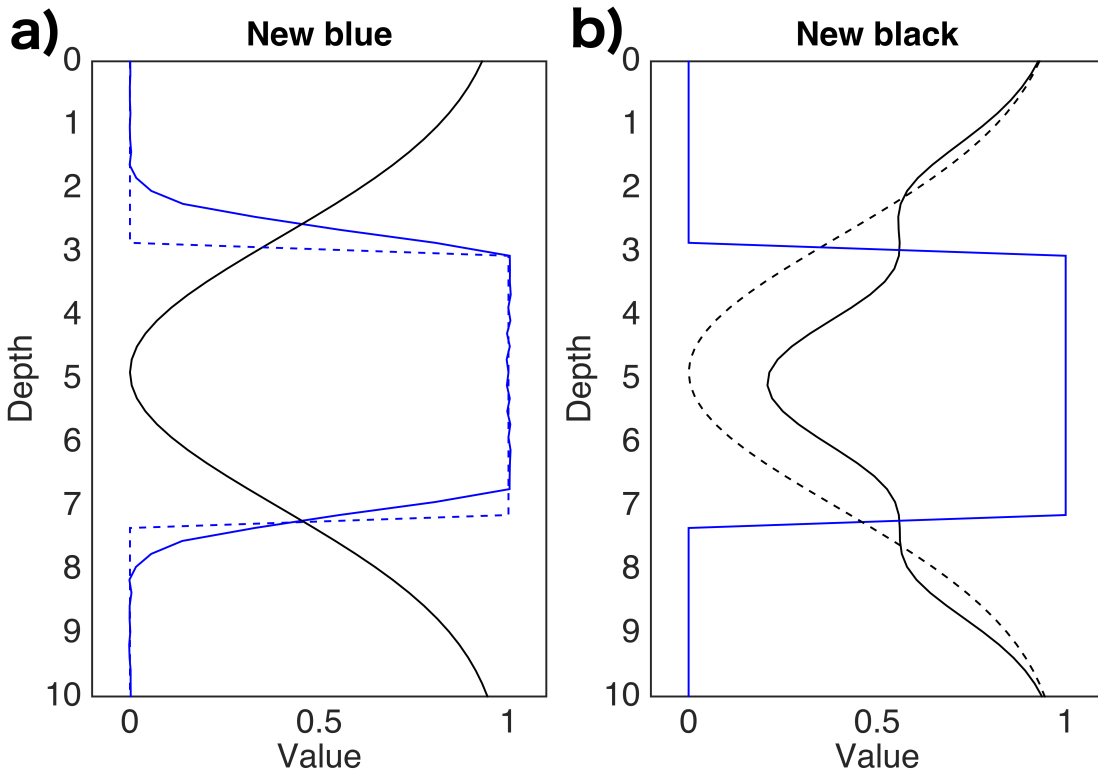


Figure 2.3: Structural transformation of the parameters keeping black constant in a, and blue constant in b. The dashed lines indicate the original parameters.

Consider two different one-dimensional parameters given by two different physical sensitivities as shown in Figure 2.3. The sensitivity towards the blue parameter is blocky, while the sensitivity towards the black parameter is smooth. If we wish to imprint the structure of the black parameter onto the blue, the blue parameter becomes smoother (Figure 2.3-a). Conversely, if we wish to imprint the structure of the blue parameter onto the black, the black parameter exhibits changes where the sharp contrasts of the blue parameter are (Figure 2.3-b).

As shown in (Figure 2.3, our approach is capable of importing spatial frequency content between the parameters. In the data domain, this means we are enhancing the physical sensitivity of the geophysical methods used. The price to pay for this sensitivity enhancement is to introduce a priori information into the inversion by assuming the parameters indeed share structural properties. As shown in Chapter 4, this approach improves both low and high spatial frequency of the recovered parameters.

CHAPTER 3:

JOINING SENSITIVITIES OF

FULL-WAVEFORM GPR AND ER DATA

¹ We develop an algorithm for joint inversion of full-waveform ground-penetrating radar (GPR) and electrical resistivity (ER) data. GPR is sensitive to electrical permittivity through reflectivity and velocity, and electrical conductivity through reflectivity and attenuation. ER is directly sensitive to electrical conductivity. The two types of data are inherently linked through Maxwell's equations and we jointly invert them. Results show that the two types of data work cooperatively to effectively regularize each other while honoring the physics of the geophysical methods. We first compute sensitivity updates separately for both the GPR and ER data using the adjoint method, and then we sum these updates to account for both types of sensitivities. The sensitivities are added with the paradigm of letting both data types always contribute to our inversion in proportion to how well their respective objective functions are being resolved in each iteration. Our algorithm makes no assumption of the subsurface geometry nor structural similarities between parameters with the caveat of needing a good initial model. We find that our joint inversion outperforms both GPR and ER separate inversions and determine that GPR effectively supports

¹This chapter has been submitted to *Geophysics* and is currently under review. Domenzain *et al.* (2019a)

ER in regions of low conductivity while ER supports GPR in regions with strong attenuation.

3.1 Introduction

Imaging electrical properties (e.g. electrical permittivity ε and conductivity σ) is widely used for environmental and engineering applications. Contrasts in subsurface permittivity have been used to locate contaminant media (Bradford & Deeds, 2006; Babcock & Bradford, 2015), availability of water in the subsurface (Benedetto, 2010; Dogan *et al.*, 2011; Parsekian *et al.*, 2012), measure stratigraphy and volumetric water content in snow (Bradford *et al.*, 2009a; Sold *et al.*, 2013; Schmid *et al.*, 2014), find geologic structures (Kjær *et al.*, 2018) and build hydrogeologic models for water-flow simulations (Knight, 2001). Subsurface conductivity has been used to quantify water content (Binley *et al.*, 2002; Brunet *et al.*, 2010; Beff *et al.*, 2013), determine temperature distributions for geothermal exploration (Fikos *et al.*, 2012; Hermans *et al.*, 2012; Spichak & Zakharova, 2015), assess risk of landslides (Jomard *et al.*, 2010; Perrone *et al.*, 2014), monitor carbon-dioxide storage (Bergmann *et al.*, 2012; Carrigan *et al.*, 2013) and characterize mountain permafrost (Hauck *et al.*, 2003; Scapozza *et al.*, 2011; Rödder & Kneisel, 2012). Despite the broad range of applications for mapping electrical properties of the subsurface using GPR and ER methods, often a choice has to be made in using either method because of their contrasting sensitivities.

GPR is sensitive to electrical permittivity through reflectivity and velocity, and also sensitive to electrical conductivity through reflectivity and attenuation. However, if attenuation is strong in the media of interest the observed waveforms might not contain enough information to image either the permittivity or the conductivity. ER is directly (and only) sensitive to electrical conductivity, however if the media of interest

has low conductivity, the measured data might not have enough information to give a meaningful image. Fortunately GPR and ER data have a complimentary relationship. GPR is sensitive to what ER is not (permittivity) and ER is directly sensitive to what GPR is only sensitive by weak reflections and attenuation (conductivity). Moreover, GPR data gives a higher spatial resolution image of the media of interest in contrast with the lower spatial resolution obtained with the ER data.

Even though ray-theory methods for processing GPR data might resolve important features of the imaged media (Holliger *et al.*, 2001; Bradford, 2006; Bradford *et al.*, 2009a), the caveat of only using the infinite frequency approximation of the data can lead to unsatisfactory results (Johnson *et al.*, 2007; Linde & Vrugt, 2013). Introduced by Tarantola (1984) in the acoustic regime, full-waveform inversion of electromagnetic data has seen a steady interest for recovering electrical properties of the subsurface (see Ernst *et al.* (2007a) and Meles *et al.* (2010) for electromagnetic rather than acoustic full-waveform inversion). While many advances have been made for cross-hole data (Ernst *et al.*, 2007a; Meles *et al.*, 2010; Klotzsche *et al.*, 2014; Gueting *et al.*, 2017), using full waveform inversion for surface acquired GPR data in the presence of strong attenuative media remains an important challenge (Lavoué *et al.*, 2014; Schmid *et al.*, 2014).

In Lavoué *et al.* (2014) the authors perform full-waveform inversions of GPR on two synthetic examples, one with sources and receivers surrounding the target media and one with sources and receivers at the surface. When the target media is surrounded by sources and receivers they are able to recover accurate spatial resolution and values of the electrical parameters even when their starting models for both permittivity and conductivity are homogenous. However, when using surface acquired

data the conductivity solution lacks accuracy and spatial resolution at shallow depths and is almost insensitive to sharp contrasts at depth. Moreover, in this case their starting models for both permittivity and conductivity are a smoothed version of the true parameters, which assumes a very accurate initial model is available. The sharp difference in the resolution of the recovered parameters between these two synthetic experiments can be attributed to the sparse illumination due to having just surface acquired data, and shows how ill-posed GPR full-waveform inversion can be when the conductivity is not known a priori.

ER inversion methods using the full response of the measured electric field range in how the data sensitivities are computed and in how the discretized physics are solved (Loke & Barker, 1996; Spitzer, 1998; Ha *et al.*, 2006; Pidlisecky *et al.*, 2007; Domenzain *et al.*, 2017). Overall, the advances of the method have evolved in more accurate discretization schemes and computationally cheaper inversion routines. Because of the inherent low-spatial and shallow depth resolution of the ER data, sharp boundaries of the subsurface conductivity can be challenging to capture without external a priori knowledge of the subsurface or strong regularization (Hetrick & Mead, 2018).

In order to exploit the complimentary sensitivities of the GPR and ER experiments, we implement an inversion algorithm that recovers both permittivity and conductivity of the media of interest by joining the sensitivities of conductivity from both the GPR and ER data in each iteration of the inversion process. In what follows we make the physical assumptions of an isotropic linear media where Ohm's law holds, with no lateral variation in the y -coordinate, a constant magnetic permeability of μ_0 and frequency independent electrical parameters.

In recent work regarding GPR full-waveform inversion (Ernst *et al.*, 2007a; Meles

et al., 2010; Klotzsche *et al.*, 2014; Lavoué *et al.*, 2014; Gueting *et al.*, 2017) it has been assumed that electrical conductivity is constant over a bandwidth of the radar signal and permittivity is frequency independent. Incorporating frequency dependent attenuation for a full-waveform inversion approach can be done as in Xue *et al.* (2017), where the authors use a modified version of the wave equation (Zhu & Harris, 2014) and develop forward and adjoint operators that approximate the effects of frequency dependent attenuation. This enforces a higher computational cost compared to assuming frequency-constant attenuation. In Giannakis *et al.* (2015) the authors develop a 3d finite-difference time-domain forward model for electromagnetic wave propagation that incorporates frequency dependent parameters by convolving Debye relaxation mechanisms directly in the wave solver. Their forward model is capable of accurately predicting the behavior of electromagnetic fields with frequency dependent parameters but a full-waveform inversion algorithm that accounts for the convolution of relaxation mechanisms is still to be developed.

Recovering frequency dependent attenuation from surface acquired GPR data can be done as in Bradford (2007). The method links the attenuation coefficient to a dispersion relation that is measurable in the GPR data. It is noted that this method does not account for intrinsic vs scattering attenuation since it does not take into account the full kinematics of the electromagnetic wave. It is also recognized that because of the inability of GPR data to recognize reflections due to velocity from reflections due to conductive media, recovering the full attenuation response requires additional low frequency data. Using the full kinematic response of GPR on surface acquired data to recover attenuation is a very ill-posed problem. As an example, see the results of Lavoué *et al.* (2014) on surface acquired data.

In Figure 3.1-**a** and **b** we present the real part of the frequency dependent effective conductivity as well as the DC conductivity. These values were computed using the Cole-Cole model with parameters given by Bradford (2007) (for sands and clay), Friel & Or (1999) (for silty loam) and Taherian *et al.* (1990) (for sandstone with brine). In general, the more conductive the material the larger the difference between DC and effective conductivity. However, the larger the conductivity the less signal we have in the GPR data. Figure 3.1-**d** shows that for high conductivity the skin factor drops below 1m as materials increase in conductivity. We note that for most earth materials, the DC and effective conductivity differs by a factor of less than an order of magnitude. In Table 3.1 we complete our list of materials with those in Loewer *et al.* (2017) (for humus, laterite and loess). We quantify how much this factor is at 250MHz and find that most earth materials differ by a factor of less than 5. Only dry sand (for this particular measured sample) exhibits a factor of 10, although the DC and effective conductivity are still low at 0.45 and 4.5 mS/m respectively.

We recognize that frequency independent electrical parameters are generally not found in nature. However, Figure 3.1 and Table 3.1 show that for a range of earth materials the frequency dependence varies by a small factor (less than 5 in most cases) and that in cases where the conductivity is large, the GPR loses most of its signal due to attenuation. Assuming frequency independent parameters forms a starting point for the evaluation of our inversion algorithm and comprises a reasonable trade-off between computation cost, field applications, the full use of the GPR waveform, and a lack of enforced assumptions of subsurface geometry and petrophysical models.

Joining data from different types of geophysical imaging methods holds the promise of reducing the non-linearity of characterizing subsurface material properties (Ogunbo

et al., 2018). Different approaches coupling the subsurface material properties as well as different algorithmic workflows have been developed in order to join different types of sensitivities (Moorkamp, 2017). Broadly, the material properties coupling can be done via geologic structure (where different material properties are assumed to share the same geometry (Haber & Oldenburg, 1997; Gallardo & Meju, 2003; Haber & Gazit, 2013)) or linked by petrophysical relationships (Ghose & Slob, 2006). More specifically, Linde *et al.* (2006) use GPR and ER cross-hole data assuming structural similarities of electromagnetic properties and simplifying the physics of the GPR to only use travel times. Our approach for joint inversion does not assume structural similarities and does not need petrophysical relationships since the GPR and ER data are physically linked through conductivity with Maxwell's equations. We are able to increase the amplitude and spatial frequency resolution of the inverted electrical properties in a joint inversion compared with individual inversions of surface acquired data. In this way the GPR and ER optimization problems effectively regularize each other while honoring the physics.

The layout of this chapter is as follows. In the subsections **GPR Inversion** and **ER Inversion** both the GPR and ER inversion schemes are developed separately and in Section **Joint Inversion** the method for joining the different sensitivities is described. In Section **Examples** we give results from our method with two different scenarios for underground exploration of surface acquisition: (1) low conductivity and (2) high conductivity, and present results with added noise in both the GPR and ER data.

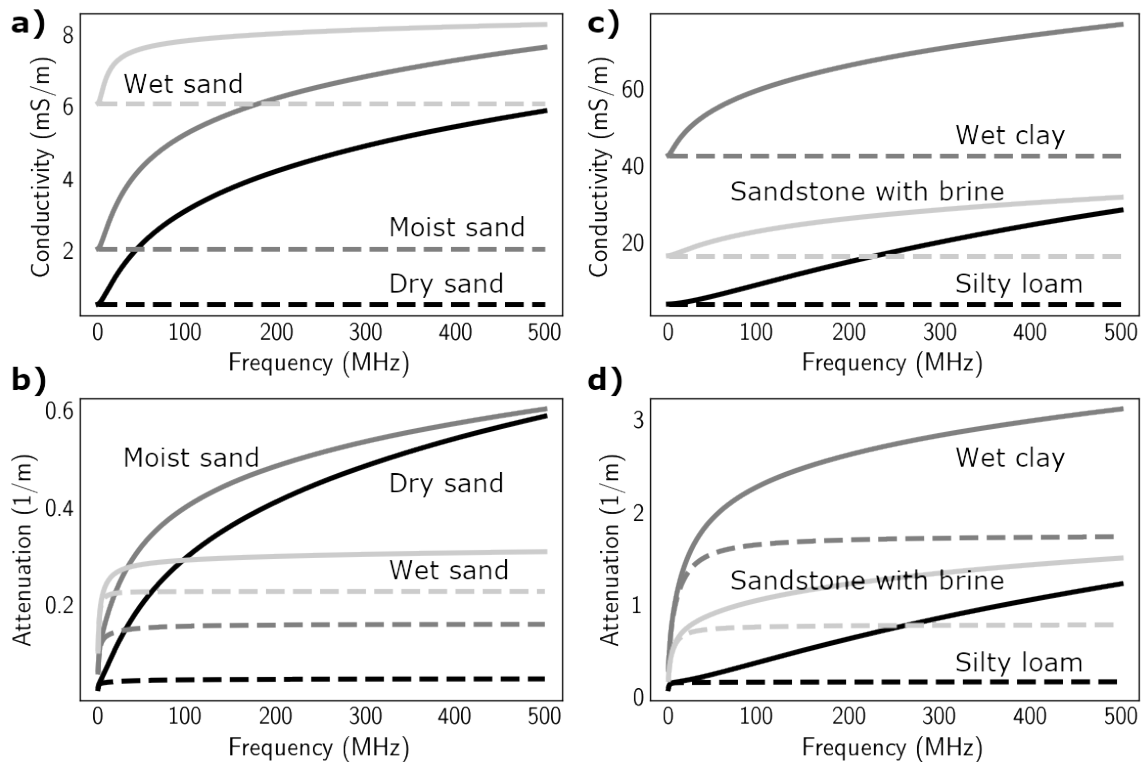


Figure 3.1: Frequency dependent conductivity and attenuation coefficients of various earth materials. Solid and dashed lines represent (real) effective and DC conductivity respectively. In a and b are low conductivity materials where GPR data has a large signal-to-noise ratio. In c and d are high conductivity materials where GPR data has a low signal-to-noise ratio.

Table 3.1: Frequency dependent and DC conductivities at 250MHz given by the Cole-Cole model. Most earth materials present an increase of at most 5 between DC and (real) effective conductivity.

	Effective (mS/m)	DC (mS/m)	Effective/DC
Dry sand	4.54	0.45	10.1
Moist sand	6.53	2	3.26
Wet sand	8.06	6.06	1.33
Silty loam	17.3	3.5	4.93
Sandstone with brine	27.2	16.2	1.68
Humus	43.1	19.5	2.21
Laterite	45	9	5
Wet clay	68.4	42.5	1.61
Loess	185	72.3	2.55

3.2 Inversion methods

3.2.1 GPR inversion

The physics of the GPR experiment are given by the time dependent Maxwell's equations,

$$\begin{pmatrix} \mu_o & 0 & 0 \\ 0 & \mu_o & 0 \\ 0 & 0 & \varepsilon \end{pmatrix} \begin{pmatrix} \dot{H}_z \\ -\dot{H}_x \\ \dot{E}_y \end{pmatrix} = \begin{pmatrix} 0 & 0 & \partial_x \\ 0 & 0 & \partial_z \\ \partial_x & \partial_z & 0 \end{pmatrix} \begin{pmatrix} H_z \\ -H_x \\ E_y \end{pmatrix} - \sigma \begin{pmatrix} 0 \\ 0 \\ E_y \end{pmatrix} + \begin{pmatrix} 0 \\ 0 \\ -J_y \end{pmatrix}, \quad (3.1)$$

where E_y is the electric field component in the y direction, (H_x, H_z) are the magnetic field components in the x and z direction, J_y is the source term, ε is the relative electrical permittivity (which we refer to only as permittivity), and σ is the electrical

conductivity. Both ε and σ are assumed constant in time and frequency independent. In order to keep notation clean we will refer to operators and variables in upper and lower case letters respectively, and so refer to the wavefield E_y as u . Table 3.2 gives a comprehensive list of the notation symbols used in this dissertation. We use a finite-difference time-domain method on a Yee grid (Yee, 1966) with PML boundary conditions (Berenger, 1996) to solve the discretized time-domain (Domenzain *et al.*, 2017) version of equation 3.1 which for reference we write as,

$$\begin{aligned} \mathbf{u} &= \mathbf{L}_w \mathbf{s}_w, \\ \mathbf{d}_w^s &= \mathbf{M}_w \mathbf{u} \end{aligned} \tag{3.2}$$

where \mathbf{L}_w is the discretized differential (time marching) operator of equation 3.1, \mathbf{u} is the electric field y component defined in space and time, \mathbf{s}_w is the source term, \mathbf{M}_w is the measuring operator, and $\mathbf{d}_w^s = \mathbf{M}_w \mathbf{u}$ is the data of the experiment, i.e. a common-source gather. The operator \mathbf{M}_w formalizes the action of taking the data \mathbf{d}_w^s (a two-dimensional slice in time and receivers) from the three dimensional tensor \mathbf{u} with dimensions of time, length and depth. From now on ε and σ will denote the frequency independent electrical permittivity and conductivity distributions in the xz plane and discretized as matrixies of size $n_z \times n_x$ where n_x and n_z denote the number of nodes in the xz -plane discretization.

We formulate our GPR inversion algorithm by finding parameters ε_* and σ_* that satisfy,

$$\{\varepsilon_*, \sigma_*\} = \arg \min \frac{1}{2} (\Theta_{w,\varepsilon}(\varepsilon; \mathbf{d}_w^o) + \Theta_{w,\sigma}(\sigma; \mathbf{d}_w^o)), \tag{3.3}$$

where the subscript * denotes the imaged parameters and \mathbf{d}_w^o denotes all the observed

GPR data. We have,

$$\Theta_{w,\varepsilon} = \frac{1}{n_s} \sum_s \Theta_{w,\varepsilon}^s, \quad (3.4)$$

where s indexes the sources, n_s denotes the total number of sources, and

$$\Theta_{w,\varepsilon}^s = \frac{\|\mathbf{e}_w\|_2^2}{\|\mathbf{d}_w^{o,s}\|_2^2}, \quad (3.5)$$

where $\mathbf{d}_w^{o,s}$ is the observed data for one source and $\mathbf{e}_w = \mathbf{d}_w^s - \mathbf{d}_w^{o,s}$ is the residual of the modeled and observed data. A similar expression for $\Theta_{w,\sigma}$ follows with the only difference between $\Theta_{w,\varepsilon}$ and $\Theta_{w,\sigma}$ being the order in the inversion scheme in which they are evaluated.

In order to find model updates $\Delta\boldsymbol{\sigma}_w$ and $\Delta\boldsymbol{\varepsilon}$ that minimize Θ_w we first obtain the gradients $\mathbf{g}_{w,\sigma}$ and \mathbf{g}_ε of $\Theta_{w,\varepsilon}^s$ and $\Theta_{w,\sigma}^s$ respectively following Meles *et al.* (2010) using a full waveform inversion approach,

$$\mathbf{v}_w = \mathbf{L}_w \mathbf{e}_w(-t), \quad (3.6)$$

$$\mathbf{g}_{w,\sigma} = - \sum_t \mathbf{u}(-t) \odot \mathbf{v}_w(t) \cdot \Delta t, \quad (3.7)$$

$$\mathbf{g}_\varepsilon = - \sum_t \dot{\mathbf{u}}(-t) \odot \mathbf{v}_w(t) \cdot \Delta t, \quad (3.8)$$

where t denotes time, $(-t)$ denotes time reversed, \odot denotes element-wise multiplication, $\dot{\mathbf{u}}$ denotes the time derivative of \mathbf{u} (computed in a finite-difference way), \mathbf{v}_w is the adjoint wavefield (the back-propagation of errors), and Δt denotes the discretized time interval. As noted by Kurzmann *et al.* (2013) using the adjoint method introduces high amplitude artifacts near the receivers that dominate the gradients. In order to remove these high amplitudes, we first multiply the gradients by a 2d Gaus-

sian surface in the xz -plane centered at the source location. The bandwidth of the 2d Gaussian equals a wavelength where the wavelength is computed using the characteristic frequency of our survey and the velocity at the source location. We then apply a Gaussian lowpass space-frequency filter following Taillandier *et al.* (2009) with the choice of bandwidth so as to only allow wavelengths larger than or equal to the characteristic wavelength of the model. The updates are,

$$\Delta\boldsymbol{\sigma}_w = -\frac{1}{n_w} \sum_{s=1}^{n_w} \alpha_\sigma \mathbf{g}_{w,\sigma}, \quad (3.9)$$

$$\Delta\boldsymbol{\varepsilon} = -\frac{1}{n_w} \sum_{s=1}^{n_w} \alpha_\varepsilon \mathbf{g}_\varepsilon, \quad (3.10)$$

where n_w is the number of GPR common-shot gathers and α_σ and α_ε are step-sizes for each gradient.

Even with a true descent direction $-\mathbf{g}_\varepsilon$, finding α_ε can be a very ill-posed inverse problem by itself leading to negative step-sizes, overshoot of the solution $\boldsymbol{\varepsilon}_*$ or a very slow convergence. Overshooting the solution $\boldsymbol{\varepsilon}_*$ can lead to our current values of $\boldsymbol{\varepsilon}$ to fall outside the velocity interval determined by the stability conditions of our finite-difference wave solver both in time (Courant *et al.*, 1967) and space (e.g. numerical dispersion).

For these reasons we choose to compute the step-size α_ε with a three-point parabola approximation of the objective function $\Theta_{w,\varepsilon}^s$ in the direction of its gradient (Wright & Nocedal, 1999). Each point used in the parabola approximation is the image of a perturbed permittivity $\hat{\boldsymbol{\varepsilon}}_i$ under the objective function $\Theta_{w,\varepsilon}^s$,

$$\hat{\boldsymbol{\varepsilon}}_i = \boldsymbol{\varepsilon} \odot \exp(-\boldsymbol{\varepsilon} \odot p_i \kappa_\varepsilon \cdot \mathbf{g}_\varepsilon), \quad i = 1, 2, 3, \quad (3.11)$$

where κ_ε is a positive real number and p_i is a fixed user defined percentage. At each iteration and for each source, κ_ε is chosen automatically in order to enforce the perturbed permittivity to lie within a certain range of possible values, i.e. within the stability velocity interval imposed by our wave solver (Courant *et al.*, 1967) and we choose κ_ε to be as large as possible. We leave the details of finding κ_ε in **Appendix A**. Because at a given iteration we already have a value of $\Theta_{w,\varepsilon}^s$ for the current permittivity (i.e. with no perturbation), we choose p_i to be 0, 0.05 and 0.5. We proceed by computing $\Theta_{w,\varepsilon}^s(\hat{\boldsymbol{\varepsilon}}_i; \mathbf{d}_w^{o,s})$ for $i = 1, 2, 3$ and then fitting a parabola through these points from which we analytically compute where the argument takes its minimum value: α_ε .

The computational cost of finding α_ε imposes one extra run of our forward model (equation 3.2) from what is done in Ernst *et al.* (2007b) and Meles *et al.* (2010), but gives more accurate values for the descent direction. We note that our search for κ_ε guarantees the permittivity values always lie within the stability conditions of our wave solver: both for the perturbations $\hat{\boldsymbol{\varepsilon}}_i$ and the updated $\boldsymbol{\varepsilon}$.

Because GPR is only sensitive to conductivity through attenuation and weak reflections, in the case of strong attenuation the GPR data might not have enough information to constrain a parabolic shape on $\Theta_{w,\sigma}^s$ in the vicinity of the current parameters. We find the step-size α_σ by first finding the largest possible real number $\kappa_{w,\sigma}$ for which the perturbation in the direction of $-\kappa_{w,\sigma} \mathbf{g}_{w,\sigma}$ keeps the conductivity within a prescribed range of possible values. We then take a small percentage (in the order of 1%) of this value to be α_σ .

In late iterations we find that the updates in equation 3.9 can lead to an oscillatory exploration of the solution space. To mitigate this effect we impose a momentum m_ε

(Rumelhart *et al.*, 1986) to the descent direction $\Delta\boldsymbol{\varepsilon}$,

$$\Delta\boldsymbol{\varepsilon} \leftarrow \Delta\boldsymbol{\varepsilon} + m_\varepsilon \Delta\boldsymbol{\varepsilon}_\bullet, \quad (3.12)$$

where $\Delta\boldsymbol{\varepsilon}_\bullet$ is the update of the previous iteration. The value of m_ε is kept constant throughout the inversion with a value of 25%.

At each iteration the updates are done in logarithmic scale in order to enforce the physical positivity constraint on both $\boldsymbol{\varepsilon}$ and $\boldsymbol{\sigma}$ (Meles *et al.*, 2010),

$$\boldsymbol{\varepsilon} \leftarrow \boldsymbol{\varepsilon} \odot \exp(\boldsymbol{\varepsilon} \odot \Delta\boldsymbol{\varepsilon}), \quad (3.13)$$

$$\boldsymbol{\sigma} \leftarrow \boldsymbol{\sigma} \odot \exp(\boldsymbol{\sigma} \odot \Delta\boldsymbol{\sigma}_w). \quad (3.14)$$

As noted by Meles *et al.* (2010), if the conductivity and permittivity reflections vary significantly it is not always convenient to compute the gradients and update under the same forward run. In lieu of this observation, in each iteration we first compute equation 3.2, we then compute $\Delta\boldsymbol{\varepsilon}$ and update $\boldsymbol{\varepsilon}$, we then compute our synthetic data (equation 3.2) again, compute $\Delta\boldsymbol{\sigma}_w$ and update $\boldsymbol{\sigma}$. In total, for each iteration for one source we compute equation 3.2 four times and equation 3.6 two times, which in total accounts for six forward models.

Assuming the source wavelet is known for all sources in our GPR experiment, we give the algorithm for computing the updates $\Delta\boldsymbol{\varepsilon}$ and $\Delta\boldsymbol{\sigma}_w$ in Figure 3.2. The full GPR inversion algorithm is given in Figure 3.4. The initialization of our algorithm consists in defining all constants used in our inversion and inputting a good initial guess for both permittivity and conductivity.

a)Permittivity update $\Delta\epsilon$ with GPR

- Loop over all sources.

 1. Compute \mathbf{u} , \mathbf{d}_w , \mathbf{e}_w and $\Theta_{w,\epsilon}^s$.
 2. Compute $\dot{\mathbf{u}}$, \mathbf{v}_w and \mathbf{g}_ϵ .
 3. Damp high amplitudes of \mathbf{g}_ϵ near the source location.
 4. Smooth \mathbf{g}_ϵ in the space frequency domain.
 5. Normalize \mathbf{g}_ϵ by its largest amplitude and compute α_ϵ .

- Compute $\Theta_{w,\epsilon}$ and,

$$\Delta\epsilon = -\frac{1}{n_w} \sum_{s=1}^{n_w} \alpha_\epsilon \mathbf{g}_\epsilon.$$

- Apply *momentum*,

$$\Delta\epsilon \leftarrow \Delta\epsilon + m_\epsilon \Delta\epsilon_0.$$

b)Conductivity update $\Delta\sigma_w$ with GPR

- Loop over all sources.

 1. Compute \mathbf{u} , \mathbf{d}_w , \mathbf{e}_w and $\Theta_{w,\sigma}^s$.
 2. Compute \mathbf{v}_w and $\mathbf{g}_{w,\sigma}$.
 3. Damp high amplitudes of $\mathbf{g}_{w,\sigma}$ near the source location.
 4. Smooth $\mathbf{g}_{w,\sigma}$ in the space frequency domain.
 5. Normalize $\mathbf{g}_{w,\sigma}$ by its largest amplitude and compute α_σ .

- Compute $\Theta_{w,\sigma}$ and,

$$\Delta\sigma_w = -\frac{1}{n_w} \sum_{s=1}^{n_w} \alpha_\sigma \mathbf{g}_{w,\sigma}.$$

Figure 3.2: Algorithms for computing the updates $\Delta\epsilon$ and $\Delta\sigma_w$.

3.2.2 ER inversion

The physics of the ER experiment are given by the steady state Maxwell's equations where Ohm's law holds (Pidlisecky *et al.*, 2007),

$$-\nabla \cdot \sigma \nabla \varphi = \mathbf{i}(\delta(x - s_+) - \delta(x - s_-)), \quad (3.15)$$

where φ is the electric potential, \mathbf{i} is the current intensity, s_{\pm} is the source-sink location, and σ is the electrical conductivity. Note that under our assumptions the conductivity in equation 3.15 is the same as in equation 3.1. We write the discretized version of equation 3.15 as,

$$\begin{aligned} \mathbf{L}_{dc}\varphi &= \mathbf{s}_{dc}, \\ \mathbf{d}_{dc}^s &= \mathbf{M}_{dc}\varphi, \end{aligned} \quad (3.16)$$

where \mathbf{L}_{dc} is the discretized differential operator of equation 3.15, φ is the electric potential (a vector of size $n_x n_z \times 1$), \mathbf{s}_{dc} is the source term (a vector of size $n_x n_z \times 1$), \mathbf{M}_{dc} is the measuring operator that computes observed voltages (a matrix of size $n_{\mathbf{d}_{dc}^s} \times n_x n_z$ where $n_{\mathbf{d}_{dc}^s}$ denotes the number of measured voltages), and \mathbf{d}_{dc}^s is the data of the experiment for one source (a vector of size $n_{\mathbf{d}_{dc}} \times 1$).

We follow Dey & Morrison (1979) and use a finite volume method to build the discretized operator \mathbf{L}_{dc} , a sparse banded matrix of size $n_x n_z \times n_x n_z$ whose entries are a function of σ and the boundary conditions. Neumann boundary conditions are applied on the air-ground interface, and Robin boundary conditions are applied in the subsurface (Dey & Morrison, 1979). By specifying Neumann boundary conditions on the air-ground interface and Robin boundary conditions in the subsurface, the matrix \mathbf{L}_{dc} is directly invertible. The source vector \mathbf{s}_{dc} is sparse having only ± 1 entries at

the source and sink positions.

In order to directly compare the sensitivities of both experiments, we use the same discretized grid for both the GPR and the ER forward models. The spacings $\Delta x, \Delta z$ and Δt are determined by the Courant-Friedrichs-Lowy condition (Courant *et al.*, 1967) with a user imposed interval of possible velocities in order for the GPR forward model to be numerically stable.

We formulate our ER inversion algorithm by finding $\boldsymbol{\sigma}_*$ that satisfies,

$$\boldsymbol{\sigma}_* = \arg \min \Theta_{dc}(\boldsymbol{\sigma}; \mathbf{d}_{dc}^o), \quad (3.17)$$

where \mathbf{d}_{dc}^o is all of the ER data. We have,

$$\Theta_{dc} = \frac{1}{n_s} \sum_s \Theta_{dc}^s, \quad (3.18)$$

where s indexes the source, n_s denotes the total number of sources, and

$$\Theta_{dc}^s = \frac{\|\mathbf{e}_{dc}\|_2^2}{\|\mathbf{d}_{dc}^{o,s}\|_2^2}. \quad (3.19)$$

We denote $\mathbf{d}_{dc}^{o,s}$ the observed data for one source and $\mathbf{e}_{dc} = \mathbf{d}_{dc}^s - \mathbf{d}_{dc}^{o,s}$ the residual of the modeled and observed data. In order to find the model update $\Delta\boldsymbol{\sigma}_{dc}$ that minimizes Θ_{dc}^s we first find the gradient of Θ_{dc}^s with respect to $\boldsymbol{\sigma}$. Let $\nabla_{\boldsymbol{\sigma}}$ be the vector of size $1 \times n_x n_z$ whose entries are the partial derivatives with respect to $\boldsymbol{\sigma}$.

We compute \mathbf{g}_{dc} using the adjoint potential field \mathbf{v}_{dc} ,

$$\begin{aligned}\mathbf{L}_{dc}^\top \mathbf{v}_{dc} &= \mathbf{M}_{dc}^\top \mathbf{e}_{dc}, \\ \mathbf{g}_{dc} &= \mathbf{S}_{dc} \mathbf{v}_{dc},\end{aligned}\tag{3.20}$$

where \mathbf{g}_{dc} and \mathbf{v}_{dc} are vectors of size $n_x n_z \times 1$ and $\mathbf{S}_{dc} = -((\nabla_\sigma \mathbf{L}_{dc}) \boldsymbol{\varphi})^\top$ is a matrix of size $n_x n_z \times n_x n_z$. We leave the details of this derivation for **Appendix B**.

Similarly to \mathbf{g}_ε and $\mathbf{g}_{w,\sigma}$, the gradient \mathbf{g}_{dc} exhibits strong amplitudes near the sources and receivers. We use the approach of Taillandier *et al.* (2009) to filter out these artifacts by applying a lowpass space-frequency domain Gaussian filter with a choice of radius so as to only allow wavelengths larger or equal than the smallest source-receiver spacing.

Once the gradients for all sources have been computed the update is,

$$\Delta\boldsymbol{\sigma}_{dc} = -\frac{1}{n_{dc}} \sum_{s=1}^{n_{dc}} \alpha_{dc} \mathbf{g}_{dc},\tag{3.21}$$

where n_{dc} is the number of ER experiments, and α_{dc} is a particular step size for each \mathbf{g}_{dc} . The step-size computations are done following Pica *et al.* (1990), where a perturbation $\hat{\boldsymbol{\sigma}}$ of $\boldsymbol{\sigma}$ in the direction of the gradient \mathbf{g}_{dc} is needed. We find the optimal perturbation parameter κ_{dc} such that,

$$\hat{\boldsymbol{\sigma}} = \boldsymbol{\sigma} \odot \exp(-\boldsymbol{\sigma} \odot \kappa_{dc} \mathbf{g}_{dc}),\tag{3.22}$$

using the same algorithm (but separately) as with the GPR inversion. Similarly to the GPR permittivity sensitivity, we add a momentum in the order of 10% of the previous iteration update to the current update $\Delta\boldsymbol{\sigma}_{dc}$ to avoid an oscillatory search

of the solution space (Rumelhart *et al.*, 1986),

$$\Delta\boldsymbol{\sigma}_{dc} \leftarrow \Delta\boldsymbol{\sigma}_{dc} + m_{dc} \Delta\boldsymbol{\sigma}_{dc\bullet}, \quad (3.23)$$

where $\Delta\boldsymbol{\sigma}_{dc\bullet}$ is the update from the previous iteration and m_{dc} is kept constant throughout the inversion. At each iteration the update is done in logarithmic scale in order to enforce the physical positivity constraint on $\boldsymbol{\sigma}$,

$$\boldsymbol{\sigma} \leftarrow \boldsymbol{\sigma} \odot \exp(\boldsymbol{\sigma} \odot \Delta\boldsymbol{\sigma}_{dc}). \quad (3.24)$$

We give the algorithm for computing the update $\Delta\boldsymbol{\sigma}_{dc}$ in Figure 3.3. The full ER inversion algorithm is given in Figure 3.4. The initialization of our algorithm consists in defining all constants used in our inversion and inputting an initial model for conductivity.

3.3 Joint inversion

We formulate our GPR and ER joint inversion algorithm by finding parameters $\boldsymbol{\varepsilon}_*$ and $\boldsymbol{\sigma}_*$ that satisfy,

$$\{\boldsymbol{\varepsilon}_*, \boldsymbol{\sigma}_*\} = \arg \min \frac{1}{2} (\Theta_{w,\varepsilon}(\boldsymbol{\varepsilon}; \mathbf{d}_w^o) + \Theta_{w,\sigma}(\boldsymbol{\sigma}; \mathbf{d}_w^o)) + \Theta_{dc}(\boldsymbol{\sigma}; \mathbf{d}_{dc}^o). \quad (3.25)$$

We optimize equation 3.25 by joining the updates $\Delta\boldsymbol{\sigma}_w$ and $\Delta\boldsymbol{\sigma}_{dc}$ obtained by equations 3.9 and 3.21 respectively. Since $\Delta\boldsymbol{\sigma}_w$ and $\Delta\boldsymbol{\sigma}_{dc}$ generally vary in magnitude, in order for the updates to share their different spatial sensitivities, we first normalize them by their largest amplitude and then add them together with scalar weights a_w

Conductivity update $\Delta\sigma_{dc}$ with ER

- Loop over all sources.
 1. Compute φ , \mathbf{d}_{dc} , \mathbf{e}_{dc} and Θ_{dc}^s .
 2. Compute \mathbf{v}_{dc} and \mathbf{g}_{dc} .
 3. Smooth \mathbf{g}_{dc} in the space frequency domain.
 4. Normalize \mathbf{g}_{dc} by its largest amplitude and compute α_{dc} .
- Compute Θ_{dc} and,

$$\Delta\sigma_{dc} = -\frac{1}{n_{dc}} \sum_{s=1}^{n_{dc}} \alpha_{dc} \mathbf{g}_{dc}.$$

- Apply *momentum*,

$$\Delta\sigma_{dc} \leftarrow \Delta\sigma_{dc} + m_{dc} \Delta\sigma_{dc} \bullet.$$

Figure 3.3: Algorithm for computing the update $\Delta\sigma_{dc}$.

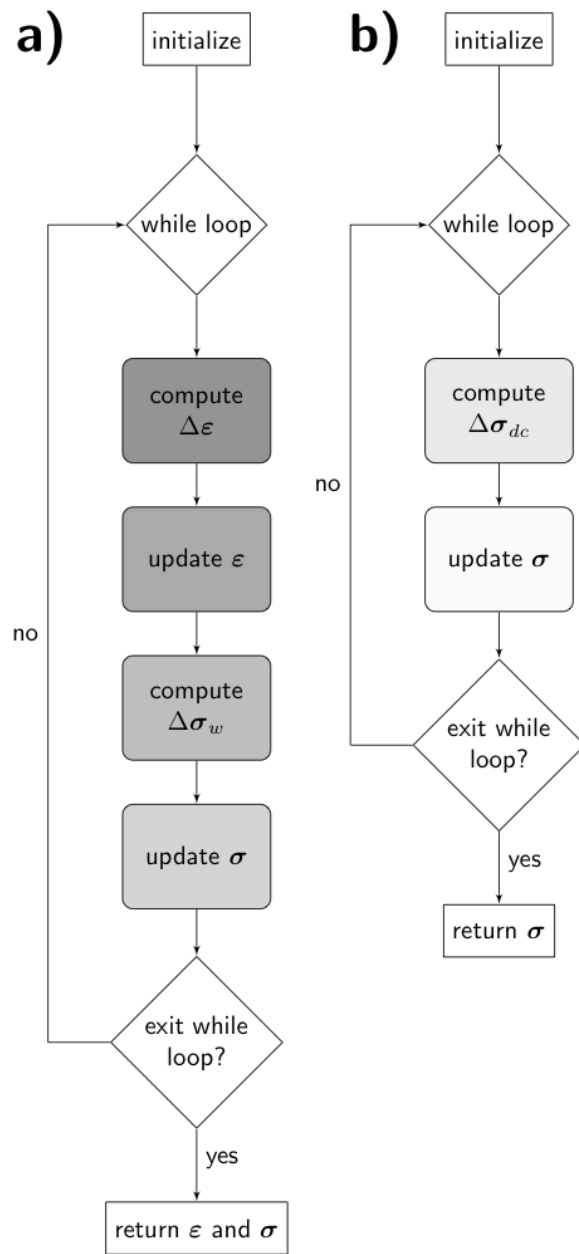


Figure 3.4: Inversion algorithms for a GPR and b ER.

Table 3.2: Reference for the notation used in the discretized inverse problems. Symbols common in both GPR and ER experiments are stripped from their subscripts to avoid clutter.

Symbol	Meaning	Note
ϵ	Discretized electrical relative permittivity	
σ	Discretized electrical conductivity	
L	Discretized differential operator	
s	Discretized source	
M	Discretized measuring operator	
d	Synthetic data	
e	Residual of synthetic vs observed data	
Θ	Objective function	Used for GPR and ER
v	Discretized adjoint field	
g	Gradient of objective function	
α	Step size for g	
κ	Perturbation parameter used to find α	
m	Momentum parameter	
u	Electric wavefield on the y component	
\dot{u}	Finite-difference time derivative of u	
$\hat{\epsilon}$	Perturbed permittivity	Only GPR
$\Delta\sigma_w$	GPR conductivity update	
$\Delta\epsilon$	GPR permittivity update	
$\Delta\epsilon_{\bullet}$	GPR permittivity update from the previous iteration	
φ	Discretized electric potential	
S_{dc}	The matrix $-((\nabla_\sigma L_{dc})\varphi)^\top$	
$\hat{\sigma}$	Perturbed conductivity	Only ER
$\Delta\sigma_{dc}$	ER conductivity update	
$\Delta\sigma_{dc\bullet}$	ER Conductivity update from previous iteration	
$\Delta\sigma$	Joint conductivity update	
a_w	Weight to regulate $\Delta\sigma_w$	Used for the joint update
a_{dc}	Weight to regulate $\Delta\sigma_{dc}$	
h	Weight to regulate a_w and a_{dc}	
c	Step size for $\Delta\sigma$	

and a_{dc} ,

$$\Delta\boldsymbol{\sigma} = a_w \Delta\boldsymbol{\sigma}_w + a_{dc} \Delta\boldsymbol{\sigma}_{dc}, \quad (3.26)$$

then normalize $\Delta\boldsymbol{\sigma}$ by its largest amplitude and finally write,

$$\Delta\boldsymbol{\sigma} \leftarrow c \Delta\boldsymbol{\sigma}, \quad (3.27)$$

where c is the geometric mean of the maximum amplitudes of $\Delta\boldsymbol{\sigma}_w$ and $\Delta\boldsymbol{\sigma}_{dc}$ prior to normalization. See Figure 3.5-a for a summary of this procedure. The choices for weights a_w and a_{dc} are made with the paradigm of letting both updates $\Delta\boldsymbol{\sigma}_w$ and $\Delta\boldsymbol{\sigma}_{dc}$ always contribute to $\Delta\boldsymbol{\sigma}$ in proportion to their objective function value at a given iteration: if the objective function value of one is smaller than the other, then the one with the smaller value should be more heavily weighted. The ad-hoc computation of a_w and a_{dc} is,

$$a_w = \begin{cases} 1 & \text{if } h \Theta_{w,\sigma} \leq \Theta_{dc} \\ \frac{1}{\sqrt{|h \Theta_{w,\sigma} - (\Theta_{dc}-1)|}} & \text{if } \Theta_{dc} < h \Theta_{w,\sigma}, \end{cases} \quad (3.28)$$

$$a_{dc} = \begin{cases} 1 & \text{if } \Theta_{dc} \leq h \Theta_{w,\sigma} \\ \frac{1}{\sqrt{|h \Theta_{w,\sigma} - (\Theta_{dc}+1)|}} & \text{if } h \Theta_{w,\sigma} < \Theta_{dc}, \end{cases}$$

where h is a positive number that further regulates the relative weight of GPR vs ER sensitivities. The value of h modulates how much we weigh each sensitivity: an increasing value of h decreases weighting of $\Delta\boldsymbol{\sigma}_w$, while a decreasing value of h increases the weighting of $\Delta\boldsymbol{\sigma}_w$.

Moreover, the choice of h over each iteration manages two aspects of the inversion:

- (a) at early iterations GPR data gives better sensitivity of sharp boundaries at shallow depths compared to the ER data so $\Delta\sigma_w$ should be weighed more, however at later iterations ER data gives better sensitivity overall so $\Delta\sigma_w$ should be weighed less.
- (b) We interpret an increase of Θ_{dc} (or $\Theta_{w,\sigma}$) with respect to the last iteration as a “cry for help” and so $\Delta\sigma_w$ should be weighed less (or more). Figure 3.6 shows the expected “bowtie” shape over iterations of a_w and a_{dc} that drives the physical sensitivities of our data in the parameter-space search-path. At early iterations the GPR data first resolves the structure of the model while the ER data struggles to resolve conductivity at depth, so the weight a_w is given a larger value than a_{dc} . At later iterations, once the GPR data has resolved enough structure the roles of a_w and a_{dc} are reversed.

Because the geometries of the hyper-surfaces defined by $\Theta_{w,\sigma}$ and Θ_{dc} as a function of σ are not known, we ensure the values of a_w and a_{dc} comply with the bowtie shape by enforcing emergent conditions (Cucker & Smale, 2007) that act individually on the magnitude of h , but when used together they interact into forming the bowtie shape. The conditions are (see Figure 3.5-**b** for quick reference),

- (0)** We first choose a value of a_{dc} for the first iteration to be positive and smaller than 1 and force the first choice of h to comply with this initial value of a_{dc} .
- (1)** As the iterations proceed, if a_{dc} is decreasing we increase h by a fixed ratio \dot{a}_{dc} ,

$$h \leftarrow \dot{a}_{dc} h.$$

Note that a_{dc} can only decrease if a_w is 1.

- (2)** If a_w decreases we further force the descent of a_w increasing h by a fixed ratio

$$\dot{a}_w,$$

$$h \leftarrow \dot{a}_w h.$$

Note that the decrease of a_w begins when a_{dc} reaches 1.

In order to ensure the “cries for help” are listened at each iteration we enforce,

- (3) If the value of Θ_{dc} increases with respect to the last iteration we increase h by a fixed ratio $\dot{\Theta}_{dc}$,

$$h \leftarrow \dot{\Theta}_{dc} h.$$

- (4) If the value of $\Theta_{w,\sigma}$ increases with respect to the last iteration we decrease h by a fixed ratio $\dot{\Theta}_w$,

$$h \leftarrow \dot{\Theta}_w h.$$

In summary, the weight h regulates the current iteration’s choice of confidence over the sensitivities $\Delta\boldsymbol{\sigma}_w$ and $\Delta\boldsymbol{\sigma}_{dc}$, while the weights $\dot{a}_{dc}, \dot{a}_w, \dot{\Theta}_{dc}$ and $\dot{\Theta}_w$ regulate how h changes over each iteration. From conditions (1)-(4) we have,

$$\begin{aligned} \dot{a}_{dc} > 1 && \dot{\Theta}_{dc} > 1 \\ \dot{a}_w > 1 && \dot{\Theta}_w < 1. \end{aligned} \tag{3.29}$$

Because each condition (1)-(4) is tested at each iteration, more than one condition can be activated in the same iteration although not all combinations are possible, for example if (1) is activated then (2) is not since a_{dc} descending implies a_w is 1. Out of all the possible combinations of repeated conditions (1)-(4), only four are ambiguous in whether h increases or decreases, see equation 3.30. We solve the ambiguities involving GPR and ER terms by imposing an increase on h when they

occur since this gives a higher weight on $\Delta\sigma_{dc}$ which is the update that is directly sensitive to the conductivity.

$$\begin{aligned} \dot{a}_{dc} \dot{\Theta}_{dc} \dot{\Theta}_w &> 1 \\ \dot{a}_{dc} \dot{\Theta}_w &> 1 \\ \dot{a}_w \dot{\Theta}_{dc} \dot{\Theta}_w &> 1 \\ \dot{a}_w \dot{\Theta}_w &\geq 1 \end{aligned} \tag{3.30}$$

In practice we treat h as an invisible variable and only worry about finding values for $\dot{a}_{dc}, \dot{a}_w, \dot{\Theta}_{dc}$ and $\dot{\Theta}_w$ which remain constant throughout the inversion. These values are found empirically. Table 3.3 displays the designated roles of values $\dot{a}_{dc}, \dot{a}_w, \dot{\Theta}_{dc}$ and $\dot{\Theta}_w$. Table 3.4 show the values used in our inversions for both low and high-conductivity scenarios.

The update for optimizing equation 3.25 is,

$$\boldsymbol{\sigma} \leftarrow \boldsymbol{\sigma} \odot \exp(\boldsymbol{\sigma} \odot \Delta\boldsymbol{\sigma}). \tag{3.31}$$

We summarize the procedure of computing the joint update $\Delta\boldsymbol{\sigma}$ together with weight h in Figure 3.5.

3.4 Examples

3.4.1 Subsurface models

We illustrate our algorithm with two possible scenarios of the subsurface: one with low conductivity (σ between 1 and 4mS/m) and one with high conductivity (σ between 5 and 20mS/m) as shown in Figure 3.8. The permittivity is kept equal (but assumed unknown) in both scenarios. We place a box of size 1×1 m present in both

a)

Joint conductivity update $\Delta\sigma$

- Compute a_w and a_{dc} with current h .
- Normalize $\Delta\sigma_w$ and $\Delta\sigma_{dc}$ by their largest amplitude and compute their geometric mean c .
- Compute $\Delta\sigma$,

$$\Delta\sigma = a_w \Delta\sigma_w + a_{dc} \Delta\sigma_{dc}.$$

- Normalize $\Delta\sigma$ by its largest amplitude and set,

$$\Delta\sigma \leftarrow c \Delta\sigma$$

- Check conditions (1)-(4) and update h .

b)

Conditions regulating h

- (1) If a_{dc} is decreasing,

$$h \leftarrow \dot{a}_{dc} h.$$

- (2) If a_w decreases,

$$h \leftarrow \dot{a}_w h.$$

- (3) If the value of Θ_{dc} increases,

$$h \leftarrow \dot{\Theta}_{dc} h.$$

- (4) If the value of Θ_w increases,

$$h \leftarrow \dot{\Theta}_w h.$$

Where $\dot{a}_{dc}, \dot{a}_w, \dot{\Theta}_w$ and $\dot{\Theta}_{dc}$ satisfy,

$$\dot{a}_{dc} > 1 \quad \dot{a}_{dc} \dot{\Theta}_{dc} \dot{\Theta}_w > 1$$

$$\dot{\Theta}_{dc} > 1 \quad \dot{a}_{dc} \dot{\Theta}_w > 1$$

$$\dot{a}_w > 1 \quad \dot{a}_w \dot{\Theta}_{dc} \dot{\Theta}_w > 1$$

$$\dot{\Theta}_w < 1 \quad \dot{a}_w \dot{\Theta}_w \leq 1$$

Figure 3.5: Algorithm for computing the update $\Delta\sigma$ as explained in Section Joint Inversion.

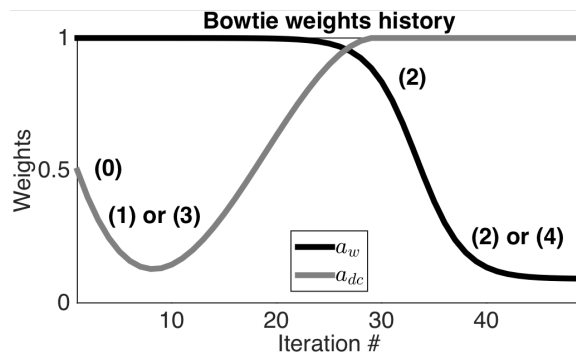


Figure 3.6: Diagram of weights a_w and a_{dc} as a function of iterations. An initial value for a_{dc} is chosen following condition (0). If a_{dc} decreases over iterations, or Θ_{dc} increases, condition (1), or (3), are activated to increase a_{dc} . Once a_{dc} reaches the value 1, a_w is forced to steadily decrease with condition (2). If $\Theta_{w,\sigma}$ increases over iterations, condition (4) is activated and a_w is increased but regulated by condition (2).

Table 3.3: Parameters for our joint inversions that were found empirically and remained fixed throughout the inversions. An increase in h favors $\Delta\sigma_{dc}$ more than $\Delta\sigma_w$. Conversely, a decrease in h favors $\Delta\sigma_w$ more than $\Delta\sigma_{dc}$.

Parameter	Role	Turn-on
initial a_{dc}	Initial weight on $\Delta\sigma_{dc}$	Only in first iteration
\dot{a}_{dc}	Increase h and a_{dc}	Only when $a_w = 1$
\dot{a}_w	Increase h , decrease a_w	Only when $a_{dc} = 1$
$\dot{\Theta}_{dc}$	Increase h , weigh $\Delta\sigma_{dc}$ more	Always
$\dot{\Theta}_w$	Decrease h , weigh $\Delta\sigma_w$ more	Always

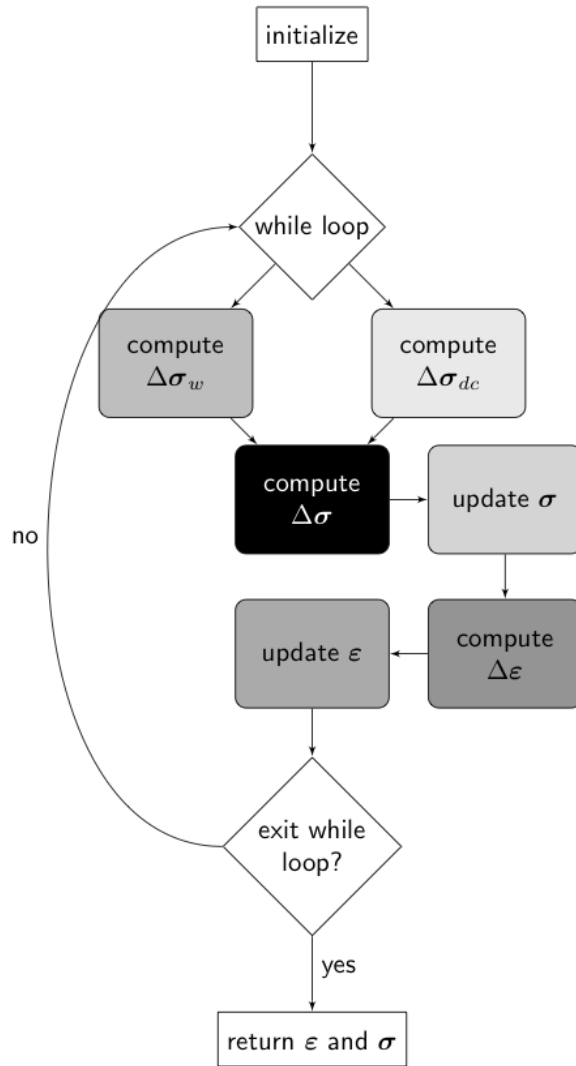


Figure 3.7: Joint inversion algorithm as explained in Section Joint Inversion.

Table 3.4: Inversion parameters used for the low and high-conductivity scenario.

Parameter	Low σ	High σ
initial a_{dc}	0.85	0.9
\dot{a}_{dc}	4	2
\dot{a}_w	2	1.5
$\dot{\Theta}_{dc}$	6	20
$\dot{\Theta}_w$	0.9	0.9

permittivity and conductivity, and a reflector at depth with a 1m thickness present only in the permittivity. We invert for both permittivity and conductivity starting from homogeneous background models: $\sigma = 1\text{mS/m}$ and $\sigma = 4\text{mS/m}$ for the low and high conductivity scenarios respectively and $\varepsilon = 4$ for both scenarios.

The choice for the size of the box in our models is intended to stress our inversions as much as possible: large enough to have two wavelengths of the electromagnetic wave pass through, but small enough to be just within the minimum resolution of our ER acquisition sensitivity. We show the usefulness of the method on an exploration scenario relevant for field applications and simple enough for interpretation and assessment of our method.

3.4.2 Data acquisition

The GPR data are synthetically generated by applying 20 equally spaced sources (with a Ricker wavelet signature of 250MHz) on the air-ground interface with source-receiver spaced a wavelength away ($\approx 0.5\text{m}$) and receiver-receiver distance a quarter of a wavelength away all along the air-ground interface. The ER data are also synthetically generated using 17 electrodes placed on the air-ground interface with one meter spacing between them and acquiring all possible dipole-dipole and Wenner

array configurations.

3.4.3 Noise

We add white noise to our synthetic GPR common-source gathers with amplitude 10% of the standard deviation of each common-source gather (see Figure 3.9). We then lowpass the data up to 70% of our Nyquist frequency, which is where most of the noise spectra is shared with our noise-free data. Since the synthetic ER data do not follow a Gaussian distribution, we first cluster the data and then add white noise to each cluster with an amplitude of 10% of the standard deviation of each cluster (see Figure 3.10). We note that the noisy dipole-dipole array gathers exhibit a significant lower signal-to-noise ratio than the noisy Wenner array gathers, although we still use all of our noisy data for our inversions.

3.4.4 GPR inversions

In Figure 3.11-a we see the recovered permittivity using just GPR data for the low conductivity scenario. We see the box correctly imaged and with values close to our true model while the bottom reflector is rightly imaged but the parameter value is not accurate because of amplitude loss in the data due to attenuation and two-way travel. We also observe low spatial frequency artifacts as a result of our surface source illumination with amplitudes dependent on the signal-to-noise ratio: with larger noise levels, the artifact amplitudes are recovered with a value closer to the permittivity of the box anomaly. For the high conductivity scenario (Figure 3.12-a) the amplitude loss in the GPR data is even greater yielding speckle artifacts near the box of only 7.5% between the permittivity of the background and the box.

The lack of amplitude information due to attenuation of the GPR data is also appreciated in the recovered conductivities using only the GPR inversion as seen in

Figure 3.13-**a** for the low conductivity and even more so in Figure 3.14-**a** for the high conductivity. We note that because of the non-uniqueness between reflectivity caused by conductivity and that caused by permittivity, the GPR conductivity solution detects an artifact apparent boundary at the bottom of the model. High spatial frequency artifacts are also present in the recovered low conductivity.

3.4.5 ER inversions

The ER recovered conductivities shown in Figures 3.13-**b** and 3.14-**b** for the low and high-conductivity scenarios tell a different story from the GPR inversions: they have a more accurate amplitude detection, contain more low spatial frequencies (both in the detection of the box and the artifacts of the inversion), and because the ER data are directly and only sensitive to conductivity they do not contain the bottom reflector. We note however that because of our one-sided surface acquisition geometry and the inherent depth resolution of ER, the amplitude of the box decays in depth.

3.4.6 Joint inversions

The joint inversion recovered conductivities for the low and high scenarios are shown in Figures 3.13-**c** and 3.14-**c** respectively. We note improvements in the parameter accuracy and spatial resolution of the recovered conductivities compared to the GPR and ER inversions as well as a better depth resolution of the box. In Table 3.5 we quantify the improvement of our joint inversion by dividing the zero-lag crosscorrelation of the true and recovered conductivities with the zero-lag autocorrelation of the true conductivities. In both the low and high-conductivity scenarios we see an improvement over the separate GPR and ER inversions. With respect to the GPR results, we improve by 3% and 5.4% in the low and high-conductivity scenarios respectively. With respect to the ER results, we improve by 0.11% in both the low and

high-conductivity scenarios.

Because of the non-uniqueness of conductivity and permittivity reflections in the GPR data, our joint inversion has the caveat of detecting apparent boundaries in the conductivity solution. We also note artifacts in our joint inversion conductivities reminiscent of the artifacts in the GPR recovered permittivity around the box-anomaly (Figure 3.11-a) although because of our weighting scheme that penalizes $\Delta\sigma_w$ in later iterations, these artifacts diminish amplitude as the number of iterations increase.

In the low conductivity scenario, Figure 3.15-a shows that the GPR data dominates $\Delta\sigma$ for the first 4 iterations resolving sharp boundaries at shallow depths that $\Delta\sigma_{dc}$ is not yet sensitive to. However as iterations increase, $\Delta\sigma_w$ has contributed enough sensitivity for $\Delta\sigma_{dc}$ to resolve at depth and so the ER data dominates the inversion resolving the box and smoothing GPR high spatial frequency artifacts while still letting $\Delta\sigma_w$ contribute to the inversion. As shown in Figure 3.15-b the first 20 iterations resolve the data at a faster pace than in later iterations.

Similar to the low-conductivity scenario, the ER data dominates most of the inversion as can be seen in Figure 3.16-a. Figure 3.16-b shows a similar decrease of Θ_{dc} as in Figure 3.15-b although Θ_w struggles to find a descent direction until the 40th iteration where both Θ_w and Θ_{dc} take a final descending stretch.

Because of the lack of information about the subsurface in the GPR data due to strong attenuation, the confidence of Θ_w in resolving the data is weak. The weak confidence of the GPR data is also seen in the small curvature of Θ_w : the changes in Θ_w are small compared to the low conductivity scenario (Figure 3.15-b), and the step sizes α_ϵ flip back and forth between positive and negative values throughout the inversion (not shown). The lack of curvature in Θ_w for the high conductivity

Table 3.5: Ratio of maximum zero-lag cross-correlation between recovered and observed parameters for the low and high-conductivity scenarios. Closer to 1 is better. The joint inversion outperforms the GPR and ER recovered conductivities.

Inversion	low σ	high σ
GPR	0.8685	0.8432
ER	0.8964	0.8963
Joint	0.8975	0.8974

scenario leads us to conclude that incorporating ER sensitivity to $\Delta\sigma_w$ is not enough to resolve permittivity.

In order to increase the resolution of permittivity values in the case of high conductivity, four possible solutions could be 1) using the low frequency information of the GPR in either a stepped frequency approach as in Meles *et al.* (2012); 2) changing the objective function in early iterations as in Bozdağ *et al.* (2011) or Ernst *et al.* (2007b) to allow for lower frequency content to be imprinted in both $\Delta\epsilon$ and $\Delta\sigma_w$; 3) assuming the permittivity and conductivity geometric features are similar and using a cross-gradient approach as in Haber & Gazit (2013); Gallardo & Meju (2003) or 4) a joint update approach similar to equation 3.26 where instead of joining the GPR and ER conductivity sensitivities we join the permittivity ($\Delta\epsilon$) and joint conductivity ($\Delta\sigma$) updates.

In Chapter 4 we improve the resolution of our algorithm by incorporating the envelope of the GPR data and using the cross-gradients constraint in a single objective function.

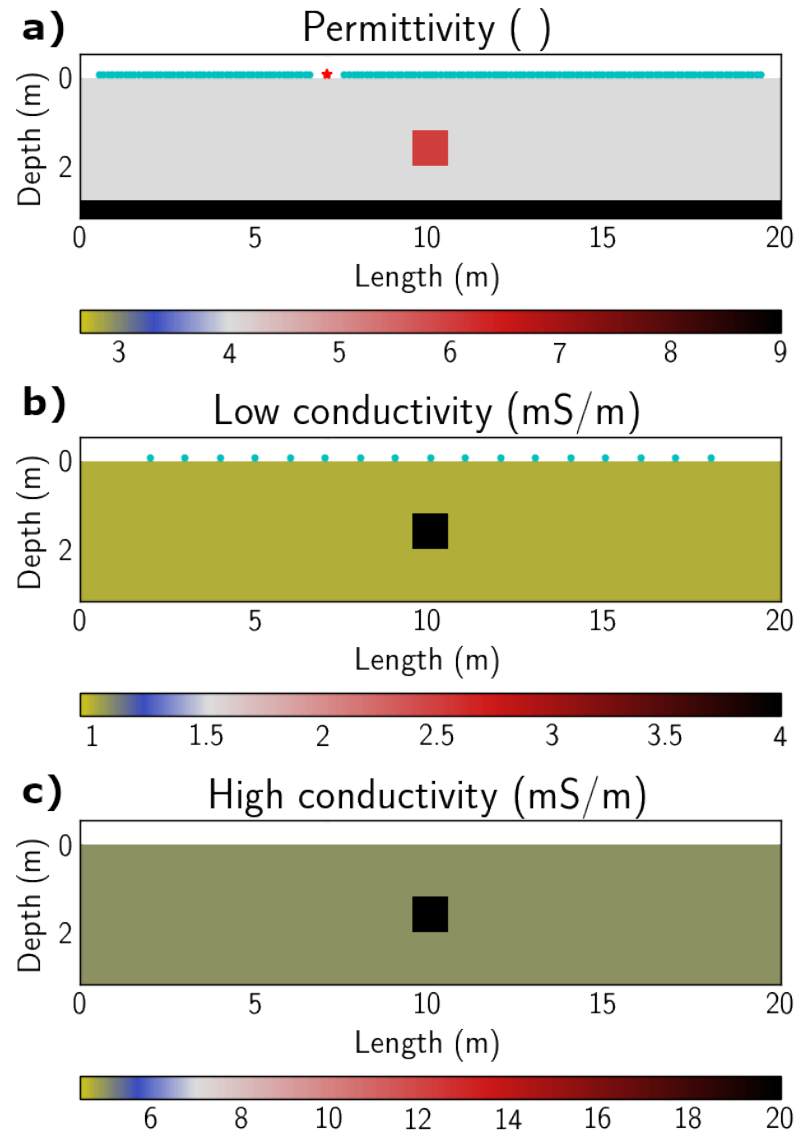


Figure 3.8: Subsurface models used for our inversions. The size of the box is $1 \times 1\text{m}$. a The permittivity background, bottom reflector and box have values of 4, 9 and 6 respectively. The conductivity background and box have values of 1 and 4 mS/m for the low conductivity b and 4 and 20 mS/m for the high conductivity c respectively. An example of GPR receivers and source are depicted in green and red in b and ER electrodes are depicted in green in c.

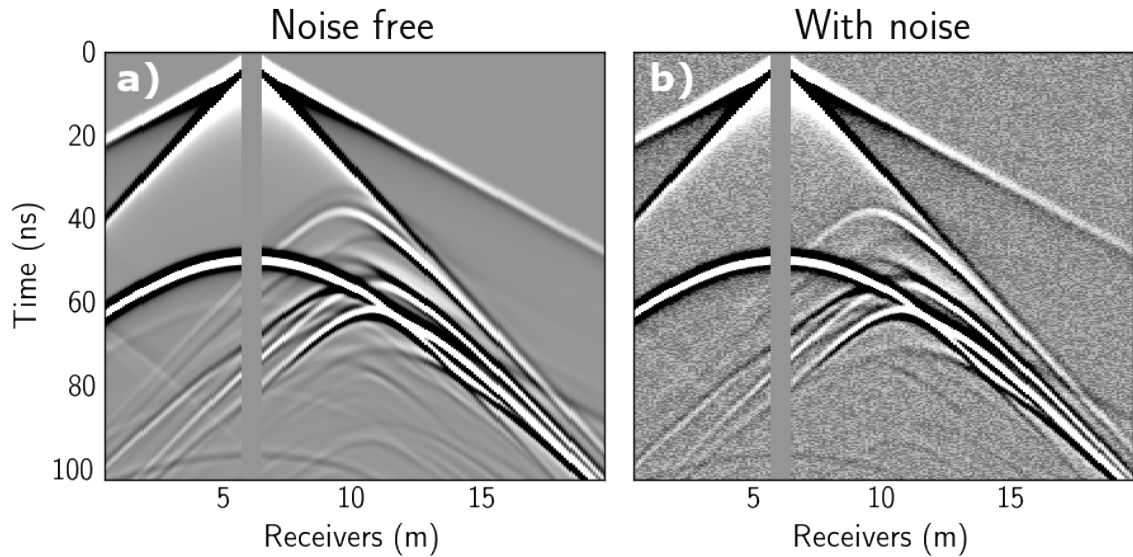


Figure 3.9: GPR data for one source noise free and with added noise.

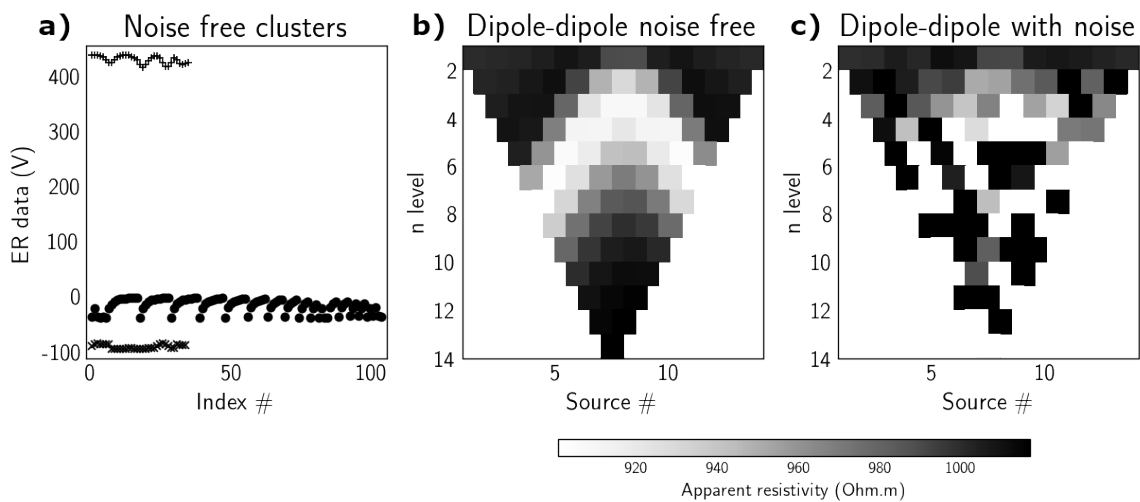


Figure 3.10: a All ER data noise free and the clusters used for adding noise depicted with symbols +, ●, and ✕. b Pseudo-section of a dipole-dipole survey noise free and c with added noise.

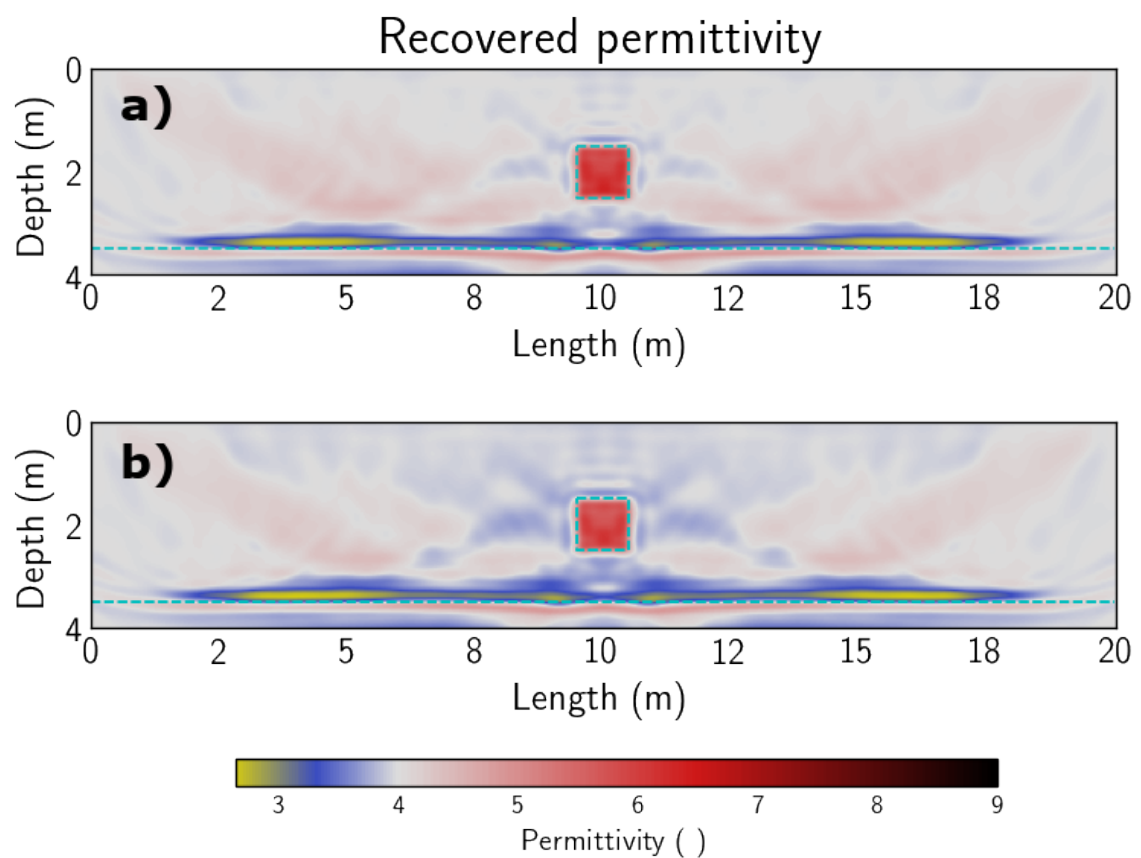


Figure 3.11: Recovered permittivity for the low-conductivity scenario with just GPR data a and with GPR and ER data b.

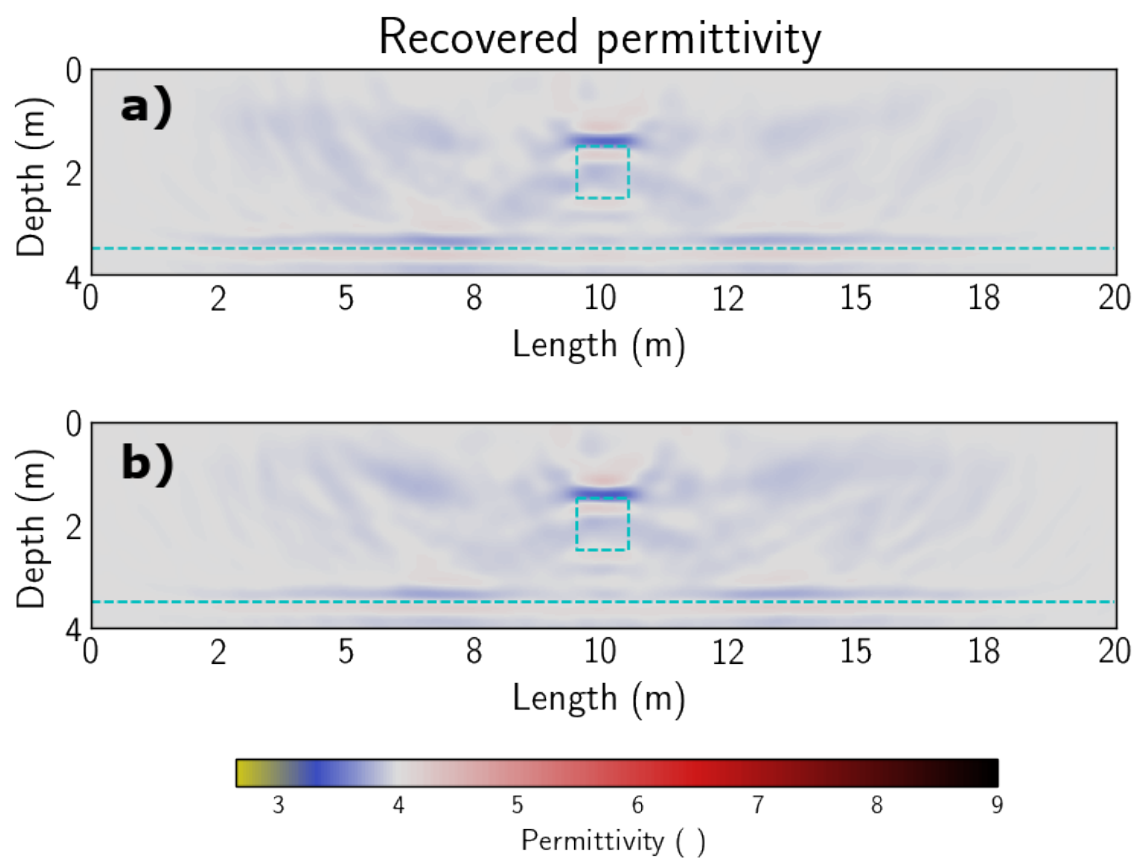


Figure 3.12: Recovered permittivity for the high-conductivity scenario with just GPR data a and with GPR and ER data b.

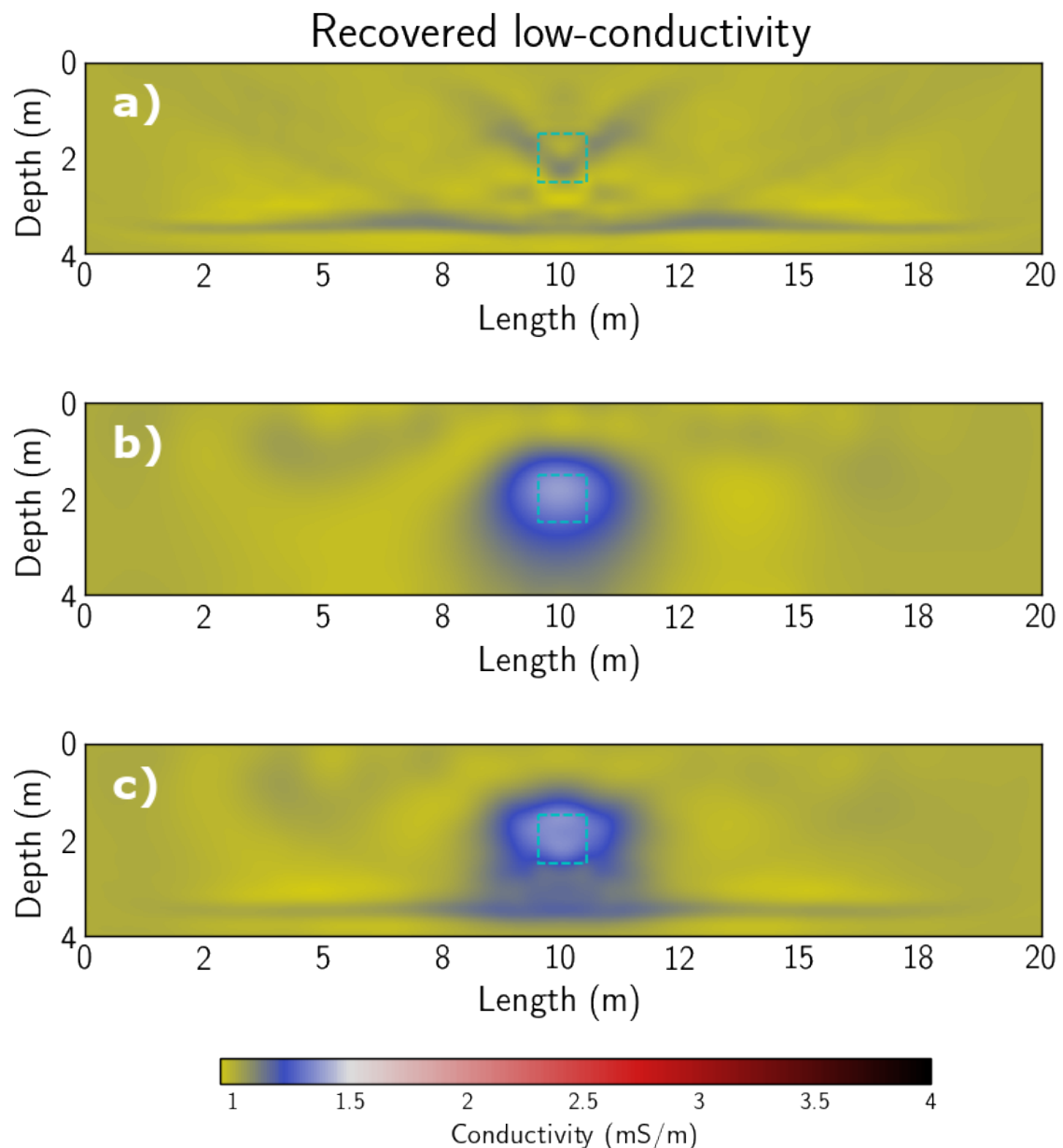


Figure 3.13: Recovered low conductivity using a just GPR data, b just ER data, and c both GPR and ER data. Each inversion was run for 50 iterations.

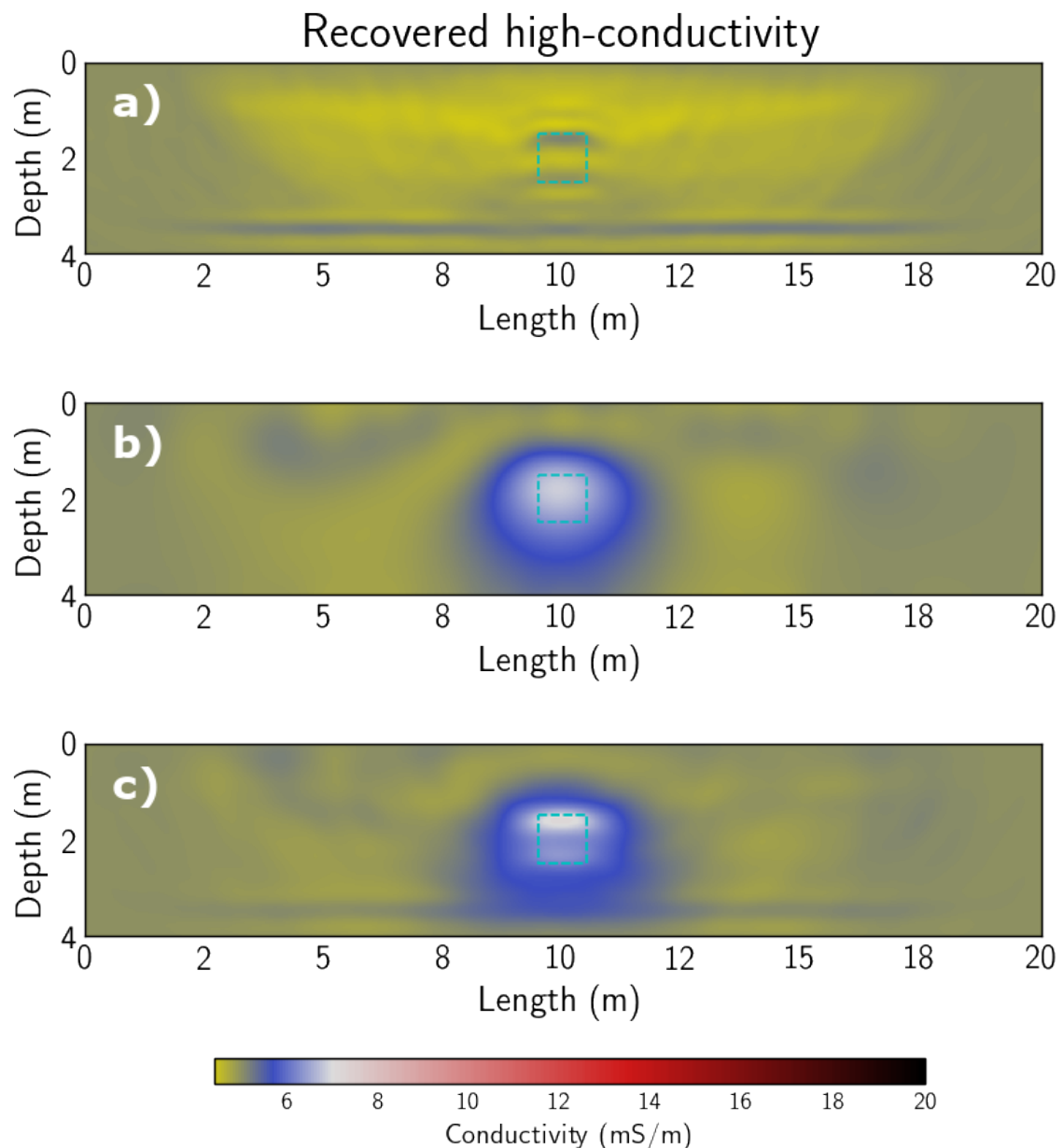


Figure 3.14: Recovered high conductivity using a just GPR data, b just ER data, and c both GPR and ER data. Each inversion was run for 50 iterations.

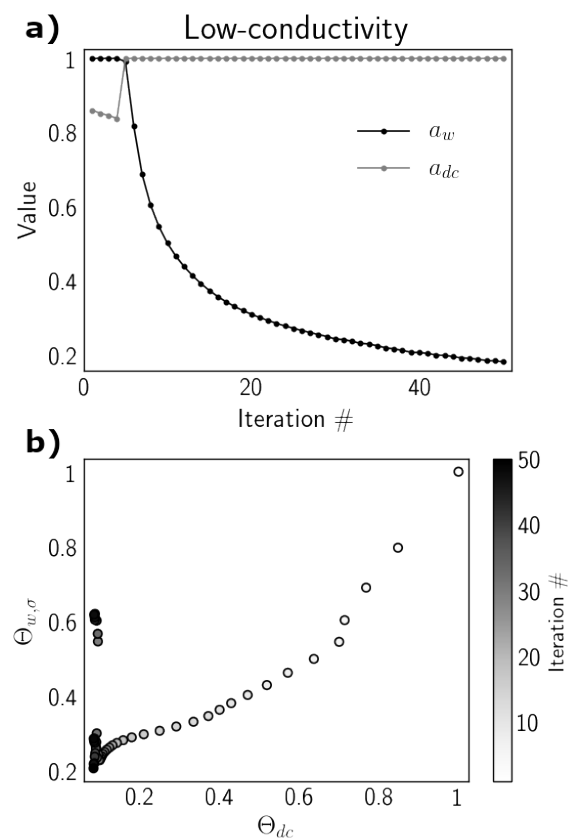


Figure 3.15: Update weights history over iterations for the low-conductivity scenarios a and normalized objective functions history over iterations d.

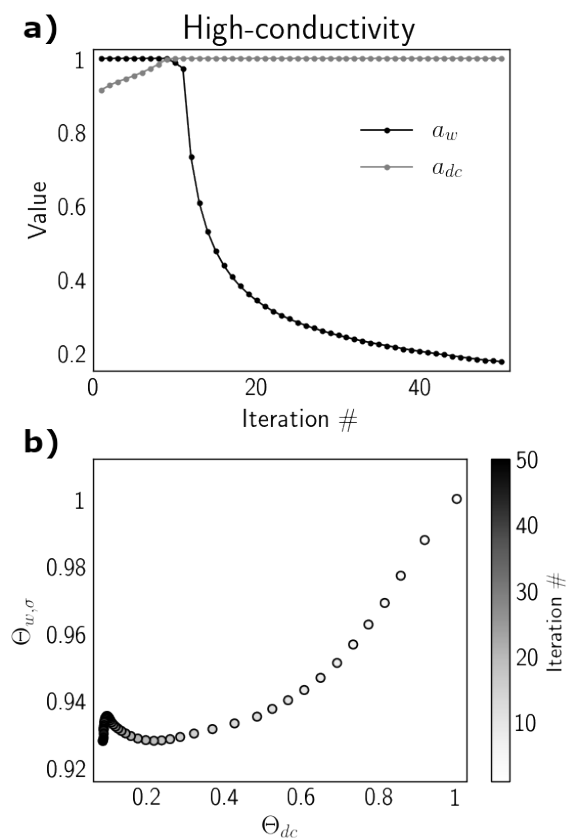


Figure 3.16: Update weights history over iterations for the high-conductivity scenarios a and normalized objective functions history over iterations d.

3.5 Conclusions

We have developed a joint inversion algorithm for recovering subsurface frequency independent electrical permittivity and conductivity with surface acquisition and no assumed geometry or structure of the target media that enhances the sensitivity of the ground penetrating radar (GPR) and electrical resistivity (ER) data by introducing low and high spatial frequency information while honoring the physics of Maxwell equations. Our joint inversion approach improves both the frequency independent permittivity and conductivity spatial and amplitude resolution of the target media compared with just GPR or ER inversions. Moreover, we find that GPR effectively supports ER in regions of low conductivity while ER supports GPR in regions with strong attenuation.

We perform an iterative non-linear inversion where the GPR and ER sensitivities are computed with the adjoint method and the conductivity GPR and ER sensitivities are joined with an ad-hoc method with the paradigm of letting both sensitivities always contribute to the inversion in proportion to how well their respective data are being resolved in each iteration. Our weighting method makes use of five fixed user defined values that further regulate the GPR and ER conductivity sensitivities automatically in each iteration, and that rely on the physical resolution of the GPR and ER experiments. Because our ad-hoc method to join the GPR and ER sensitivities is based on the value of the objective function values and the physical resolution of our geophysical methods, we suggest it can be used for joining other geophysical exploration methods where the physics involved play a similar role, e.g. active source seismic and gravity which are linked by density.

We assume the subsurface media is linear, isotropic, two dimensional and with

frequency independent electrical parameters. In an effort to relax a-priori knowledge of the subsurface we do not use any petrophysical relationships throughout our work. These assumptions were chosen as a compromise between ease of computation cost and relevance with field data scenarios. Moreover, we note that for a variety of earth materials the DC and effective conductivity differ by a factor of less than an order of magnitude. Our assumptions enable us to directly couple the electrical conductivity sensitivities that the GPR and ER data are sensitive to. While frequency independent parameters are not realistic in general, it serves as a starting point for testing our algorithm and motivates the development of forward models and inversion schemes that do take into account frequency dependency of electrical parameters.

In order to benchmark our algorithm we simulate GPR and ER data on two subsurface models, one with low (in the order of 10mS/m or less) and one with high (in the order of more than 10mS/m) conductivity. The low conductivity model was designed to test our algorithm in a case where the recovered permittivity is sufficiently resolved by the GPR data alone while the conductivity is only meaningfully recovered by the ER data. The high conductivity model was designed to test for a case where the GPR data alone cannot resolve a meaningful image of either permittivity or conductivity. Sources and receivers were placed on the air-ground interface simulating a real-data acquisition scenario for both GPR and ER experiments.

In both cases our joint inversion approach improves the resolution of spatial dimensions and amplitude of the target conductivity from just GPR and ER inversions. The spatial detection is measured as a ratio of zero-lag cross-correlations between true and recovered parameters. It is improved by 3% and 5.4% with respect to the GPR inversions in the low and high-conductivity scenarios respectively, and by 0.11% in

both scenarios with respect to the ER inversions.

Because of the non-uniqueness between permittivity and conductivity reflections in the GPR data, our joint inversion scheme introduces apparent boundaries in the recovered conductivity that are not corrected with the ER data. High spatial frequency artifacts of the GPR sensitivity to the conductivity are mapped into our joint inversion solution, although these artifacts can be diminished in amplitude if the inversion is run for more iterations allowing for the low spatial frequency ER sensitivity to correct them. In both low and high conductivity scenarios the recovered permittivity is not enhanced by using the ER sensitivity to conductivity, which can be of particular interest in the high conductivity case where permittivity is poorly solved by the GPR inversion.

Given the poor amplitude detection of the permittivity in the high conductivity scenario, approaches to increase the permittivity solution should likely 1) exploit low frequency content of the GPR data and 2) assume structural similarities of permittivity and conductivity. A possible path to enhance low frequency sensitivity of the GPR data could involve changing the objective function of the GPR inversion in early iterations or sequentially increase the frequency content of the GPR data during the inversion. If structural similarities between permittivity and conductivity are assumed, possible paths to accomplish 2) could be joining the conductivity sensitivities of the GPR and ER data in a cross-gradient scheme, or with a similar approach as presented in this paper for joining the GPR and ER conductivity sensitivities. In Chapter 4 we address 1) and 2) by enhancing our joint inversion with the envelope transform of the GPR data and cross-gradient constraints on both permittivity and conductivity.

Allowing for deeper spatial sensitivity for the ER experiment is equivalent to using long one-sided surface acquisition. In order to recover low frequencies and enough amplitude information from the GPR experiment, long one-sided surface acquisition of multi-offset data are needed. Given that our joint update for the conductivity assumes both updates are in the same spatial coordinates and with the same discretization, the cost for computing the GPR and ER forward models is increased from conventional GPR or ER experiments and inversion schemes. As a result, long offsets for both experiments are needed, yielding our approach best suited for shallow subsurface investigation.

Inverting for subsurface electrical properties using full-waveform of GPR data with data acquired on the surface is a new and emerging method. Choosing to carefully study synthetic examples where the solution is known enables us to assess the attributes and limitations of our method. This is an important step before using field data with our method because, in general, the solution of subsurface electrical parameters is unknown.

CHAPTER 4:

ENHANCING LOW FREQUENCY AND EXPLOITING STRUCTURAL SIMILARITIES

¹ Recovering material properties of the subsurface using ground penetrating radar (GPR) in the presence of strong attenuation and weak low frequencies in the data is a challenging problem. We propose three non-linear inverse methods for recovering electrical conductivity and permittivity of the subsurface by joining GPR and electrical resistivity (ER) data acquired at the surface. All methods use ER data to constrain the low spatial-frequency of the conductivity solution. The first method uses the envelope of the GPR data to exploit low frequency content in full-waveform inversion and does not assume structural similarities of material properties. The second method uses cross-gradients to manage weak amplitudes in the GPR data by assuming structural similarities between permittivity and conductivity. The third method uses both the envelope of the GPR data and the cross-gradient of the model parameters. By joining ER and GPR data, exploiting low frequency content in the GPR data, and assuming structural similarities between electrical permittivity and conductivity we are able to recover subsurface parameters in regions where the GPR data has a signal-to-noise ratio close to one.

¹This chapter has been submitted to *Geophysics* and is currently under review. Domenzain *et al.* (2019b)

4.1 Introduction

Electrical properties in the subsurface such as electrical permittivity ε and conductivity σ , hold relevant information regarding short, medium and long-term human needs. In many of these applications surface data acquisition of active source methods such as electrical resistivity (ER) and ground penetrating radar (GPR) can prove to have a lower and more feasible deployment cost when compared with borehole methods.

ER is sensitive only to electrical conductivity while GPR is sensitive to electrical permittivity by reflectivity and velocity, and conductivity by attenuation and reflection of the excited electromagnetic wave. Full-waveform inversion (FWI) of GPR data is an emerging technique for enhancing the resolution of electrical properties with little a-priori knowledge of the subsurface geometry with the caveat of needing an initial ray-based tomography for robust initial models (Ernst *et al.*, 2007a). However, inverting with only surface acquired GPR data remains a challenge and thus limits most of the current applications in which GPR is commonly used.

Similar to seismic full-waveform inversion, two main challenges that must be resolved for GPR-FWI are the lack of low frequencies and the presence of attenuation in the data. Fortunately, ER can be used to enhance GPR because it is directly sensitive to low spatial frequencies in electrical conductivity and is directly linked to the GPR governing physics by Maxwell's equations. In this work we combine the two methods and make the assumption that electrical properties are not frequency dependent. Although this is not realistic in general, in Chapter 3 we note that for a variety of relevant earth materials, the (real) effective conductivity and the DC conductivity differ by a factor of less than 5. Hence, assuming frequency independent electrical parameters serves as a starting point to test the enhancement of the spatial

resolution in our inversions.

In Chapter 3 we developed a joint inversion scheme of GPR and ER data that uses the full physics of Maxwell’s equations. The inversion accounts for the sensitivities of GPR and ER data in each iteration of an adjoint method based inversion. We tested our joint inversion scheme in two synthetic examples showing enhancements when compared to individual GPR and ER inversions. The recovered conductivity was improved through joint inversion because the ER data improved amplitude resolution and the GPR constrained high spatial-frequency content.

In this work we address joint inversion of GPR and ER data when the conductivity in the subsurface is strong. Unfortunately, if the attenuation is too strong the GPR data will miss reflection events that hold meaningful information of the subsurface. In this situation we find that even though the recovered conductivity is better resolved by using both GPR and ER data, the recovered permittivity lacks the correct amplitude and misses long wavelength resolution.

Fortunately, methods developed for seismic FWI (Bozdağ *et al.*, 2011; Liu & Zhang, 2017) can be used to enhance low frequency content in GPR-FWI. In the context of seismic FWI it is well known that low frequencies in the waveform data help the inversion avoid local minima (Virieux & Operto, 2009; Baeten *et al.*, 2013). In Bozdağ *et al.* (2011) the authors propose using the analytic signal of the observed waveform in order to isolate the instantaneous phase and amplitude (i.e. envelope) information of the data and modify the FWI objective function accordingly. In Liu & Zhang (2017) the authors join first arrival travel-time with early arrival envelope data to build a rich low spatial-frequency initial velocity model that is then used in the FWI routine. Both works find that the low frequency content of the envelope

waveform data is good for enhancing the low frequency spatial content of the recovered velocity. In this work we use the envelope waveform data of GPR and further join it with ER data to alleviate low spatial frequencies in both electrical permittivity and conductivity.

Inversion methods that assume structural similarities of the target subsurface parameters (Haber & Oldenburg, 1997; Gallardo & Meju, 2003) can be used to further improve our joint inversion algorithm by letting the ER data inform the GPR data in regions of high attenuation. Assuming structural similarities in target subsurface parameters allows different geophysical data with varying spatial and physical sensitivities inform each other where to look for a solution that more accurately resembles reality if the structural similarity holds true. In Gallardo & Meju (2003) the authors choose the cross-gradient operator as a structural constraint and successfully apply it to real seismic and ER data. In this work we show that by assuming structural similarities between electrical permittivity and conductivity we can use the cross-gradient operator for filling in amplitude and spatial-frequency content to our solutions while still using forward and inverse models that take into account the full physics of Maxwell's equations.

Since then different types of geophysical data have been used in this context (Gallardo & Meju, 2007; Fregoso & Gallardo, 2009; Gross, 2019). Most relevant to our study are the works of Linde *et al.* (2006) and Doetsch *et al.* (2010) which use borehole GPR and ER data to solve for electrical permittivity and conductivity. All of these works rely on a linearization of one or both forward models and clear access to the sensitivity matrices of the data, which in the case of time-domain FWI the latter is computationally expensive. In Hu *et al.* (2009) the authors combine

seismic and controlled-source electromagnetic data to solve for compressional velocity and electrical conductivity in a Gauss-Newton inversion while enforcing the cross-gradient constraint. They employ adjoint based methods for computing the sensitivity matrices of the data with the computational burden of storing and inverting the Hessian of the objective functions. In this work we compute the gradients of the objective functions using adjoint based methods and relieve the need to store and compute the Hessian of the objective functions.

We begin with a brief review of the physics of the forward models for GPR and ER and objective functions for the GPR and ER inversions. Then we review our joint inversion scheme from Chapter 3 and define three new joint inversion schemes designed to manage attenuation and enhance low frequencies. Finally we test our joint inversions on synthetic subsurface models designed to challenge the spatial and amplitude resolution of GPR and ER sensitivities.

4.2 GPR and ER forward models and inversions

We briefly recall the governing equations, forward models and objective functions for the GPR and ER experiments. Our physical models assume isotropic physical properties and a 2d subsurface geometry where the parameters are constant along the y -axis. These assumptions are made for ease of computations of our forward models and not crucial for our inversion schemes. Both the GPR and ER forward models are discretized on the same computational grid. Gradients of the objective function with respect to the parameters are given in Chapter 3 and a full discussion is found in Chapter 3.

4.2.1 Ground penetrating radar

The physics of the GPR experiment are given by,

$$\begin{pmatrix} \mu_o & 0 & 0 \\ 0 & \mu_o & 0 \\ 0 & 0 & \varepsilon \end{pmatrix} \begin{pmatrix} \dot{H}_z \\ -\dot{H}_x \\ \dot{u} \end{pmatrix} = \begin{pmatrix} 0 & 0 & \partial_x \\ 0 & 0 & \partial_z \\ \partial_x & \partial_z & 0 \end{pmatrix} \begin{pmatrix} H_z \\ -H_x \\ u \end{pmatrix} - \sigma \begin{pmatrix} 0 \\ 0 \\ u \end{pmatrix} + \begin{pmatrix} 0 \\ 0 \\ -J_y \end{pmatrix}, \quad (4.1)$$

where u is the electric field component in the y direction, (H_x, H_z) are the magnetic field components in the x and z direction, J_y is the source term, ε is the electric permittivity, σ is the electric conductivity and μ_o is the magnetic permeability which we assume constant and equal to the permeability of free space. We discretize equation 4.1 by

$$\begin{aligned} \mathbf{u} &= \mathbf{L}_w \mathbf{s}_w, \\ \mathbf{d}_w^s &= \mathbf{M}_w \mathbf{u} \end{aligned} \quad (4.2)$$

where \mathbf{L}_w is the discretized differential (time marching) operator of equation 4.1, \mathbf{u} is the electric field y component defined in space and time, \mathbf{s}_w is the source term, \mathbf{M}_w is the measuring operator, and $\mathbf{d}_w^s = \mathbf{M}_w \mathbf{u}$ is the data of the experiment, i.e. a common-source gather. The discretized solution of equation 4.2 is described in detail in Chapter 3.

We make note that from this point forward we will refer to operators and variables in capital and lower case letters respectively, and distinguish continuous and discrete

mathematics in normal and bold font respectively. A complete table of relevant notation can be found in Table 4.1.

4.2.2 Electrical resistivity

The physics of the ER experiment are given by the steady state Maxwell's equations where Ohm's law holds (Pidlisecky *et al.*, 2007),

$$-\nabla \cdot \sigma \nabla \varphi = \mathbf{i}(\delta(x - s_+) - \delta(x - s_-)), \quad (4.3)$$

where φ is the electric potential, \mathbf{i} is the current intensity and s_{\pm} is the source-sink position. We write the discretized version of equation 4.3 as,

$$\begin{aligned} \mathbf{L}_{dc}\boldsymbol{\varphi} &= \mathbf{s}_{dc}, \\ \mathbf{d}_{dc}^s &= \mathbf{M}_{dc}\boldsymbol{\varphi}, \end{aligned} \quad (4.4)$$

where \mathbf{L}_{dc} is the discretized differential operator of equation 4.3, $\boldsymbol{\varphi}$ is the electric potential, \mathbf{s}_{dc} is the source term, \mathbf{M}_{dc} is the measuring operator that computes observed voltages, and \mathbf{d}_{dc}^s is the data of the experiment for one source. The discretized solution of equation 4.4 is described in detail in Chapter 3.

4.2.3 GPR inversion

The GPR inversion algorithm finds parameters $\boldsymbol{\varepsilon}_*$ and $\boldsymbol{\sigma}_*$ that satisfy,

$$\{\boldsymbol{\varepsilon}_*, \boldsymbol{\sigma}_*\} = \arg \min \Theta_w(\boldsymbol{\varepsilon}, \boldsymbol{\sigma}; \mathbf{d}_w^o), \quad (4.5)$$

where the subscript * denotes the imaged parameters and \mathbf{d}_w^o denotes all the observed GPR data. From now on we denote the electrical permittivity and conductivity in

Table 4.1: Reference for the notation used in the discretized inverse problems. Symbols common in both GPR and ER experiments are stripped from their subscripts to avoid clutter.

Symbol	Meaning	Note
ε	Discretized relative permittivity	
σ	Discretized conductivity	
\mathbf{L}	Discretized differential operator	
\mathbf{s}	Discretized source	
\mathbf{M}	Discretized measuring operator	
\mathbf{d}	Synthetic data	Used for GPR and ER
\mathbf{e}	Residual of synthetic vs observed data	
Θ	Objective function	
\mathbf{v}	Discretized adjoint field	
\mathbf{g}	Gradient of objective function	
α	Step size for \mathbf{g}	
\mathbf{u}	Electric wavefield on the y component	
$\dot{\mathbf{u}}$	finite-difference time derivative of \mathbf{u}	Only GPR
$\Delta\sigma_w$	GPR conductivity update	
$\Delta\varepsilon$	GPR permittivity update	
β	GPR envelope weight	
φ	Electric potential	
\mathbf{S}_{dc}	The matrix $-((\nabla_\sigma \mathbf{L}_{dc})\varphi)^\top$	Only ER
$\Delta\sigma_{dc}$	ER conductivity update	
$\Delta\sigma$	Joint conductivity update	
a_w, a_{dc}	Weights to regulate $\Delta\sigma_w$ and $\Delta\sigma_{dc}$	
c	Step size for $\Delta\sigma$	Used for the joint update
$\Delta\sigma_{\tau,o}$	Cross-gradient conductivity update	
$\Delta\varepsilon_{\tau,o}$	Cross-gradient permittivity update	
b_ε, b_σ	Weights to regulate $\Delta\varepsilon_{\tau,o}$ and $\Delta\sigma_{\tau,o}$	

bold font to emphasize these parameters are discretized and in matrix form. We have,

$$\Theta_w = \frac{1}{n_s} \sum_s \Theta_w^s, \quad (4.6)$$

where s indexes the sources, n_s denotes the total number of sources, and

$$\Theta_w^s = \frac{\|\mathbf{e}_w\|_2^2}{\|\mathbf{d}_w^{o,s}\|_2^2}, \quad (4.7)$$

where $\mathbf{d}_w^{o,s}$ is the observed data for one source and $\mathbf{e}_w = \mathbf{d}_w^s - \mathbf{d}_w^{o,s}$ is the residual of the modeled and observed data. The details for computing the gradient of Θ_w with respect to $\boldsymbol{\varepsilon}$ and $\boldsymbol{\sigma}$ can be found in Chapter 3.

4.2.4 ER inversion

The ER inversion algorithm finds $\boldsymbol{\sigma}_*$ that satisfies,

$$\boldsymbol{\sigma}_* = \arg \min \Theta_{dc}(\boldsymbol{\sigma}; \mathbf{d}_{dc}^o), \quad (4.8)$$

where \mathbf{d}_{dc}^o is all of the ER data. We have,

$$\Theta_{dc} = \frac{1}{n_s} \sum_s \Theta_{dc}^s, \quad (4.9)$$

where s indexes the source, n_s denotes the total number of sources, and

$$\Theta_{dc}^s = \frac{\|\mathbf{e}_{dc}\|_2^2}{\|\mathbf{d}_{dc}^{o,s}\|_2^2}. \quad (4.10)$$

We denote $\mathbf{d}_{dc}^{o,s}$ the observed data for one source and $\mathbf{e}_{dc} = \mathbf{d}_{dc}^s - \mathbf{d}_{dc}^{o,s}$ the residual of the modeled and observed data. The details for computing the gradient of Θ_{dc} with

respect to $\boldsymbol{\sigma}$ can be found in Chapter 3.

4.3 Joint inversions

4.3.1 Joint inversion of ER and GPR data

The objective function for our joint inversion is,

$$\{\boldsymbol{\varepsilon}_*, \boldsymbol{\sigma}_*\} = \arg \min \Theta_w(\boldsymbol{\varepsilon}, \boldsymbol{\sigma}; \mathbf{d}_w^o) + \Theta_{dc}(\boldsymbol{\sigma}; \mathbf{d}_{dc}^o). \quad (4.11)$$

We optimize 4.11 using gradient descent by first computing the descent directions for $\boldsymbol{\sigma}$: $\Delta\boldsymbol{\sigma}_w$ and $\Delta\boldsymbol{\sigma}_{dc}$ for both Θ_w and Θ_{dc} respectively, and then take a weighted average of these descent directions to update $\boldsymbol{\sigma}$; we then compute the descent direction $\Delta\boldsymbol{\varepsilon}$ and update $\boldsymbol{\varepsilon}$. Figure 4.1 shows a code-flow diagram of this process. We follow Chapter 3 and briefly explain how these updates and joining-weights are computed.

After all the gradients for all sources are computed the update directions are,

$$\Delta\boldsymbol{\sigma}_w = -\frac{1}{n_w} \sum_{s=1}^{n_w} \alpha_\sigma \mathbf{g}_{w,\sigma}, \quad (4.12)$$

$$\Delta\boldsymbol{\sigma}_{dc} = -\frac{1}{n_{dc}} \sum_{s=1}^{n_{dc}} \alpha_{dc} \mathbf{g}_{dc}, \quad (4.13)$$

$$\Delta\boldsymbol{\varepsilon} = -\frac{1}{n_w} \sum_{s=1}^{n_w} \alpha_\varepsilon \mathbf{g}_\varepsilon, \quad (4.14)$$

where α_σ , α_{dc} , and α_ε are computed as in Chapter 3. After $\Delta\boldsymbol{\sigma}_w$ and $\Delta\boldsymbol{\sigma}_{dc}$ have been computed they are joined by weights a_w and a_{dc} ,

$$\Delta\boldsymbol{\sigma} = a_w \Delta\boldsymbol{\sigma}_w + a_{dc} \Delta\boldsymbol{\sigma}_{dc}, \quad (4.15)$$

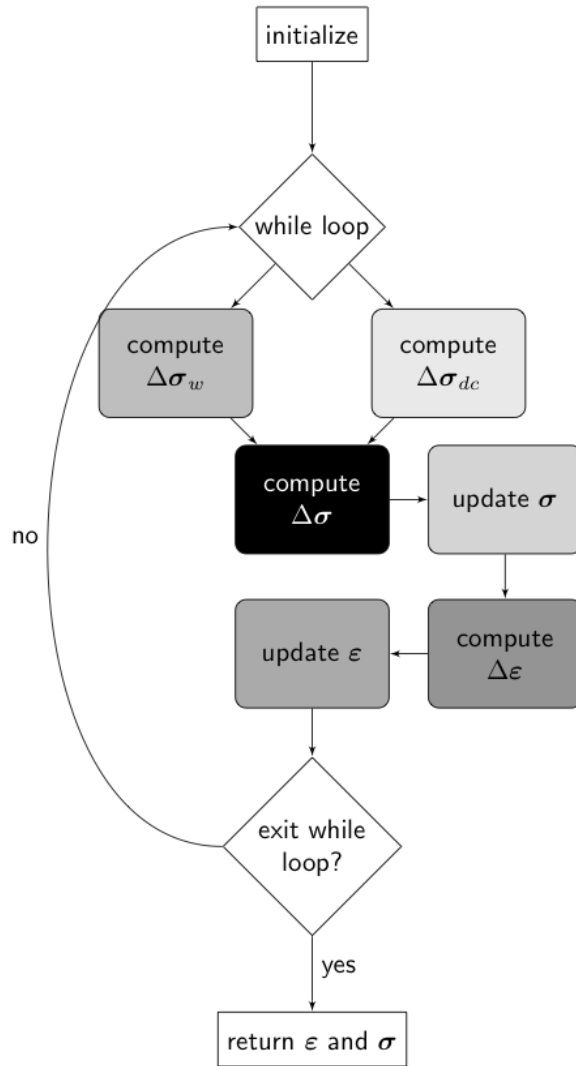


Figure 4.1: Inversion algorithm for Joint and JEN. We differentiate Joint and JEN by how we compute $\Delta\sigma_w$ and $\Delta\epsilon$.

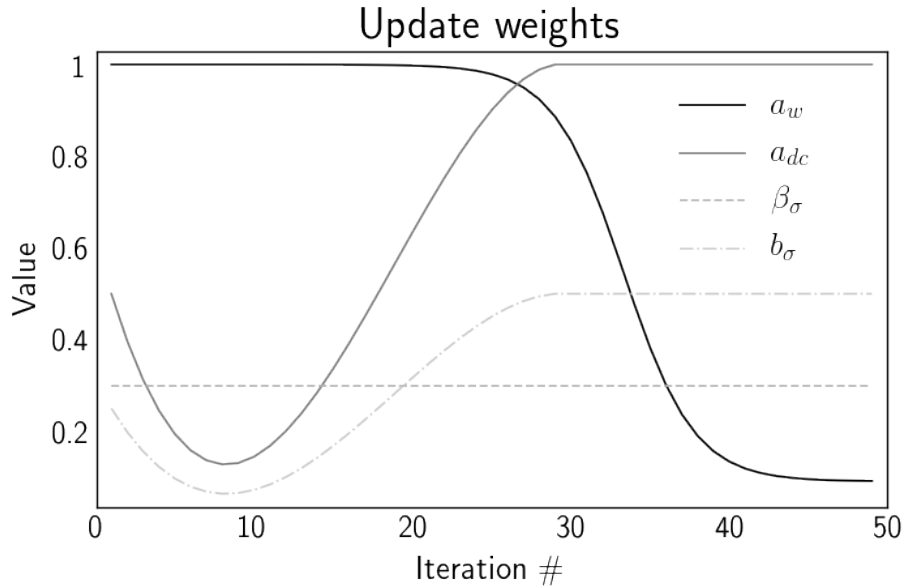


Figure 4.2: Qualitative optimal shape for weights throughout iterations for all inversion schemes (Joint, JEN, JOIX and JENX).

we then normalize $\Delta\boldsymbol{\sigma}$ by its largest amplitude and finally write,

$$\Delta\boldsymbol{\sigma} \leftarrow c \Delta\boldsymbol{\sigma}, \quad (4.16)$$

where c is the geometric mean of the maximum amplitudes of $\Delta\boldsymbol{\sigma}_w$ and $\Delta\boldsymbol{\sigma}_{dc}$ prior to normalization. The driving purpose of the weights a_w and a_{dc} is of letting both updates $\Delta\boldsymbol{\sigma}_w$ and $\Delta\boldsymbol{\sigma}_{dc}$ always contribute to $\Delta\boldsymbol{\sigma}$ in proportion to their objective function value at a given iteration. Figure 4.2 shows the shape as a function of iterations of the weights a_w and a_{dc} should have: a bow-tie shape where at early iterations a_w dominates and at later iterations a_{dc} takes over. For a full discussion on the weights a_w and a_{dc} see Chapter 3.

In order to enforce positivity constraints the parameters are updated as,

$$\boldsymbol{\sigma} \leftarrow \boldsymbol{\sigma} \odot \exp(\boldsymbol{\sigma} \odot \Delta\boldsymbol{\sigma}), \quad (4.17)$$

$$\boldsymbol{\varepsilon} \leftarrow \boldsymbol{\varepsilon} \odot \exp(\boldsymbol{\varepsilon} \odot \Delta\boldsymbol{\varepsilon}). \quad (4.18)$$

We will refer to this inversion method (i.e. optimizing equation 4.11) as Joint inversion (Joint).

4.3.2 Joint inversion of GPR envelope and ER data

We begin with a description of GPR envelope inversion which exploits the low frequency content of the GPR data. Similar to GPR inversion we find $\boldsymbol{\varepsilon}_*$ and $\boldsymbol{\sigma}_*$ but with the objective function $\tilde{\Theta}_w$ (Bozda\u{g} *et al.*, 2011; Liu & Zhang, 2017),

$$\begin{aligned} \{\boldsymbol{\varepsilon}_*, \boldsymbol{\sigma}_*\} &= \arg \min \tilde{\Theta}_w(\boldsymbol{\varepsilon}, \boldsymbol{\sigma}; \mathbf{d}_w^o, \mathbf{d}_{w,a}^o), \\ \tilde{\Theta}_w &= \Theta_w(\boldsymbol{\varepsilon}, \boldsymbol{\sigma}; \mathbf{d}_w^o) + \Theta_{w,a}(\boldsymbol{\varepsilon}, \boldsymbol{\sigma}; \mathbf{d}_{w,a}^o), \end{aligned} \quad (4.19)$$

where $\mathbf{d}_{w,a}^o$ is the envelope of the observed data using the Hilbert transform and,

$$\begin{aligned} \Theta_{w,a} &= \frac{1}{n_s} \sum_s \Theta_{w,a}^s, \\ \Theta_{w,a}^s &= \frac{\|\mathbf{e}_{w,a}\|_2^2}{\|\mathbf{d}_{w,a}^{o,s}\|_2^2}, \end{aligned} \quad (4.20)$$

where s indexes the sources. The subscript a denotes the instantaneous amplitude (i.e. envelope), and the tilde denotes the sum of waveform and envelope sensitivity. We optimize $\tilde{\Theta}_w$ using gradient descent and regulate how much information $\Theta_{w,a}$ contributes to the inversion by weighing the gradients of Θ_w and $\Theta_{w,a}$ differently. The gradients of $\Theta_{w,a}$ with respect to the parameters $\boldsymbol{\varepsilon}$ and $\boldsymbol{\sigma}$ are computed using

a full-waveform approach where a different adjoint source has to be used for $\Theta_{w,a}$ as explained in Bozdağ *et al.* (2011) and reproduced in Appendix C for completeness.

For the sake of clarity we illustrate the optimization procedure for just $\boldsymbol{\varepsilon}$. For one source, let $\tilde{\mathbf{g}}_\varepsilon$, \mathbf{g}_ε and $\mathbf{g}_{\varepsilon,a}$ be the gradients of $\tilde{\Theta}_w^s$, Θ_w^s and $\Theta_{w,a}^s$, where the last two are computed as in equations 3.8 and C.10 respectively. We have,

$$\tilde{\mathbf{g}}_\varepsilon = \mathbf{g}_\varepsilon + \beta_\varepsilon \mathbf{g}_{\varepsilon,a}, \quad (4.21)$$

where the gradients \mathbf{g}_ε and $\mathbf{g}_{\varepsilon,a}$ are assumed normalized in amplitude and β_ε is a fixed scalar quantity for all sources and all iterations. The weight β_ε regulates how much we boost the low frequency content of the observed GPR data. Our numerical results show that a larger value of β_ε gives better depth resolution with the caveat of loosing spatial resolution. However if the value of β_ε is too large the inversion might strongly favor the low spatial-frequency content over the high spatial-frequency content, thus not giving accurate results.

Once $\tilde{\mathbf{g}}_\varepsilon$ has been computed we find the step-size α_ε as detailed in Chapter 3. After $\tilde{\mathbf{g}}_\varepsilon$ and α_ε have been computed for all sources the permittivity update is,

$$\Delta\boldsymbol{\varepsilon} = -\frac{1}{n_w} \sum_{s=1}^{n_w} \alpha_\varepsilon \tilde{\mathbf{g}}_\varepsilon. \quad (4.22)$$

Analogous to $\boldsymbol{\varepsilon}$, the update for $\boldsymbol{\sigma}$ is,

$$\tilde{\mathbf{g}}_\sigma = \mathbf{g}_{w,\sigma} + \beta_\sigma \mathbf{g}_{\sigma,a}, \quad (4.23)$$

$$\Delta\boldsymbol{\sigma}_w = -\frac{1}{n_w} \sum_{s=1}^{n_w} \alpha_\sigma \tilde{\mathbf{g}}_\sigma, \quad (4.24)$$

where β_σ is a fixed scalar quantity, $\mathbf{g}_{w,\sigma}$ and $\mathbf{g}_{\sigma,a}$ are computed as in equations 3.7 and C.9 respectively, and $\tilde{\mathbf{g}}_\sigma$ is assumed normalized in amplitude. Similarly to β_ε a larger value of β_σ will result in better depth resolution.

The weights β_ε and β_σ play an important role in recovering the subsurface parameters. In our numerical results we have found that when the GPR data has a small signal-to-noise ratio it is beneficial to use values close to one and when the signal-to-noise ratio is large, values smaller than one give better results. However, regardless on how good the signal-to-noise ratio is in the GPR data using the ER data in a joint inversion proves to have better results with comparatively stronger results when the GPR data exhibits strong attenuation.

We define our joint inversion of GPR envelope and ER data by minimizing the following objective function,

$$\{\boldsymbol{\varepsilon}_*, \boldsymbol{\sigma}_*\} = \arg \min \tilde{\Theta}_w(\boldsymbol{\varepsilon}, \boldsymbol{\sigma}; \mathbf{d}_w^o, \mathbf{d}_{w,a}^o) + \Theta_{dc}(\boldsymbol{\sigma}; \mathbf{d}_{dc}^o). \quad (4.25)$$

At a given iteration of our joint inversion (whose work-flow is as in Figure 4.1) we replace $\Delta\boldsymbol{\varepsilon}$ and $\Delta\boldsymbol{\sigma}_w$ by those computed in equations 4.22 and 4.24. The updated values for $\boldsymbol{\sigma}$ and $\boldsymbol{\varepsilon}$ are made as in equations 4.17 and 4.18.

We will refer to this inversion method (i.e. optimizing equation 4.25) as Joint and envelope inversion (JEN).

4.3.3 Joint inversion with cross-gradients

In this section we assume electrical permittivity and conductivity share structural properties. At a given iteration we want the structure of $\boldsymbol{\varepsilon}$ to be shared onto $\boldsymbol{\sigma}$ and vice-versa, and we want to do so by respecting the different concavities $\boldsymbol{\varepsilon}$ and $\boldsymbol{\sigma}$ may

have. For this reason we choose the discrete cross-gradient operator τ as a measure of structure (Gallardo & Meju, 2003),

$$\tau(\boldsymbol{\varepsilon}, \boldsymbol{\sigma}) = \nabla_{\mathbf{x}} \boldsymbol{\varepsilon} \times \nabla_{\mathbf{x}} \boldsymbol{\sigma}, \quad (4.26)$$

where $\nabla_{\mathbf{x}}$ denotes the discretized finite-difference spatial operator (∂_x, ∂_z) , and minimize the objective function Θ_τ ,

$$\Theta_\tau(\boldsymbol{\varepsilon}, \boldsymbol{\sigma}) = \frac{1}{2} \|\tau\|_2^2. \quad (4.27)$$

Because we are modeling the full physics of both the GPR and ER experiments and we compute the gradients of our objective functions using an FWI and adjoint method approach, our method differs from the original method of Gallardo & Meju (2003) because we do not compute the sensitivity matrices of our data. The result is that at each iteration of our joint inversion (whose work-flow is shown in Figure 4.3) we optimize equation 4.27 using a Gauss-Newton approach from which we only use the *master* updates $\Delta\boldsymbol{\sigma}_{\tau,o}$ and $\Delta\boldsymbol{\varepsilon}_{\tau,o}$. These updates are the cumulative sum of all updates done in the Gauss-Newton optimization routine. The details of optimizing equation 4.27 and computing $\Delta\boldsymbol{\sigma}_{\tau,o}$ and $\Delta\boldsymbol{\varepsilon}_{\tau,o}$ are explained in Appendix D.

We observe that minimizing Θ_τ in this way 1) has good potential for a well posed problem because the number of data points is equal to the number of unknowns (all the points in our model domain), 2) is relatively cheap in computation time and memory, 3) can be done by modifying both $\boldsymbol{\varepsilon}$ and $\boldsymbol{\sigma}$ or by keeping one fixed and only modifying the other, and 4) enables us to port the information of minimizing Θ_τ into our scheme for optimizing Θ_w and Θ_{dc} without having to use second order

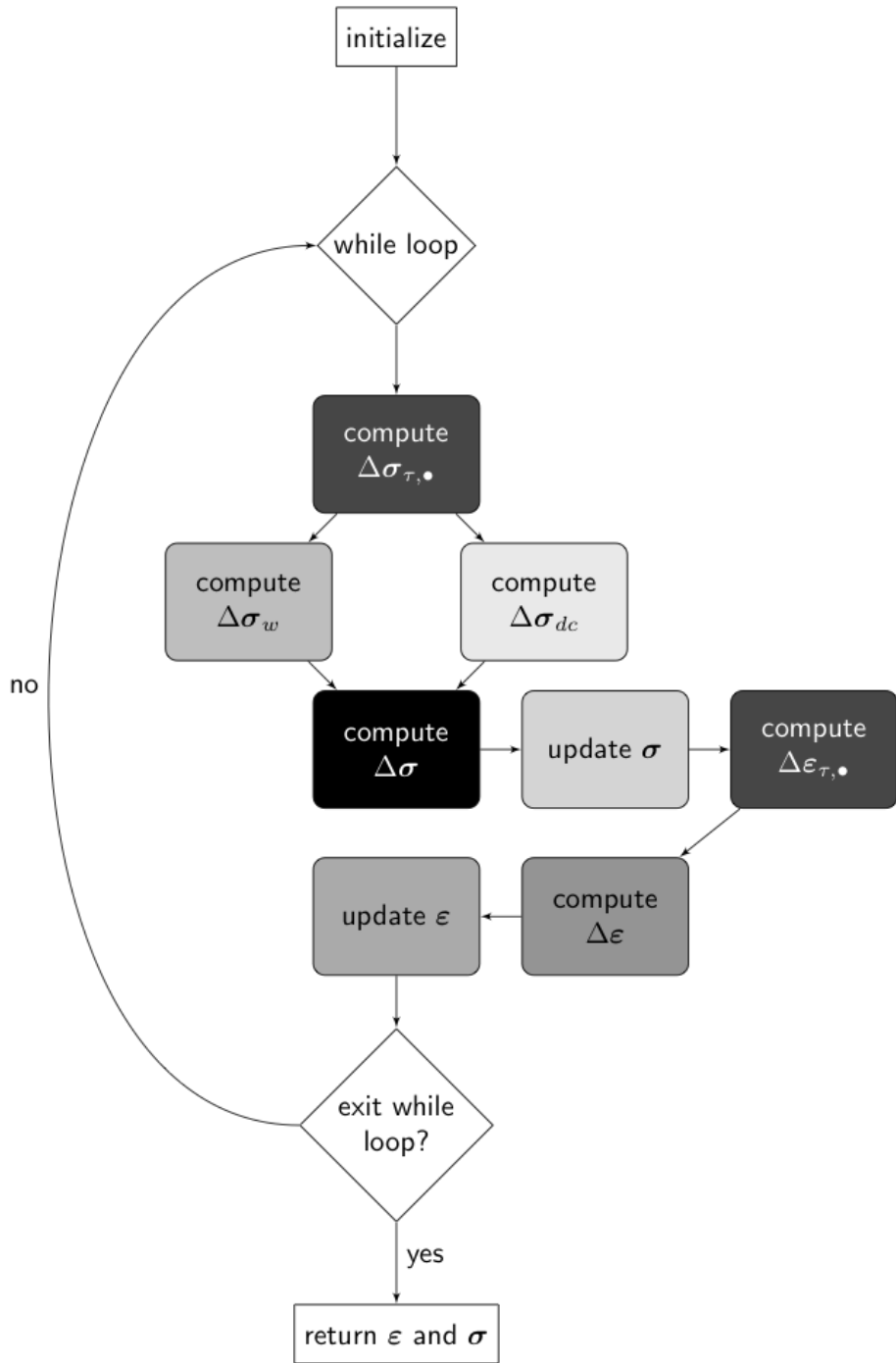


Figure 4.3: Inversion algorithm for JOIX and JENX. We differentiate JOIX and JENX by how we compute $\Delta\sigma_w$ and $\Delta\epsilon$.

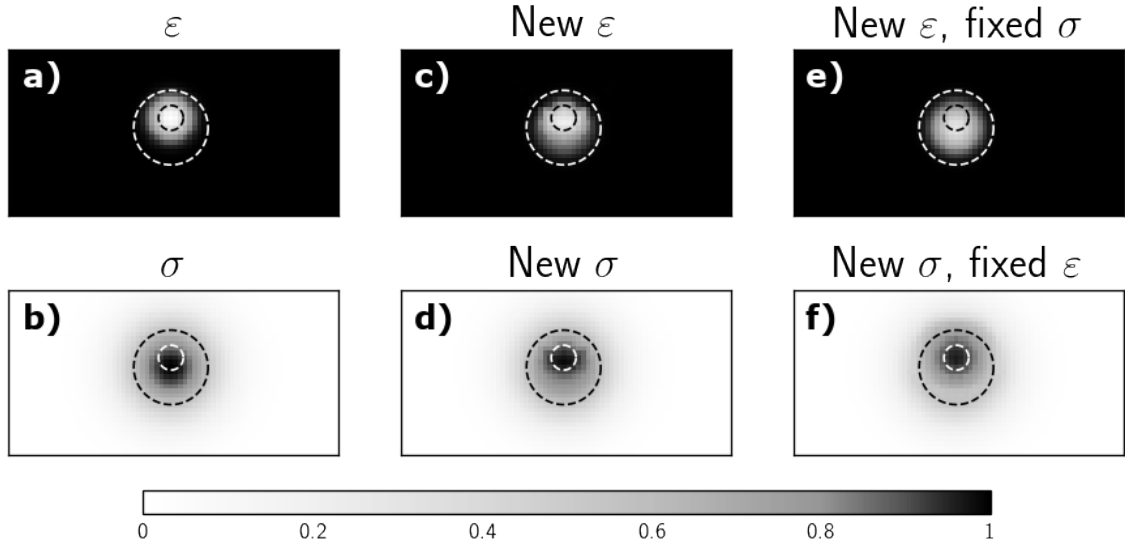


Figure 4.4: Illustration of cross-gradient possibilities. Given estimates ϵ and σ in a and b, Θ_τ is minimized by updating both ϵ and σ in c and d, updating ϵ and keeping σ fixed in e), and updating σ keeping ϵ fixed in f. The dashed circles are constant markers for the widths and centers of the Gaussian shapes in the given estimates of ϵ and σ .

optimization methods, i.e. the Hessians of Θ_w and Θ_{dc} .

Figure 4.4 gives an example of the different possibilities for minimizing Θ_τ outlined in observation 3). Given hypothetical values for ϵ and σ in Figure 4.4-a and 4.4-b, at a given iteration we minimize Θ_τ in three different ways. In Figures 4.4-c and 4.4-d we update ϵ and σ , in Figure 4.4-e) we fix σ and update ϵ , and in Figure 4.4-f we fix ϵ and update σ . Note that in this example both ϵ and σ have different concavities and different shapes, i.e. σ is wider than ϵ , mimicking the different resolutions our joint inversion is able to obtain from these two different parameters. The dashed circles are of fixed radii in all panels and serve as markers for the underlying shapes.

When optimizing Θ_τ for both σ and ϵ as shown in Figure 4.4-c and 4.4-d both σ and ϵ are modified and re-shaped to look more like one another since they are jointly

updated. Figure 4.4-e) shows $\boldsymbol{\varepsilon}$ expanding towards the outer circle, appearing even more similar to $\boldsymbol{\sigma}$ in Figure 4.4-b than that of Figure 4.4-c. Figure 4.4-f shows $\boldsymbol{\sigma}$ contracting into the inner circle, appearing even more similar to $\boldsymbol{\varepsilon}$ in Figure 4.4-a than that of Figure 4.4-d.

Depending on the subsurface material properties, the sensitivities of the GPR and ER data might resolve better at earlier iterations either $\boldsymbol{\varepsilon}$ or $\boldsymbol{\sigma}$. Whichever subsurface parameter is best resolved first should inform the other about its structural properties. Because of this reason and observations 1-4 above we choose to optimize Θ_τ twice per iteration: once modifying $\boldsymbol{\sigma}$ and keeping $\boldsymbol{\varepsilon}$ fixed and a second time modifying $\boldsymbol{\varepsilon}$ and keeping $\boldsymbol{\sigma}$ fixed. Each optimization has unique weights b_σ and b_ε that identify how much confidence we give to the current solutions of either $\boldsymbol{\varepsilon}$ or $\boldsymbol{\sigma}$.

We define our joint GPR and ER with cross-gradient by minimizing the following objective function,

$$\{\boldsymbol{\varepsilon}_*, \boldsymbol{\sigma}_*\} = \arg \min \Theta_w(\boldsymbol{\varepsilon}, \boldsymbol{\sigma}; \mathbf{d}_w^o) + \Theta_{dc}(\boldsymbol{\sigma}; \mathbf{d}_{dc}^o) + \Theta_\tau(\boldsymbol{\varepsilon}, \boldsymbol{\sigma}). \quad (4.28)$$

At each iteration of our joint inversion we begin with estimates of $\boldsymbol{\varepsilon}$ and $\boldsymbol{\sigma}$. The joint update for the conductivity first involves keeping $\boldsymbol{\varepsilon}$ fixed and computing the update $\Delta\boldsymbol{\sigma}_{\tau,o}$ given by equation D.7 that optimizes Θ_τ . Then we compute the weight b_σ and scale $\Delta\boldsymbol{\sigma}_{\tau,o}$,

$$b_\sigma = \left(h_\sigma \frac{a_{dc}}{a_w} - (h_\sigma - d_\sigma) a_{dc} \bullet \right) a_w, \quad (4.29)$$

$$\Delta\boldsymbol{\sigma}_{\tau,o} \leftarrow b_\sigma \Delta\boldsymbol{\sigma}_{\tau,o},$$

where $a_{dc} \bullet$ is the value of a_{dc} in the first iteration, $\Delta\boldsymbol{\sigma}_{\tau,o}$ is assumed normalized in amplitude. The scalars d_σ and h_σ control how early and how much in the joint

inversion should the structural information of $\boldsymbol{\varepsilon}$ is to be imprinted in $\boldsymbol{\sigma}$.

Figure 4.2 depicts the optimal path of b_σ throughout the iterations. During early iterations b_σ is small because not enough structure has been recovered on $\boldsymbol{\varepsilon}$, but at late iterations b_σ is larger because $\boldsymbol{\varepsilon}$ is closer to its true solution. The value of b_σ at a given iteration is a measure of how much confidence we have on the structure of the current solution for $\boldsymbol{\varepsilon}$: the larger b_σ the more confidence we have on $\boldsymbol{\varepsilon}$.

We note that the upward trend of b_σ over iterations can only be achieved if

$$h_\sigma \geq d_\sigma > 0, \quad (4.30)$$

which also forces b_σ to plateau to the value h_σ in late iterations so as to inhibit dominance of the structural assumption and let the physics of our inversions assume control. The purpose of d_σ is to control the value of b_σ for the first iteration: $b_\sigma = d_\sigma a_{dc} \bullet$.

The new update $\Delta\boldsymbol{\sigma}_{\tau,o}$ is now passed to the GPR and ER optimization routines before the step-sizes of the gradients are computed,

$$\begin{aligned} \mathbf{g}_{w,\sigma} &\leftarrow \mathbf{g}_{w,\sigma} + \Delta\boldsymbol{\sigma}_{\tau,o}, \\ \mathbf{g}_{dc} &\leftarrow \mathbf{g}_{dc} + \Delta\boldsymbol{\sigma}_{\tau,o}, \end{aligned} \quad (4.31)$$

where both $\mathbf{g}_{w,\sigma}$ and \mathbf{g}_{dc} are assumed normalized in amplitude. The step-sizes of the gradients $\mathbf{g}_{w,\sigma}$ and \mathbf{g}_{dc} are computed as described in Chapter 3 and the updates $\Delta\boldsymbol{\sigma}_w$ and $\Delta\boldsymbol{\sigma}_{dc}$ are computed as in equations 4.12 and 4.13. Finally, the updated value for $\boldsymbol{\sigma}$ is calculated as in equation 4.17.

Figure 4.3 shows a code-flow diagram of our joint inversion with the cross-gradient.

The next step in our joint inversion is the structural update to $\boldsymbol{\varepsilon}$ which is analogous to the update we just computed for $\boldsymbol{\sigma}$. We keep $\boldsymbol{\sigma}$ fixed, compute $\Delta\boldsymbol{\varepsilon}_{\tau,o}$ given by equation D.6, compute the weight b_ε and scale $\Delta\boldsymbol{\varepsilon}_{\tau,o}$,

$$b_\varepsilon = \left(h_\varepsilon \frac{a_{dc}}{a_w} - (h_\varepsilon - d_\varepsilon) a_{dc\bullet} \right) a_w, \quad (4.32)$$

$$\Delta\boldsymbol{\varepsilon}_{\tau,o} \leftarrow b_\varepsilon \Delta\boldsymbol{\varepsilon}_{\tau,o},$$

where $\Delta\boldsymbol{\varepsilon}_{\tau,o}$ is normalized in amplitude. The new update $\Delta\boldsymbol{\varepsilon}_{\tau,o}$ is now passed to the GPR optimization routine before the step-size of the gradient is computed by

$$\mathbf{g}_\varepsilon \leftarrow \mathbf{g}_\varepsilon + \Delta\boldsymbol{\varepsilon}_{\tau,o}, \quad (4.33)$$

where \mathbf{g}_ε is assumed normalized in amplitude. The updated value for $\boldsymbol{\varepsilon}$ is calculated by equation 4.18 where the update $\Delta\boldsymbol{\varepsilon}$ is given in equation 4.14.

The weights h_ε and d_ε are not necessarily equal to h_σ and d_σ , but b_ε must follow a similar shape as b_σ (see Figure 4.2). Similar to b_σ , the value of b_ε at a given iteration is a measure of how much confidence we have on the structure of the current solution for $\boldsymbol{\sigma}$: the larger b_ε the more confidence we have on $\boldsymbol{\sigma}$.

Because h_σ and h_ε regulate how large b_σ and b_ε can become over the course of iterations, we propose two general rules on choosing h_σ and h_ε based on how much conductivity is present in the subsurface:

1. if conductivity is low h_ε should be small and h_σ large,
2. if conductivity is high h_σ should be small and h_ε large.

We recognize that in a real scenario we might not know a-priori the conductivity of

the subsurface, however we can obtain a good enough approximation for determining h_σ and h_ε by observing the ER pseudo-sections and assessing how many reflection events are visible in the GPR shot-gathers.

We will refer to this inversion method (i.e. optimizing equation 4.28) as Joint and cross-gradients inversion (JOIX).

4.3.4 Joint inversion of GPR envelope and ER data with cross-gradient

Now that we have enhanced our joint inversion of GPR and ER data (Domenzain *et al.*, 2019a) with an envelope objective function for the GPR data and with structural similarities of subsurface electrical properties, we develop a third method that joins these two enhancements into one single inversion procedure. The joint GPR envelope and ER data with cross-gradient inversion minimizes the following objective function,

$$\{\boldsymbol{\varepsilon}_*, \boldsymbol{\sigma}_*\} = \arg \min \tilde{\Theta}_w(\boldsymbol{\varepsilon}, \boldsymbol{\sigma}; \mathbf{d}_w^o, \mathbf{d}_{w,a}^o) + \Theta_{dc}(\boldsymbol{\sigma}; \mathbf{d}_{dc}^o) + \Theta_\tau(\boldsymbol{\varepsilon}, \boldsymbol{\sigma}). \quad (4.34)$$

At a given iteration we first compute $\Delta\boldsymbol{\sigma}_{\tau,o}$ as in equation 4.29, and then add this information to the gradients $\mathbf{g}_{w,\sigma}$ and \mathbf{g}_{dc} normalized in amplitude given by equations 3.7 and 3.20,

$$\begin{aligned} \mathbf{g}_{w,\sigma} &\leftarrow \mathbf{g}_{w,\sigma} + \beta_\sigma \mathbf{g}_{\sigma,a} + \Delta\boldsymbol{\sigma}_{\tau,o}, \\ \mathbf{g}_{dc} &\leftarrow \mathbf{g}_{dc} + \Delta\boldsymbol{\sigma}_{\tau,o}. \end{aligned} \quad (4.35)$$

Once the gradients from all sources have been computed, we find the updates $\Delta\boldsymbol{\sigma}_w$ and $\Delta\boldsymbol{\sigma}_{dc}$ as given by equations 4.12 and 4.13. Then we can compute $\Delta\boldsymbol{\sigma}$ with equation 4.16 and update $\boldsymbol{\sigma}$ as in equation 4.17.

In order to compute $\Delta\boldsymbol{\epsilon}$ we first compute $\Delta\boldsymbol{\epsilon}_{\tau,o}$ as in equation 4.32 and then add this information to \mathbf{g}_ϵ and $\mathbf{g}_{\epsilon,a}$ normalized in amplitude as given by equations 3.8 and C.10,

$$\mathbf{g}_\epsilon \leftarrow \mathbf{g}_\epsilon + \beta_\epsilon \mathbf{g}_{\epsilon,a} + \Delta\boldsymbol{\epsilon}_{\tau,o}. \quad (4.36)$$

Once all gradients for all sources have been computed we find $\Delta\boldsymbol{\epsilon}$ as given by equation 4.14. Finally we update $\boldsymbol{\epsilon}$ as in equation 4.18. The code-flow diagram in Figure 4.3 also describes this procedure with gradients computed by equations 4.35 and 4.36.

We refer to this inversion method (i.e. optimizing equation 4.34) as Joint, envelope and cross-gradients inversion (JENX).

Choice of weights

In order to join the objective functions $\tilde{\Theta}_w$, Θ_{dc} and Θ_τ we have introduced 11 weights. Our joint inversion requires 5 (equation 4.15), the envelope inversion requires 2 (equations 4.21 and 4.23) and the cross-gradient inversion requires 4 (equations 4.29 and 4.32). Aside from the considerations given for each inversion routine, our numerical results show that when all weights are non-zero they all influence each other. In some cases the influence the weights exert on each other can lead to a different behavior in the inversion than what was explained in the previous sections.

We observe that the conductivity solution influences the permittivity solution in a stronger way than the permittivity solution influences the conductivity solution. Moreover, because of the weak sensitivity the GPR data has on the conductivity, obtaining a good solution for the conductivity is most efficiently achieved by joining the ER data (Domenzain *et al.*, 2019a). Therefore, we assume we are already satisfied with the joint weights of equation 4.15 and focus on improving the permittivity and

conductivity solution with weights for $\tilde{\Theta}_w$ or Θ_τ .

Let us first assume the conductivity of the subsurface is low and the GPR data holds enough information for a good solution of the permittivity. If we increase β_σ or h_σ (in equations 4.35 and 4.29) to improve depth or spatial resolution in σ we pay the price of degrading the spatial and amplitude resolution of ϵ .

Let us now assume the conductivity in the subsurface is high and the GPR data does not hold enough information for a good estimate of the permittivity but the ER data is enough for a good solution of the conductivity. Contrary to the above scenario, in this case it is possible to exploit the good solution of σ and the low frequency content of the GPR data in order to improve ϵ . Our approach consists of over-weighing the envelope of the GPR data and relying on the cross-gradients to regulate the excess of the low-frequency content. We choose negative weights b_ϵ and b_σ for the cross-gradient updates in order to trim off the low-frequency over-fit. The use of negative weights on Θ_τ to counteract an overfit due to $\tilde{\Theta}_w$ is a novel approach to effectively using both of cross-gradients and the envelope transform as it takes into account the sensitivities of both objective functions at each iteration. The descent direction for the ϵ solution is ensured by computing the step-size for the updates with a parabolic line search as explained in Chapter 3.

We recognize that all 11 weights were found by trial and error. In the low-conductivity scenario we followed the qualitative guidelines explained in the previous sections and shown in Figure 4.2. For the high-conductivity scenario the negative weights (h_ϵ , d_ϵ , h_σ and d_σ) were chosen in order for b_ϵ and b_σ to smoothly decrease magnitude in absolute value as iterations progressed. This choice results in more low-frequency content trim-off at early iterations and less at later iterations.

4.4 Subsurface simulations

Recovering electrical permittivity and conductivity of the subsurface using full-waveform inversion of surface acquired GPR data can be challenging if low frequencies are sparse and attenuation is high. Furthermore if the subsurface geometry has velocity and attenuation anomalies larger than a wavelength of the GPR signal the data might miss amplitude information to accurately recover said anomalies. Recovering electrical conductivity of the subsurface at depth using surface acquired ER data is limited by needing large offsets. Furthermore if the subsurface has electrical conductivity anomalies smaller than the receiver electrode distance, the ER data cannot spatially resolve said anomaly.

Joining GPR and ER data (whose different sensitivities compliment each other by sharing electrical conductivity) can better resolve subsurface electrical properties given that both GPR and ER data hold enough information about the subsurface. However if the subsurface is poorly conductive the ER data might have little sensitivity to changes in the conductivity when compared to the GPR data. Conversely, if the subsurface is highly conductive the ER data might have a larger sensitivity to changes in the conductivity when compared to the GPR data.

In view of these observations and in an effort to keep our analysis as simple as possible we choose to test our algorithms on two synthetically designed subsurface scenarios: one with low and one with high electrical conductivity as shown in Figures 3.8-a),b) and 3.8-a),c). Both scenarios have the same subsurface geometry: an electrical velocity and conductive box-anomaly in the center and a velocity reflector at depth. The box is $1 \times 1\text{m}$ wide: two wavelengths long but just within the limit of our chosen ER experiment spatial resolution.

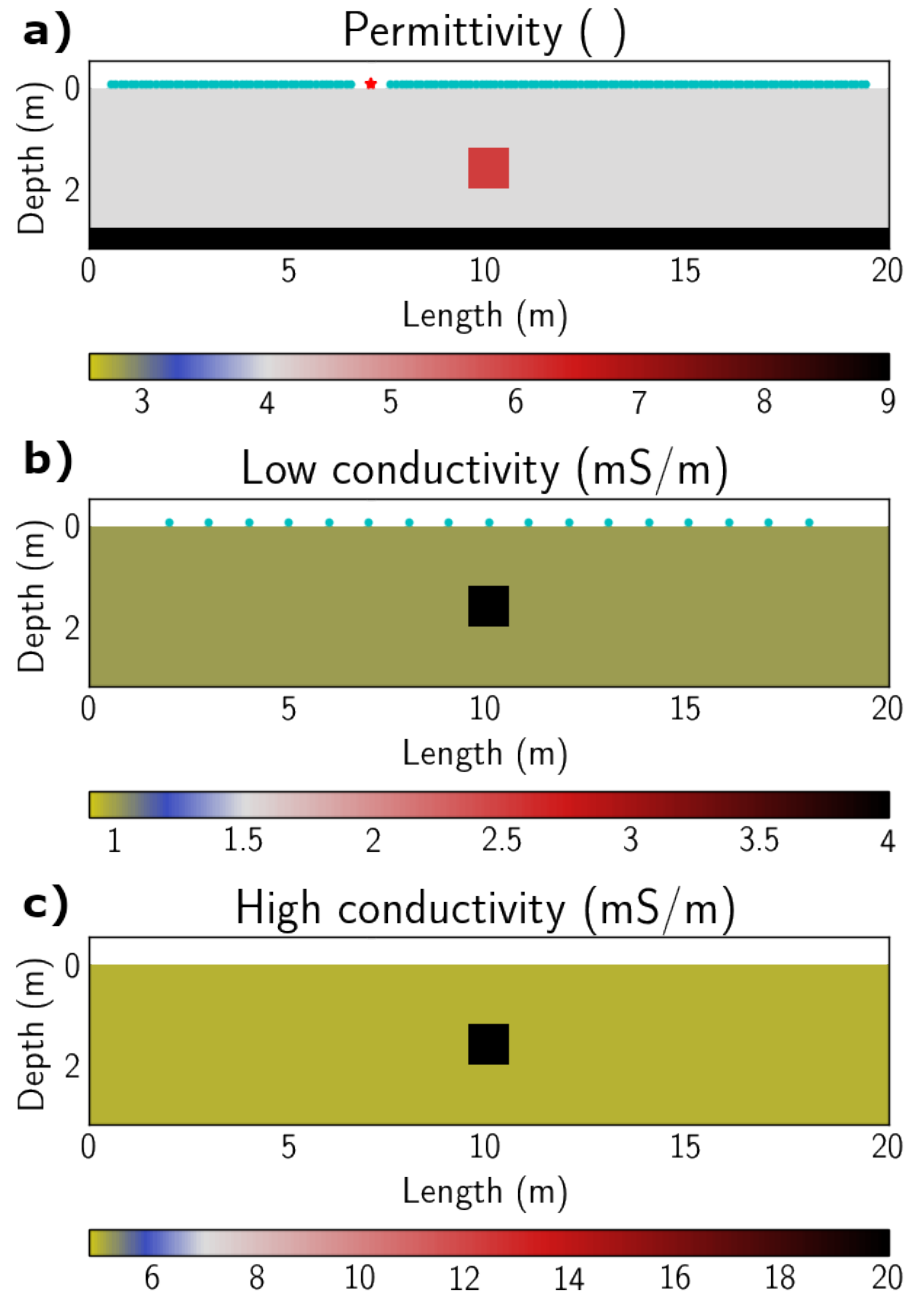


Figure 4.5: True permittivity a and conductivity for the low b and high c conductivity scenario. In a, GPR source and receivers layout for line # 7. In b, all electrodes used for our ER experiment.

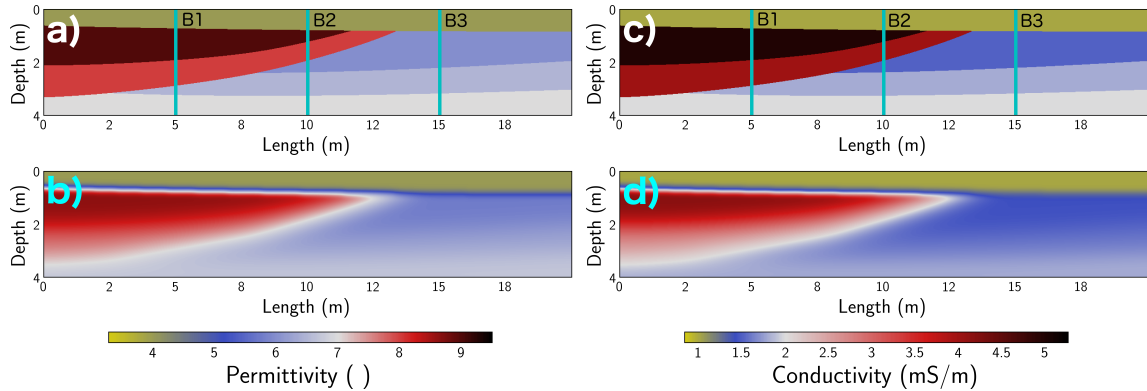


Figure 4.6: Synthetic alluvial aquifer true and initial parameters. True a and initial b permittivities. True c and initial d conductivities. The cyan lines represent boreholes B1, B2 and B3 from left to right.

Finally, we implement our algorithm with all objective functions in a scenario resembling an alluvial aquifer as shown in Figure 4.6-a and c. Our synthetic aquifer loosely follows the subsurface geometry of the Boise Hydrogeophysical Research Site (BHSR) as imaged by Bradford *et al.* (2009b) and mapped by Barrash & Clemo (2002). The electrical parameters resemble those of dry gravel on the shallow layer and a variety of moist sands in the deeper layers, with wetter sands (but not saturated) to the left of the model. The dipping shallow layer is at most two wavelengths deep and just within our ER spatial resolution. The wet region acts both as a strong reflector and as attenuative media for the radar data.

4.4.1 Experiments

Low & high conductivity

We model 250MHz GPR antennas with a Ricker wavelet source. We apply 20 equally spaced sources on the air-ground interface with source-receiver near-offset of 0.5m (approximately one wavelength) and receiver-receiver distance a quarter of a wave-

length as shown in Figure 3.8-**a**. For the ER experiment we use 17 electrodes placed 1m away from each other on the air-ground interface (see Figure 3.8-**b**) and perform all possible dipole-dipole and Wenner array configurations.

The synthetic GPR and ER data are then given random white noise with amplitude of 10% of their standard deviation as explained in Chapter 3. See Figures 4.7 and 4.8 for the acquired data in both scenarios. Note that for the high-conductivity scenario the signal in the GPR data is very weak, and near where the box reflection event should be the signal-to-noise ratio is almost 1, while for the low-conductivity scenario the GPR data shows strong reflections.

All inversions have a starting homogeneous model for both permittivity and conductivity: a value of 4 for permittivity, and values of 1mS/m and 5mS/m for the low and high-conductivity scenarios respectively.

Synthetic alluvial aquifer

We use the same acquisition geometry as for the low and high conductivity experiments (see Figure 3.8-**a** and Figure 3.8-**b**). Given the complicated subsurface geometry, we enhance the ER experiment with all possible Schlumberger arrays. All our data are given random white noise analogous to the low and high conductivity scenarios. To aid our analysis we place boreholes B1, B2 and B3 as shown in Figure 4.6-**a** and **c**.

Figure 4.6-**b** displays the initial permittivity and Figure 4.6-**d** the initial conductivity used in our inversions. Our numerical experiments suggest a very strong sensitivity to the first layer in our initial models throughout our inversions. We choose a smooth initial model that accurately resolves the first air-wave refraction in the GPR

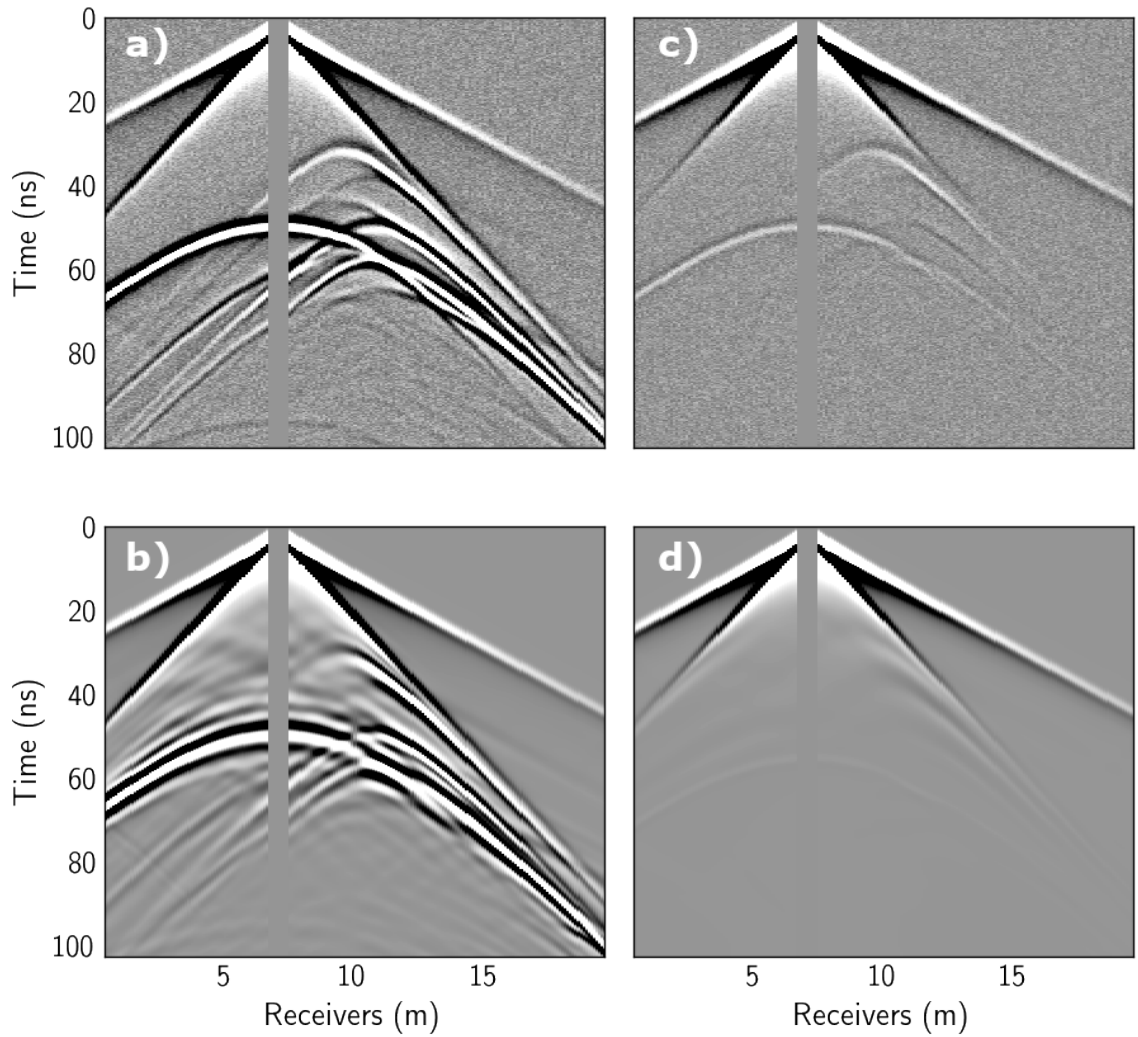


Figure 4.7: GPR shot gather # 7 of the low and high-conductivity scenarios and their respective best recovered parameters as given by Figures 4.10-4.11 d for the low-conductivity and 4.12-4.13 d for the high-conductivity scenario. Amplitudes are clipped to 1.5% of the maximum amplitude in the data.

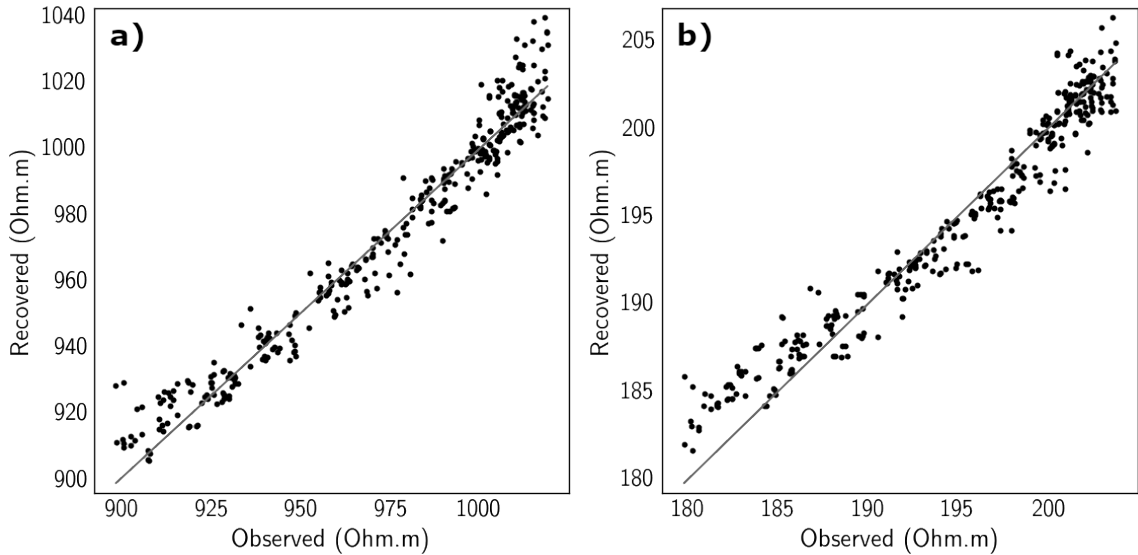


Figure 4.8: ER data of the low a and high b conductivity scenarios and their respective best recovered parameters.

data and qualitatively follows the shape of the low-velocity region in length. Figure 4.9-a gives the residual of the initial and observed GPR data: all reflection events below the first air-wave refraction are present.

In Appendix D we give the details for choosing and building our initial models. The strategy consists in perturbing the true model in two different ways. First, we smooth it enough to lose depth resolution of the first layer and lateral resolution of the low-velocity region. As a second approach, we smooth the true model below the first layer but retain the true model for the first layer. The smoothing is done with a Gaussian low-pass filter in the space frequency domain with a half-width of 0.8 1/m. The initial model in Figure 4.6-b and d is an intermediate step between the first and second perturbations. It is described in Appendix E. We note that although demanding, these initial models are representations of the long wavelength structure that could realistically be obtained from reflection tomography and careful analysis

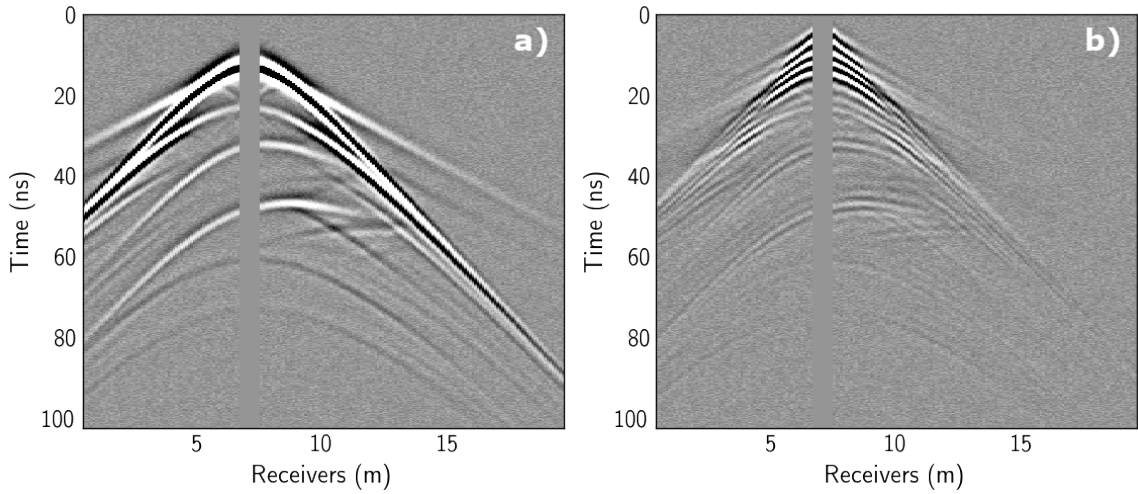


Figure 4.9: Residuals of GPR shot-gather #7 for the synthetic alluvial aquifer. Residual of initial model and observed in a, and of recovered and observed in b. Recovered data correspond to the JOIX method. Amplitudes are clipped to 1.5% of the maximum amplitude in the data.

of direct arrivals.

4.4.2 Results

Low conductivity

Figures 4.10-**a** and 4.11-**a** show the recovered parameters for the low-conductivity case using joint inversion of GPR and ER data and using the weights in the first column of Table 4.2. We see the shape and amplitude of the box recovered in the permittivity solution together with high spatial-frequency artifacts around the box mainly due to one-sided acquisition and noise in the data. The recovered conductivity also exhibits high spatial-frequency artifacts around the box and a strong amplitude from the permittivity bottom reflector due to the GPR data being unable to distinguish permittivity from conductivity reflections.

Figures 4.10-**b** and 4.11-**b** show the recovered parameters for the low-conductivity

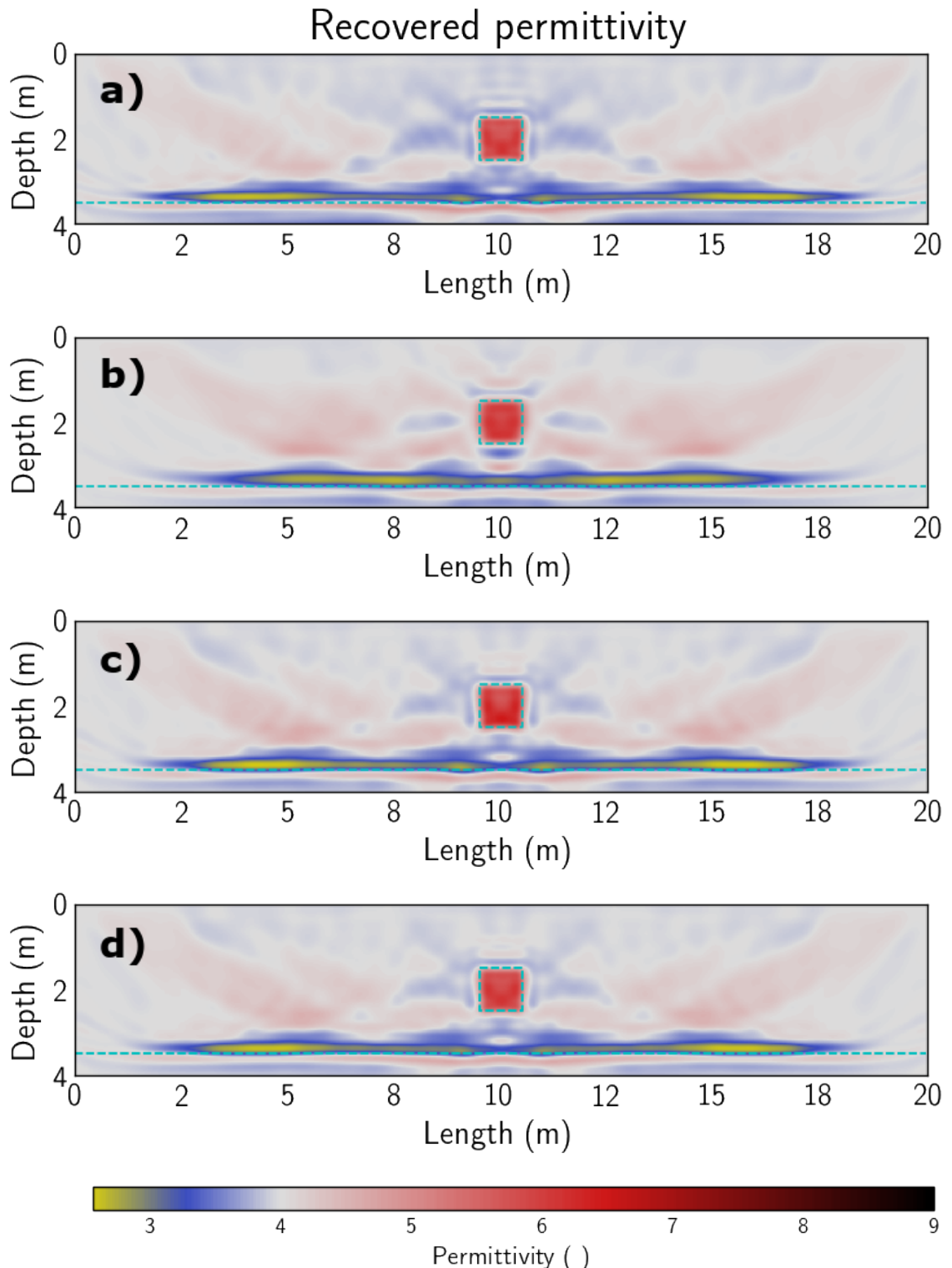


Figure 4.10: Recovered permittivity with low conductivity using Joint in a, JEN in b, JOIX in c and JENX in d.

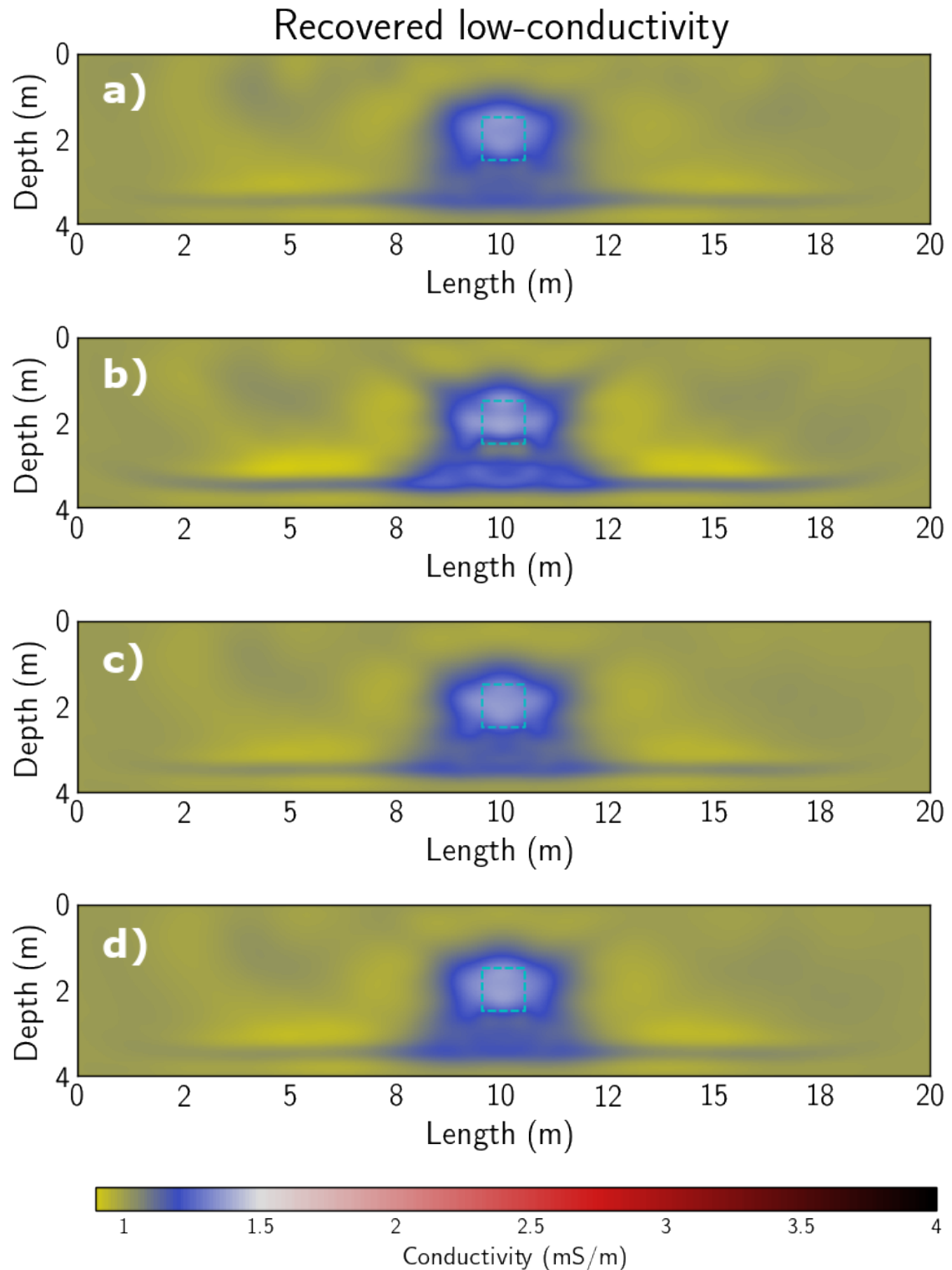


Figure 4.11: Recovered low conductivity using Joint in a, JEN in b, JOIX in c and JENX in d.

Table 4.2: Inversion parameters for the low-conductivity scenario.

Low σ	Joint	JEN	JOIX	JENX
$a_{dc} \bullet$	0.85	0.85	0.85	0.85
\dot{a}_{dc}	3	3	3	3
$\dot{\Theta}_{dc}$	2	2	2	2
\dot{a}_w	4	4	4	4
$\dot{\Theta}_w$	0.9	0.9	0.9	0.9
β_ε		0.25		
β_σ		0.25		1e-5
h_ε			0.01	
d_ε			0.1	
h_σ				1e-3
d_σ				

case using joint inversion of GPR envelope and ER data and using the weights in the second column of Table 4.2. In the recovered permittivity we note less high spatial-frequency artifacts than in the joint inversion case (see Figure 4.10-**a**), although the price to pay is a lower resolution of the box. The recovered conductivity shows better amplitude resolution although the bottom permittivity reflector is now thicker than in the joint inversion case (see Figure 4.11-**a**) due to the larger weighing of the GPR low frequency.

Figures 4.10-**c** and 4.11-**c** show the recovered parameters for the low-conductivity case using joint inversion of GPR and ER data with cross-gradients and using the weights in the third column of Table 4.2. We see the permittivity solution is very similar to the joint inversion result (Figure 4.10-**a**). However, the recovered conductivity has a more even spread in amplitude resolution compared to the joint and envelope inversion and the artifact amplitude of the permittivity reflector is now less as compared with Figures 4.11-**a** and **b**.

Figures 4.10-**d** and 4.11-**d** show the recovered parameters for the low-conductivity case using joint inversion of GPR envelope and ER data with cross-gradients and using the weights in the fourth column of Table 4.2. The permittivity solution is again very similar to the results of Figures 4.10-**a** and **c** but the conductivity solution is now slightly better than the rest of the inversion results by having a more localized resolution around the box.

High conductivity

Figures 4.12-**a** and 4.13-**a** show the recovered parameters for the high-conductivity case using joint inversion of GPR and ER data with weights as in the first column of Table 4.3. We note very weak amplitude and low spatial-frequency resolution on the recovered permittivity due to strong attenuation and a signal-to-noise ratio equal almost to 1 in the region of the box reflection event. The recovered conductivity exhibits better low spatial-frequency content than the low-conductivity case, however, there are stronger amplitudes near the top of the box than at depth.

Figures 4.12-**b** and 4.13-**b** show the recovered parameters for the high-conductivity case using joint inversion of GPR envelope and ER data with weights as in the second column of Table 4.3. The recovered permittivity now exhibits less high-spatial frequency content than in the joint inversion of GPR and ER case (see Figure 4.12-**a**) and a small increase in amplitude resolution near the box anomaly. For the recovered conductivity we note a slight increase in amplitude resolution at depth.

Figures 4.12-**c** and 4.13-**c** show the recovered parameters for the high-conductivity case using joint inversion of GPR and ER data with cross-gradients and weights as in the third column of Table 4.3. We see the improved amplitude resolution in the

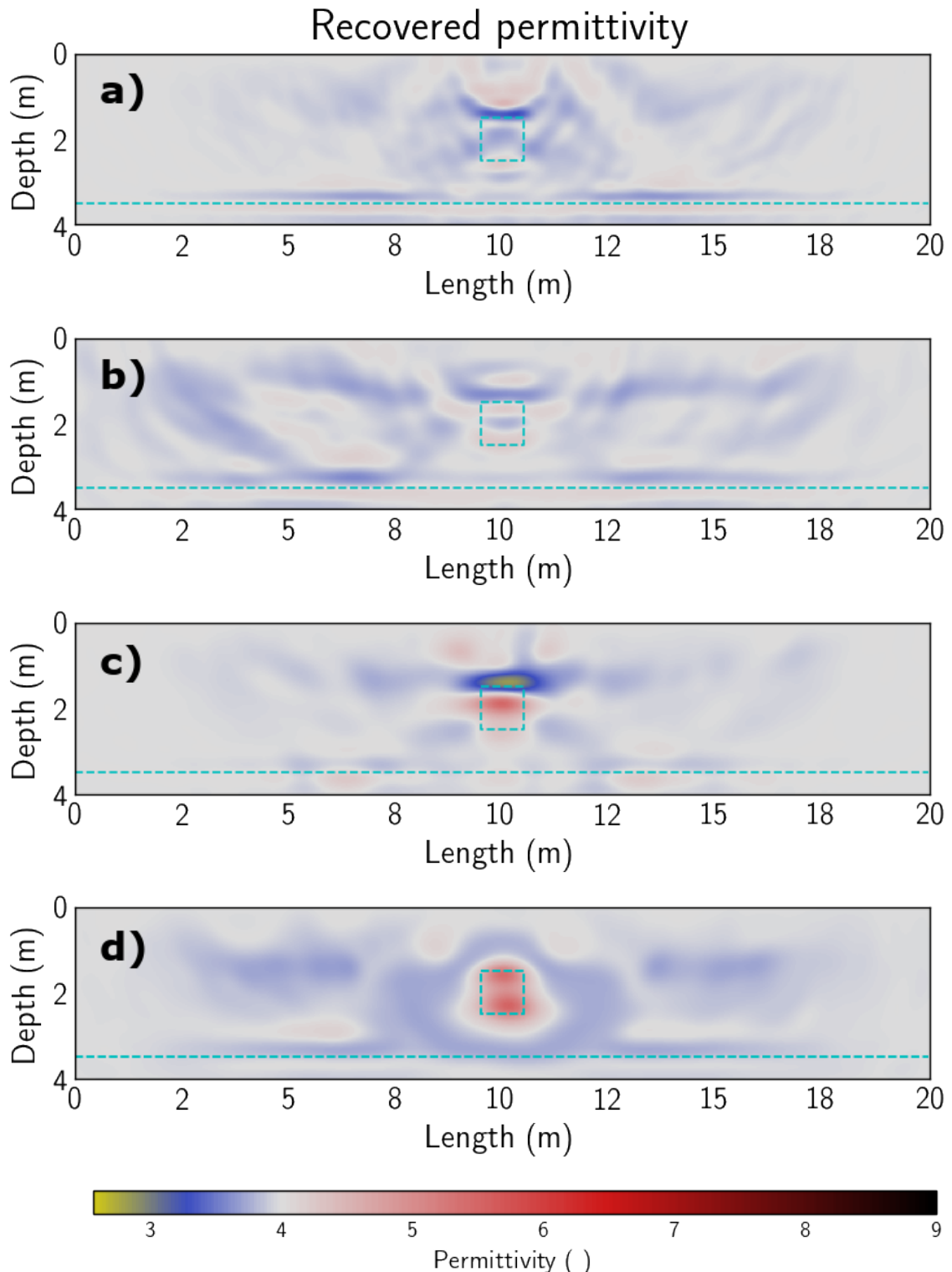


Figure 4.12: Recovered permittivity with high conductivity using Joint in a, JEN in b, JOIX in c and JENX in d.

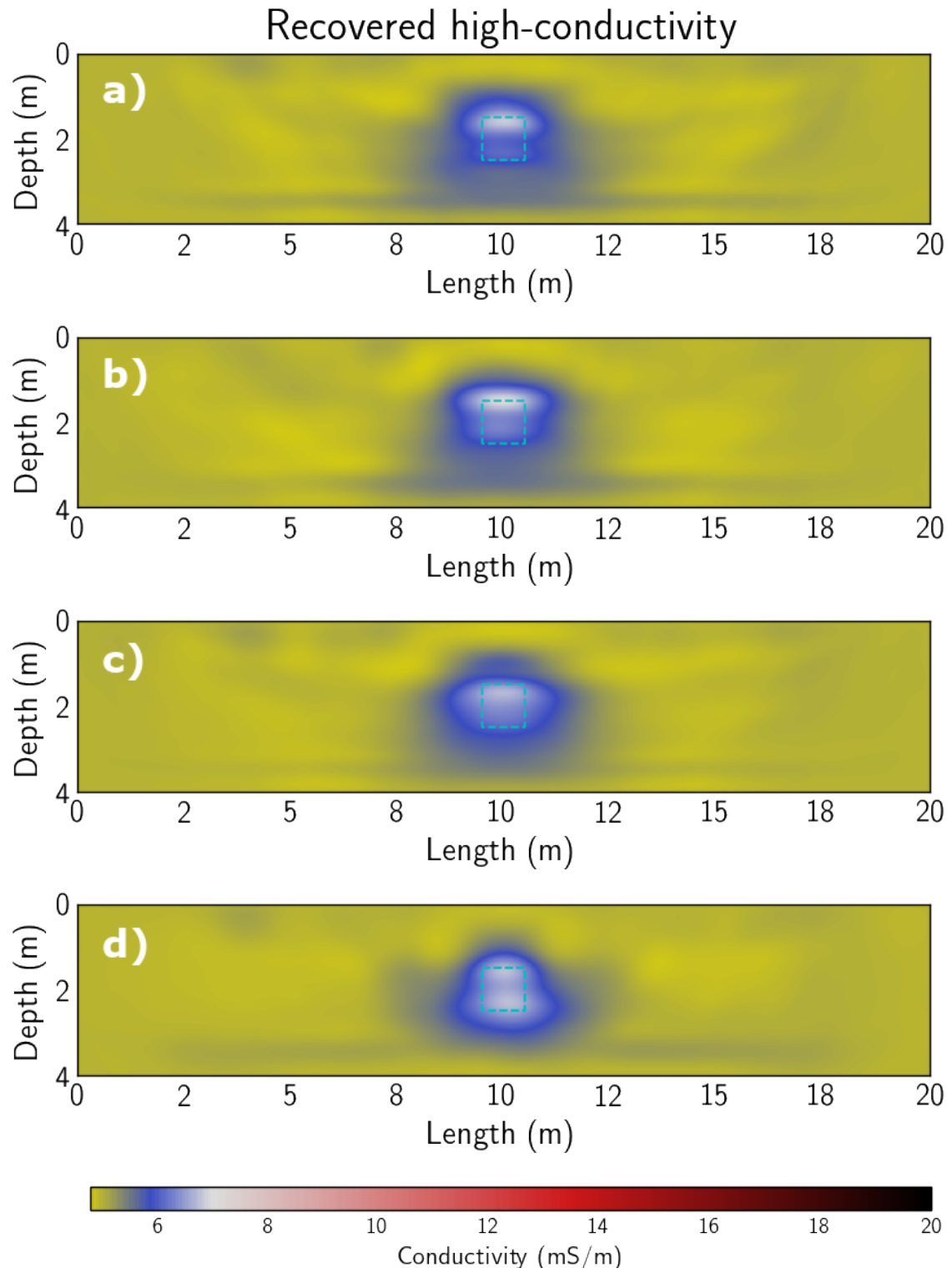


Figure 4.13: Recovered high conductivity using Joint in a, JEN in b, JOIX in c and JENX in d.

Table 4.3: Inversion parameters for the high-conductivity scenario.

High σ	Joint	JEN	JOIX	JENX
$a_{dc} \bullet$	0.85	0.85	0.85	0.87
\dot{a}_{dc}	1.5	1.5	1.5	1.5
$\dot{\Theta}_{dc}$	1.5	1.5	1.5	1.5
\dot{a}_w	2.5	2.5	2.5	2.5
$\dot{\Theta}_w$	0.9	0.9	0.9	0.9
β_ε		1		0.5
β_σ		1		0.5
h_ε			0.2	-0.3
d_ε			0.6	-3
h_σ				-0.16
d_σ				-0.6

region where the permittivity box lies, although the overall shape is missing low spatial-frequency information. The recovered conductivity now has a better depth amplitude resolution as compared with the joint GPR and ER and joint GPR envelope and ER inversions (see Figures 4.13-**a** and **b**).

Figures 4.12-**d** and 4.13-**d** show the recovered parameters for the high-conductivity case using joint inversion of GPR envelope and ER data with cross gradients and weights as in the fourth column of Table 4.3. The permittivity anomaly is now recovered with an accurate amplitude and overall correct shape, however we observe an overshoot of low spatial-frequency content as a remanent artifact from the conductivity solution and the smoothing factor in the gradients. The recovered conductivity however, is now more accurate at depth and a better overall spatial resolution than the rest of the inversions.

Table 4.4: Inversion parameters for the synthetic alluvial aquifer.

	$a_{dc} \bullet$	\dot{a}_{dc}	$\dot{\Theta}_{dc}$	\dot{a}_w	$\dot{\Theta}_w$	β_ε	β_σ	h_ε	d_ε	h_σ	d_σ	iterations
Joint	0.2	3	2	1.5	0.3							129
JEN	0.2	3	2	1.5	0.3	0.5	0.5					89
JOIX	0.2	3	2	1.5	0.3			-10^{-3}	-0.4	-10^{-4}	-0.1	400
JENX	0.2	3	2	1.5	0.3	0.5	0.5	-10^{-3}	-0.2	-10^{-4}	-0.1	155

Synthetic alluvial aquifer

In Lavoué *et al.* (2014) the authors invert GPR surface acquired data of a synthetic realistic subsurface scenario. The authors use a full-waveform approach and they note that regularization is needed for constraining the conductivity solution. In this work, we apply no additional regularization of the inversion beyond the joint objective function itself and the cross-gradients constraint.

Similar to our discussion for low and high conductivity, we performed all our inversions (Joint, JEN, JOIX, JENX) on the synthetic alluvial aquifer with inversion parameters as in Table 4.4. Figure 4.14 shows the recovered permittivity and Figure 4.15 shows the recovered conductivity for all inversions.

In Figure 4.14 for all inversions we see artifact ripples in the first layer. These ripples are due to the small discrepancy between values of the true and initial model (approximately 2.5% in the first layer). Similar lower space-frequency artifacts are also present in the recovered conductivity (see Figure 4.15).

Throughout Figure 4.14 we see the effect of having such a high impedance contrast between the first layer and the low-velocity region: one-sided acquisition struggles to resolve the immediate section of the region below the first layer. As seen in Appendix E, this effect can be drastically reduced in the entire domain if the first layer of our

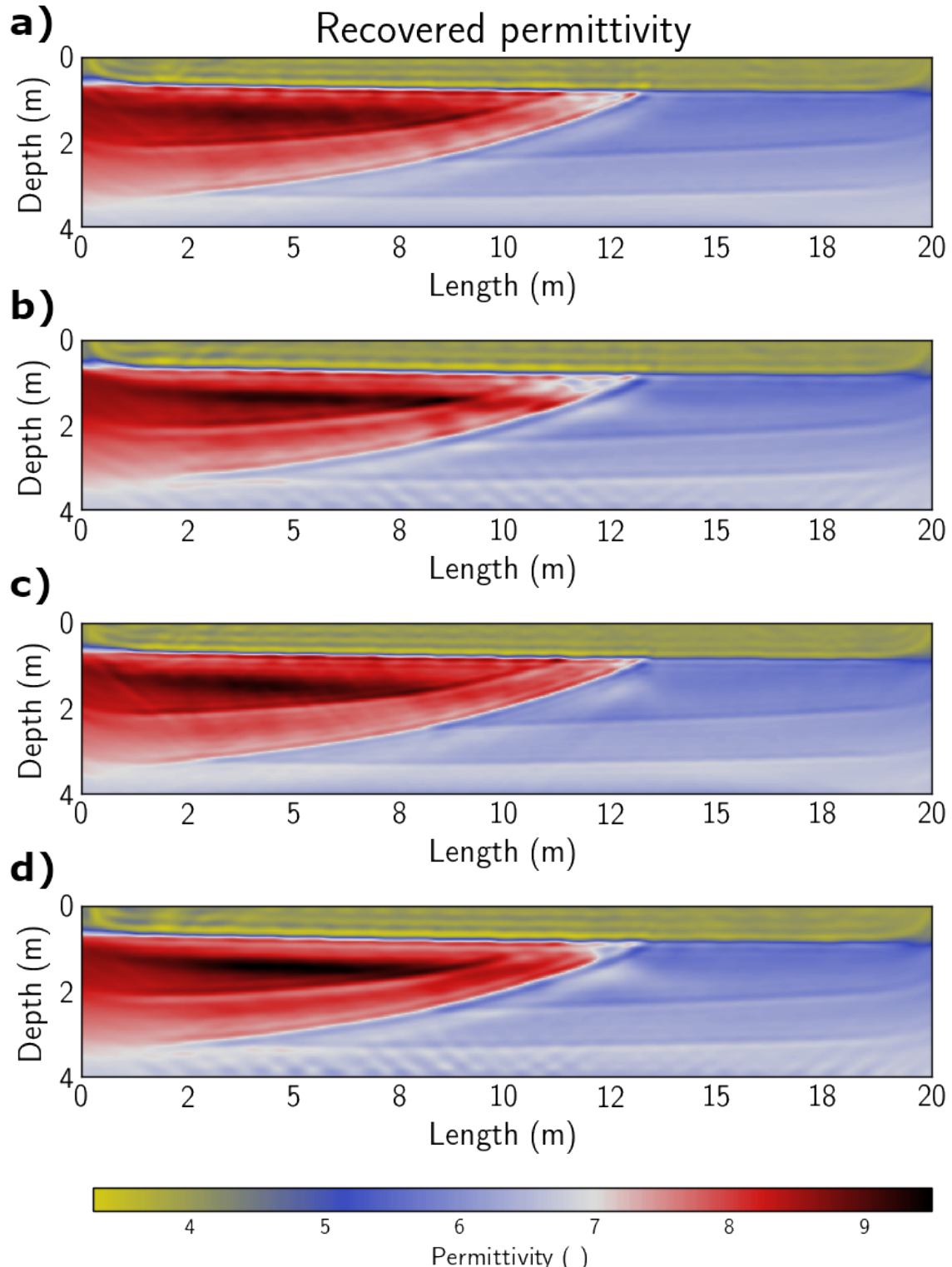


Figure 4.14: Recovered permittivity for the synthetic alluvial aquifer using Joint in a, JEN in b, JOIX in c and JENX in d.

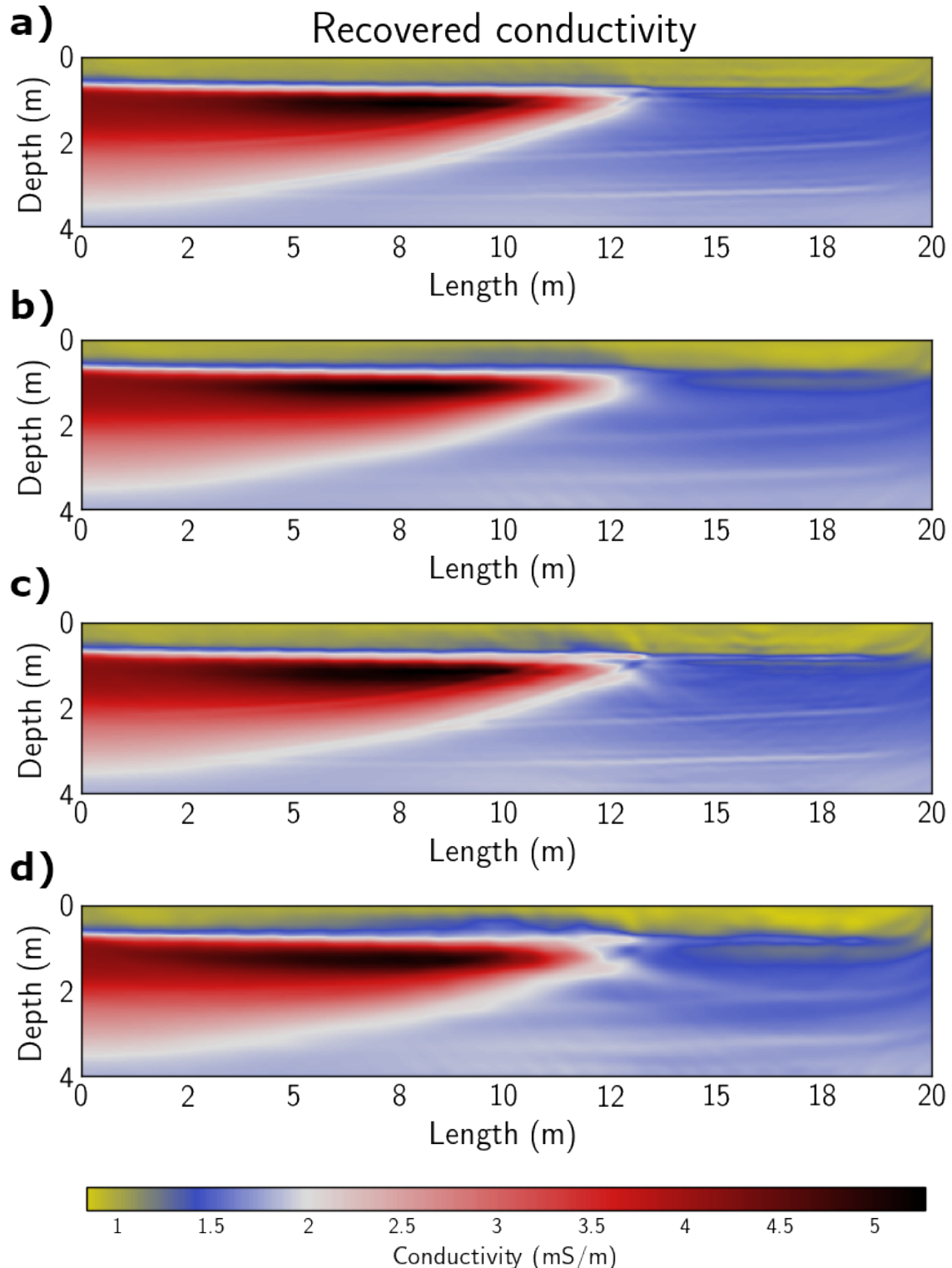


Figure 4.15: Recovered conductivity for the synthetic alluvial aquifer using Joint in a, JEN in b, JOIX in c and JENX in d.

model is more accurately resolved in the initial models.

If the subsurface anomalies are larger than a wavelength, resolving the region of the intrusion below the first layer can be very challenging to resolve using only GPR data. Relying on the envelope of the GPR data (Figure 4.14-**b** and **d**) to correct it can cause overshooting the solution. However, by using the ER sensitivity of the conductivity and the cross-gradients constraint we help mitigate this effect. By doing so, we retain the right values of permittivity and resolve the corner of the low-velocity region, see Figure 4.14-**c** and Figure 4.15-**c**. The cross-gradients constraint also helps stabilize the inversion by enabling to run more iterations without strong artifacts appearing in the recovered parameters.

We show the borehole data for the JOIX inversion (see Figure 4.14-**c** and Figure 4.15-**c**) in Figure 4.16 and Figure 4.17 for permittivity and conductivity respectively. In Figure 4.16 we see that despite underestimating the parameters in the initial model, the permittivity solution accurately approximates the correct values. We also note that permittivity values at depth lack precision. However, the inversion accurately locates the location of boundaries, and it does so approximating the right impedance value.

In Figure 4.17 we also note a lack of accuracy at depth for the recovered conductivity. Similar to the inherent lack of sensitivity in the GPR data due to two-way travel, the ER data is mostly sensitive in an upside-down trapezoid region below the survey line. The sensitivity of the ER data is mostly appreciated in Figure 4.15, where the conductivity is mostly resolved in a trapezoid region. Figure 4.17-**c** also exhibits the lack of GPR and ER sensitivity at depth, where although the data is sensitive to impedance contrasts, it is not capable of resolving the correct magnitude

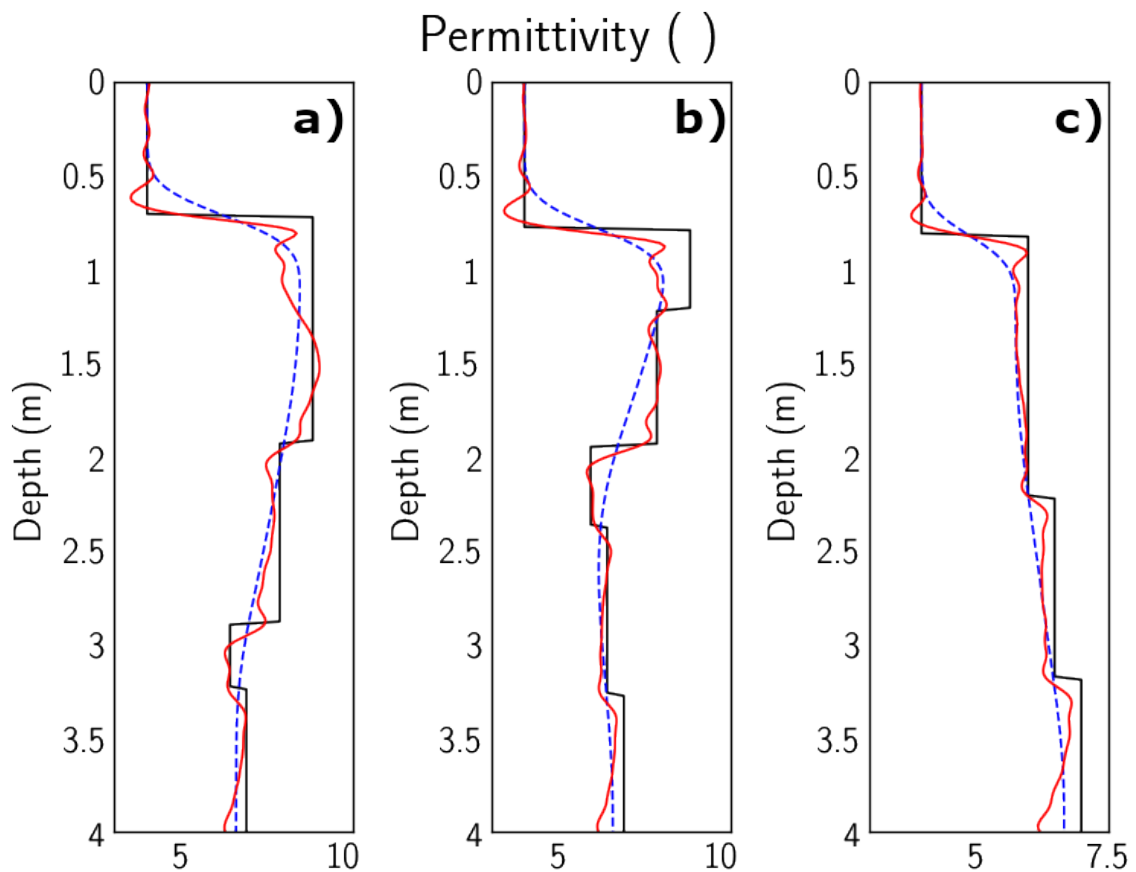


Figure 4.16: Recovered permittivity of the synthetic alluvial aquifer using the JOIX method on boreholes B1, B2 and B3 in a, b and c respectively. True is solid black and initial model is dashed blue.

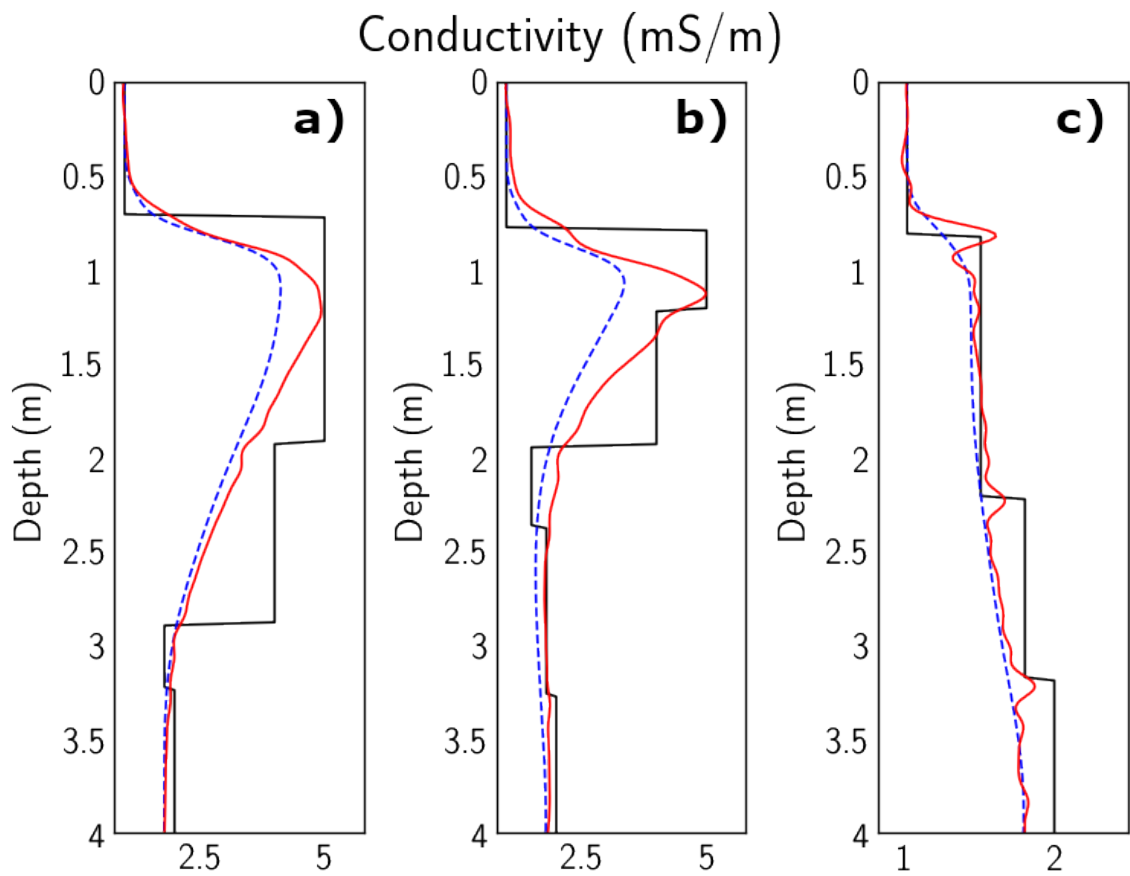


Figure 4.17: Recovered conductivity of the synthetic alluvial aquifer using the JOIX method on boreholes B1, B2 and B3 in a), b) and c) respectively. True is solid black and initial model is dashed blue.

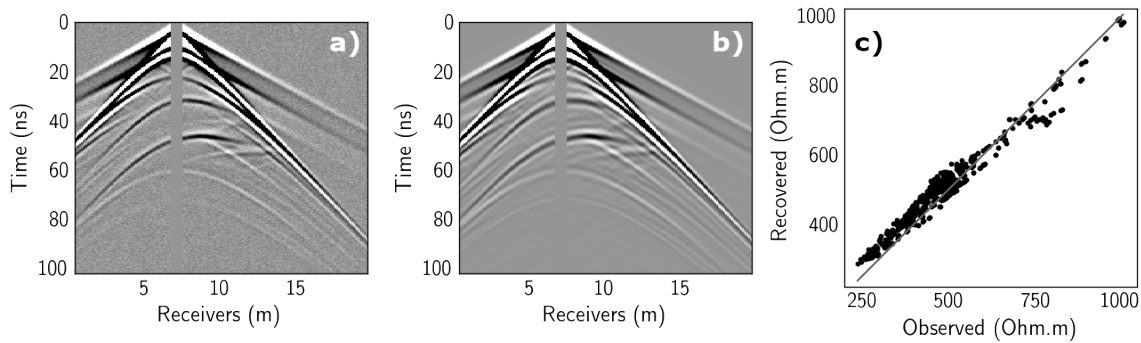


Figure 4.18: Synthetic alluvial aquifer data. Observed a and recovered b GPR data for shot-gather #7. In c observed and recovered ER data. Recovered data correspond to the JOIX method. Amplitudes are clipped to 1.5% of the maximum amplitude in the data.

for the conductivity.

Figure 4.18-**b** gives the recovered GPR data for shot-gather #7 and Figure 4.18-**c** gives both the observed and recovered ER data. We note that most of the reflection events of the observed GPR data below the air-wave refraction are recovered in Figure 4.18-**b**. Figure 4.9-**b** shows the residual of the recovered and observed GPR data. We see that the first and second air-wave refraction are recovered, and the corner of the low-velocity region is resolved up to the noise level. At early times we also note in Figure 4.9-**b** the artifact ripples in the first layer that the inversion has introduced.

4.5 Discussion

Low & high conductivity

Our numerical results show that all the different objective functions $\tilde{\Theta}_w, \Theta_{dc}$ and Θ_τ influence each other when compared to their individual inversions. For both the low and high-conductivity scenarios we find the best results when combining all the objective functions noting improvements in high and low spatial-frequencies, and

Table 4.5: RMS error and average of the RMS errors for all inversion methods of the true and recovered parameters for the low-conductivity scenario. The region where the errors were calculated is the band between 8 and 12 m in length. The boxed results are the smallest value of each column.

Low σ	ϵ	σ	average
Joint	0.3691	0.4927	0.4309
JEN	0.3742	0.4972	0.4357
JOIX	0.3682	0.4912	0.4297
JENX	0.3697	0.4908	0.4303

enhancing amplitude resolution both of the box anomaly and at depth.

In all cases we find the conductivity solutions are significantly of lower spatial resolution when compared to the permittivity solutions. This is due to the inherent spatial resolution limitations of the ER data and the attenuation driven sensitivity of the GPR data to conductivity.

In the low-conductivity scenario we observe a gradual improvement in the conductivity solution by introducing the objective functions $\tilde{\Theta}_w$, Θ_{dc} and Θ_τ . We quantify this improvement by computing the absolute RMS error of the true and recovered conductivity for each method in a region around the box-anomaly and shown in the second column of Table 4.5. However, the improvement in the conductivity solution slightly degrades the best result for the permittivity solution as shown in the first column of Table 4.5. The average of both the permittivity and conductivity RMS absolute errors is displayed in the third column of Table 4.5, indicating that the Joint inversion of GPR and ER data with cross-gradients gives the best overall result.

In the high-conductivity case it is clearer how both the permittivity and conductivity solutions improve when introducing all objective functions. We quantify

Table 4.6: RMS error and average of the RMS errors for all inversion methods of the true and recovered parameters for the high-conductivity scenario. The region where the errors were calculated is the band between 8 and 12 m in length. The boxed results are the smallest value of each column.

High σ	ϵ	σ	average
Joint	0.3708	0.5012	0.4360
JEN	0.3644	0.4992	0.4318
JOIX	0.3666	0.4976	0.4321
JENX	0.3642	0.4915	0.4278

our inversion results in Table 4.6, which is analogous to Table 4.5 but for the high-conductivity scenario. The smallest RMS errors for both parameters are given by introducing all $\tilde{\Theta}_w$, Θ_{dc} and Θ_τ objective functions.

We conclude that in the low-conductivity scenario where the GPR data is strongly sensitive to permittivity, improving the conductivity solution costs a slight degradation of the permittivity solution. In the high-conductivity scenario where the GPR data is strongly affected by attenuation (and thus a lower signal-to-noise ratio), we can improve the permittivity solution by directly using data that is not directly sensitive to permittivity, i.e. ER data using cross-gradients.

Because on average for both low and high-conductivity scenarios the best recovered parameters are obtained using all objective functions (see third column of Tables 4.5 and 4.6), given field GPR and ER data we recommend using all objective functions. In the case where the GPR data is strongly sensitive to permittivity we advice caution with overweighing the envelope gradients of $\tilde{\Theta}_w$ while more leeway can be given to Θ_τ in order to improve the conductivity solution. In the case the GPR data is weakly sensitive to permittivity, we recommend strong weighing on Θ_τ in order to exploit

the ER data for the benefit of the permittivity solution.

Synthetic alluvial aquifer

Compared to the low and high conductivity examples, the initial model we used for the synthetic alluvial aquifer holds much more low-spatial frequency content of the subsurface. This mostly impacts two aspects of the inversion: 1) the initial conductivity model already describes the ER data pretty well, yielding a weak ER update. 2) Using the envelope of the GPR data inhibits the FWI gradient to fully exploit high spatial-frequency features. In this case, the permittivity sensitivity given by the GPR data can be exploited to improve the spatial resolution of the recovered conductivity with the cross-gradients constraint. We find the better results by completely muting the envelope weighting. This weighting strategy is in accordance with the low and high-conductivity discussion above. The cross-gradients constraint on the permittivity enhances low spatial-frequency content on the GPR sensitivity, keeping the inversion artifact-free for more iterations.

Figure 4.19-**a** shows the weights a_w and a_{dc} as a function of iterations. We choose a very small starting value for a_{dc} in order to let the GPR sensitivity resolve the missing high-spatial frequency content. In Figure 4.19-**b** we see that most of the model is resolved in the first 50 iterations. The next 50 iterations resolve mostly the ER data. After 150 iterations the parameters are resolved within the resolution of our methods since no relevant change occurs. Later iterations keep improving the permittivity and conductivity solutions by filling high spatial-frequency details like for example, the corner of the low-velocity region.

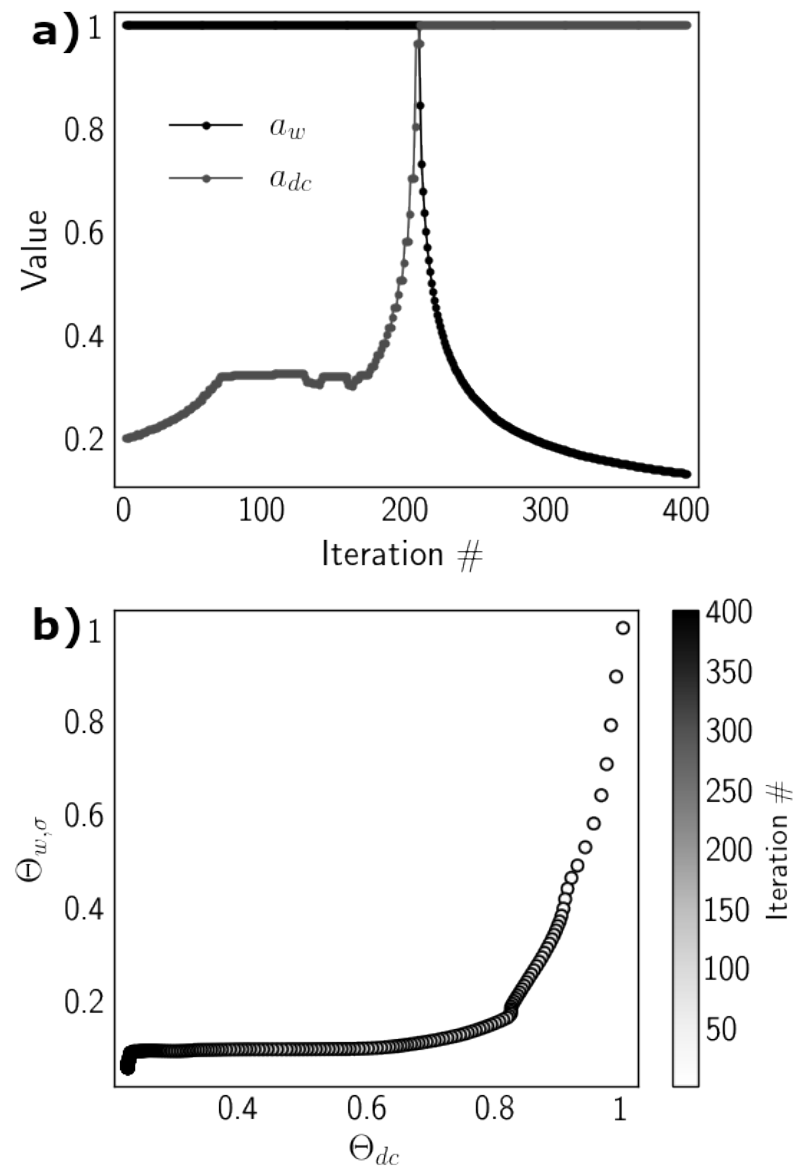


Figure 4.19: Inversion weights of the synthetic alluvial aquifer using the JOIX method. In a values of weights a_w and a_{dc} over iterations. In b objective function values for $\Theta_{w,\sigma}$ and Θ_{dc} .

4.6 Conclusions

We have developed a joint inversion algorithm for one-sided acquired full-waveform GPR and ER data. The algorithm directly joins GPR and ER data, the envelope of the GPR data, and structural information of the parameters using a modified cross-gradients approach. Our three-for-one algorithm manages how much information from each sensitivity is used in the inversion. This algorithm manages effects of strong attenuation and enhances low spatial-frequency content in the recovered electrical permittivity and conductivity.

We tested our inversion scheme on synthetic noisy data and found that even in regions of high attenuation where the GPR data has a signal-to-noise ratio close to one we are able to recover accurate enough subsurface electrical properties. In regions where the attenuation is present but not strong we are able to improve the low spatial-frequency content and accurately resolve sharp boundaries of the recovered parameters.

By joining GPR with ER data we exploit the linkage given by Maxwell's equations of electrical conductivity in both GPR and ER experiments. Borrowing from seismic FWI we use the envelope of the GPR data to better resolve amplitudes at depth and improve the low-spatial frequency content. We have modified the original cross-gradient scheme to fit with our full-physics inversion without the need for computing sensitivity matrices of the data or Hessians of the objective functions.

We note that with field data scenarios it might be the case that the more attenuation in the GPR data the more sensitive to the subsurface the ER data might be (high-conductivity scenario), and the less attenuation in the GPR data the less sensitive to the subsurface the ER data might be (low-conductivity scenario). However,

our algorithm accounts for both scenarios.

We tested our algorithm on a realistic scenario based on an alluvial aquifer deposit. We find that the choice for an initial model greatly impacts the recovered parameters. The best results were found using a smooth velocity model accurate in shallow depths. We note that although demanding, our initial models may be possible to realize with field data using existing workflows such as reflection-traveltime and ER tomography. Our regularization strategy relies on letting the GPR and ER data regularize each other, together with cross-gradients constraints on both permittivity and conductivity. Albeit an initial model, no further a priori information is needed.

Even though we have presented 2D results our algorithm can take into account 3D structure by using 3D GPR and ER forward models. An important caveat of our scheme is assuming ER and GPR are sensitive to a unique electrical conductivity, and in doing so we do not account for frequency dependent conductivity. While in some limited types of materials this approximation is reasonable, in general it is not adequate. Future work will be focused toward accounting for apparent conductivity differences at DC and radar frequencies.

CHAPTER 5:

INVERSION OF 2.5D ELECTRICAL RESISTIVITY DATA USING THE ADJOINT METHOD

¹ We present a 2.5D inversion algorithm of electrical resistivity (ER) data that handles realistic field experiments using low storage requirements. We use the adjoint method directly in the discretized Maxwell's steady state equation that governs the physics of the ER data. In doing so we make no finite difference approximation on the Jacobian of the data and avoid the need to store large and dense matrices. Rather, we exploit matrix-vector multiplication of sparse matrices and find satisfactory results using gradient descent for our inversion routine without having to resort to the Hessian of the objective function. Moreover, our algorithm does not need extra padding of the domain since it robustly accounts for boundary conditions in the subsurface. Given the low storage requirements, our algorithm can be used for joint inversion with other geophysical methods that may impose finer grid constraints (and larger memory requirements) without the need of interpolating the sensitivities of the domain. In an effort to physically appraise the domain of the recovered conductivity, we use a cut-off of the electric current density present in our survey. We tested our algorithm

¹This chapter will be submitted to *Geophysics* and is currently under internal revision.

on synthetic and field data acquired in a controlled alluvial aquifer and were able match the recovered conductivity to borehole observations.

5.1 Introduction

Electrical resistivity (ER) inversions that take into account the full response of the observed data without assuming subsurface geometry are usefull tools for quantitatively characterizing subsurface properties. In recent years, the development of new algorithms for ER data have focused on better approximations to the forward model and to the data sensitivities (Günther *et al.*, 2006; Ha *et al.*, 2006; Pidlisecky *et al.*, 2007; Marescot *et al.*, 2008).

Given that the discretization of the ER governing equations do not require fine grid meshes along the entire computational domain, using second order inversion methods is common practice in most ER inversion schemes (Loke & Barker, 1996; Oldenburg & Li, 1999; Günther *et al.*, 2006; Pidlisecky *et al.*, 2007; Marescot *et al.*, 2008). Although useful on ER data, emerging inversion algorithms that join sensitivities from other time domain geophysical methods (for example ground penetrating radar (GPR) (Domenzain *et al.*, 2019a)) demand either (i) interpolation of the subsurface parameters or (ii) having both sensitivities on the same computational grid (Domenzain *et al.*, 2019a). In Figure 5.1 we see in gray the amount in double precision memory needed to store the Hessian of the objective function for a range of domain sizes,

$$\text{Hessian memory} = \frac{\text{bytes} \cdot (\# \text{ of pixels})^2}{\text{bytes to Gb}}. \quad (5.1)$$

In Ernst *et al.* (2007a) the authors perform a 2D full-waveform inversion (FWI) of GPR borehole data on an aluvial aquifer, a setting with usual electrical parameters

found in the subsurface. The number of pixels in their domain is roughly 10^5 . Commonly used ER inversion methods would require approximately 10^2 Gb of memory to store the Hessian.

In Loke & Barker (1996) and Pidlisecky *et al.* (2007) the authors approximate the Jacobian of the data with a finite difference scheme. The motivation of using adjoint methods is the direct access to the sensitivity of the data in the entire computational domain. The adjoint method for computing ER sensitivities can be applied by either considering the continuous objective function (Günther *et al.*, 2006; Marescot *et al.*, 2008), or the discrete objective function (Pratt *et al.*, 1998; Ha *et al.*, 2006). In Ha *et al.* (2006) the authors use the discrete adjoint method similar to Pratt *et al.* (1998) (in the context of acoustic FWI in the frequency domain) for computing a gradient descent direction in a 2D ER inversion. In their work it is shown that their 2D inversion method costs roughly the same number of flops as Gauss-Newton ER inversion techniques. However, their method does not account for 3D variability of the subsurface. Moreover, their method requires to numerically transform the observed data as an *apparent electric field* and do not account for dissolving boundary conditions in the subsurface.

For our inversion method, we adapt the acoustic FWI of Pratt *et al.* (1998) to a 2D ER inversion that does not need to transform the observed data (Domenzain *et al.*, 2019a). We use a gradient descent algorithm which relieves the need to store the Jacobian of the data and approximate the Hessian of the objective function. For our 2D forward model we use dissolving boundary conditions in the subsurface (Dey & Morrison, 1979) which relaxes the need to do extra padding of the domain. Using the approximation of Pidlisecky & Knight (2008), we account for a 2.5D subsurface

with our 2D forward model. In Pidlisecky & Knight (2008) the authors use a linear combination of 2D electric potentials to approximate the 2.5D solution. In their code it is noted that approximately only four 2D electric potentials suffice.

The amount of memory for computing the ER sensitivities with our method is given by the sum of memory needed to store four 2D electric potentials, and the amount of memory needed to store a 2.5D forward model matrix. With our finite volume discretization, each forward model matrix costs roughly six copies of the domain (5 copies for the 2D forward model and one copy for the 2.5D approximation).

We have,

$$\text{Our method memory} = \frac{\text{bytes} \cdot \# \text{ of pixels} \cdot 4}{\text{bytes to Gb}} + \frac{\text{bytes} \cdot \# \text{ of pixels} \cdot 6}{\text{bytes to Gb}}. \quad (5.2)$$

Figure 5.1 shows in black the amount of memory needed with our method for a range in domain size. Given the low storage requirements, our algorithm can be used for joint inversion with data whose forward models impose finer grid constraints without the need to interpolate the model parameters.

We assess the accuracy of the recovered conductivity at depth using a measure of electric current density in our survey throughout all iterations. Our method relies on the physical principle that the sensitivity of surface acquired ER data is given by electric current lines that return to the surface. Although other methods exist (Oldenburg & Li, 1999) and have been successful in field surveys (Oldenborger *et al.*, 2007), they are costly to compute because more than one inversion is needed for their construction. However, the (costly) exploration of the parameter space given by multiple inversions of the data give a reliable region for apprasing the solution. Rather than presenting a substitute for existing methods, we present ours as a computation-

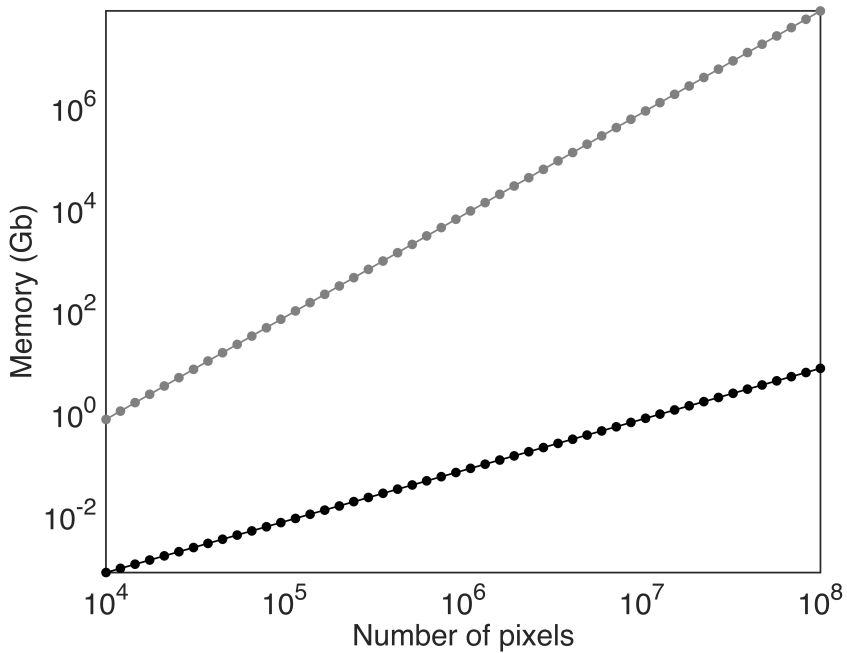


Figure 5.1: Memory needed to compute ER sensitivities as a function of domain size. In gray, using the Hessian of the objective function. In black, using our 2.5D approximation.

ally cheap alternative that takes into account the physics of the ER survey and the different sensitivities of the data throughout the inversion. We show that at worst our approach is conservative in appraising the solution domain.

We show the usefulness of our work with a synthetic example and field data acquired at an alluvial aquifer near Boise, Idaho USA. For the ER field data, we compare our results with previous borehole studies at the same site (Oldenborger *et al.*, 2007; Mwenifumbo *et al.*, 2009) and find similar results for petrophysical parameters and conductivity values.

5.2 Methods

5.2.1 ER 2D forward model

Assuming Ohm's law, the physics of the ER experiment are given by the steady state Maxwell's equations (Pidlisecky *et al.*, 2007),

$$-\nabla \cdot \sigma(x, z) \nabla \varphi(x, z) = \underbrace{\mathbf{i}(\delta(x - s_+) - \delta(x - s_-))}_{s(x, z)}, \quad (5.3)$$

where φ is the electric potential, \mathbf{i} is the current intensity, s_{\pm} is the source-sink location, and σ is the electrical conductivity. Since we are assuming a 1d survey line perpendicular to the y axis, the source term s does not depend on y .

We discretize equation 5.3 using a finite volume method with Neumann and Robin boundary conditions at the air-ground interface and in the subsurface respectively (Dey & Morrison, 1979). The discretization is expressed as a matrix-vector product,

$$\begin{aligned} \mathbf{L}\boldsymbol{\varphi}_{2d} &= \mathbf{s}, \\ \mathbf{d}_{2d} &= \mathbf{M}\boldsymbol{\varphi}_{2d}, \end{aligned} \quad (5.4)$$

where \mathbf{L} is the discretized differential operator of equation 5.3, $\boldsymbol{\varphi}_{2d}$ is the 2d electric potential, \mathbf{s} is the source term, \mathbf{M} is the measuring operator that computes observed voltages, and \mathbf{d}_{2d} is the data of the experiment for one source-sink location. For every pixel in the domain, the matrix \mathbf{L} has as many non-zero entries as neighbors and another entry for itself. Since an inner pixel has four neighbors, an upper bound for the non-zero bands of \mathbf{L} is 5, with each band having as many elements as pixels are in the domain.

5.2.2 Inversion of 2D ER data

We optimize the objective function

$$\Theta_{2d}(\boldsymbol{\sigma}; \mathbf{d}_{2d}^o) = \left\| \underbrace{\mathbf{d}_{2d} - \mathbf{d}_{2d}^o}_{\mathbf{e}_{2d}} \right\|_2^2, \quad (5.5)$$

with respect to the conductivity where \mathbf{e}_{2d} is the residual of the data. In Domenzain *et al.* (2019a) it is shown that the gradient \mathbf{g}_{2d} of the objective function Θ_{2d} with respect to $\boldsymbol{\sigma}$ for one source can be expressed as,

$$\begin{aligned} \mathbf{L}^\top \mathbf{v}_{2d} &= \mathbf{M}^\top \mathbf{e}_{2d} \\ \mathbf{g}_{2d} &= \mathbf{S} \mathbf{v}_{2d}, \end{aligned} \quad (5.6)$$

where,

$$\mathbf{S} = -((\nabla_\sigma \mathbf{L}) \boldsymbol{\varphi}_{2d})^\top, \quad (5.7)$$

is a sparse banded matrix whose entries are explicitly calculated (Domenzain *et al.*, 2019a). Equations 5.6 and 5.7 can also be expressed as,

$$\begin{aligned} \mathbf{g}_{2d} &= \mathbf{J}_{2d}^\top \mathbf{e}_{2d}, \\ \mathbf{J}_{2d} &= \mathbf{ML}^{-1} \mathbf{S}^\top. \end{aligned} \quad (5.8)$$

We note that because we are computing the derivative with respect to $\boldsymbol{\sigma}$ on the discrete operator \mathbf{L} , the boundary conditions of \mathbf{L} are also taken into account in \mathbf{S} . The number of non-zero entries in \mathbf{S} is the same as \mathbf{L} . Each column of \mathbf{S} accounts for one virtual source (Pratt *et al.*, 1998; Ha *et al.*, 2006) and in a given iteration it is computed once per source \mathbf{s} .

5.2.3 ER 2.5D forward model

Equation 5.3 disregards the 3d structure of the earth that is present in field data. In order to account for 3d structure while still assuming no significant change in the y direction, we can express the governing physics of the ER experiment as

$$-\nabla \cdot \sigma(x, z) \nabla \varphi(x, y, z) = s(x, z). \quad (5.9)$$

In order to solve equation 5.9 we use the Fourier-cosine transform in the k_y -domain (Pidlisecky & Knight, 2008),

$$-\nabla \cdot \sigma \nabla \tilde{\varphi}(x, k_y, z) + k_y^2 \sigma \tilde{\varphi}(x, k_y, z) = \frac{1}{2} s(x, z), \quad (5.10)$$

and then use the inverse Fourier-cosine transform to get the electric potential solution in the xz -plane,

$$\varphi(x, y=0, z) = \frac{2}{\pi} \int_0^\infty \tilde{\varphi} dk_y. \quad (5.11)$$

As explained in Pidlisecky & Knight (2008), discretizing equation 5.11 amounts to optimizing for an array \mathbf{k} of k_y values and a corresponding array $\boldsymbol{\omega}$ of weights ω . For completeness, we include the details of this optimization in Appendix A. Both \mathbf{k} and $\boldsymbol{\omega}$ do not depend on the subsurface conductivity. They only depend on the source-receiver geometry.

Once \mathbf{k} and $\boldsymbol{\omega}$ have been computed, we discretize equation 5.10 for each weight k_i in \mathbf{k} as,

$$\mathbf{L}_i = \mathbf{L}^i + k_i^2 \boldsymbol{\sigma}, \quad (5.12)$$

where \mathbf{L}^i is very similar as in equation 5.4 but the Robin boundary conditions in

ER 2.5d forward model

1. retrieve from memory (or compute) \mathbf{k} and ω ,
2. choose $k_i \in \mathbf{k}$ and
3. build $\mathbf{L}_i = \mathbf{L}^i + k_i^2 \sigma$ with the right boundary conditions for that k_i ,
4. solve $\mathbf{L}_i \tilde{\varphi}_i = \frac{\mathbf{s}}{2}$ for $\tilde{\varphi}_i$ and store,
5. repeat 2–5 until all $k_i \in \mathbf{k}$ have been used,
6. compute φ , \mathbf{d} and \mathbf{e} ,

$$\varphi = \frac{2}{\pi} \sum_i \omega_i \tilde{\varphi}_i$$

$$\mathbf{d} = \mathbf{M}\varphi$$

$$\mathbf{e} = \mathbf{d} - \mathbf{d}^o$$

Figure 5.2: Algorithm for computing the 2.5D electric potential given a source \mathbf{s} and conductivity σ .

the subsurface are now different, as dictated by equation F.2. The i 'th 2.5D forward model is,

$$\begin{aligned} \mathbf{L}_i \tilde{\varphi}_i &= \frac{\mathbf{s}}{2}, \\ \tilde{\mathbf{d}}_i &= \mathbf{M}\tilde{\varphi}_i. \end{aligned} \tag{5.13}$$

The full 2.5d forward model, i.e. the discretized expression of 5.11 is,

$$\varphi = \frac{2}{\pi} \sum_i \tilde{\varphi}_i \omega_i. \tag{5.14}$$

In Figure 5.2 we give all the steps of the algorithm for computing φ .

5.2.4 Inversion of 2.5D ER data

We now want to optimize the objective function

$$\Theta(\boldsymbol{\sigma}; \mathbf{d}^o) = \|\underbrace{\mathbf{d} - \mathbf{d}^o}_{\mathbf{e}}\|_2^2, \quad (5.15)$$

with respect to the conductivity where \mathbf{e} is the residual of the data. We compute the gradient \mathbf{g} of Θ by,

$$\mathbf{g} = \mathbf{J}^\top \mathbf{e}, \quad (5.16)$$

where $\mathbf{J} = \nabla_{\boldsymbol{\sigma}} \mathbf{d}$. In order to find an expression for \mathbf{J} we first write \mathbf{d} in terms of $\tilde{\mathbf{d}}_i$,

$$\mathbf{d} = \mathbf{M}\boldsymbol{\varphi} = \underbrace{\mathbf{M} \frac{2}{\pi} \sum_i \omega_i \tilde{\boldsymbol{\varphi}}_i}_{\boldsymbol{\varphi}} = \frac{2}{\pi} \sum_i \omega_i \underbrace{\mathbf{M} \tilde{\boldsymbol{\varphi}}_i}_{\tilde{\mathbf{d}}_i} = \frac{2}{\pi} \sum_i \omega_i \tilde{\mathbf{d}}_i. \quad (5.17)$$

We can now apply $\nabla_{\boldsymbol{\sigma}}$ to equation 5.17,

$$\nabla_{\boldsymbol{\sigma}} \mathbf{d} = \frac{2}{\pi} \sum_i \omega_i \underbrace{\nabla_{\boldsymbol{\sigma}} \tilde{\mathbf{d}}_i}_{\mathbf{J}_i} = \underbrace{\frac{2}{\pi} \sum_i \omega_i \mathbf{J}_i}_{\mathbf{J}} \quad (5.18)$$

Equation 5.18 is a recepie for computing \mathbf{J} . By substituting equation 5.18 in equation 5.16 we have,

$$\begin{aligned} \mathbf{g} &= \frac{2}{\pi} \left(\sum_i \omega_i \mathbf{J}_i \right)^\top \mathbf{e} \\ &= \frac{2}{\pi} \sum_i \omega_i \underbrace{\mathbf{J}_i^\top \mathbf{e}}_{\tilde{\mathbf{g}}_i}. \end{aligned} \quad (5.19)$$

In the last equality we write $\tilde{\mathbf{g}}_i = \mathbf{J}_i^\top \mathbf{e}$ because with a similar approach as in Domenzain *et al.* (2019a) for equation 5.6, from equation 5.13 we have,

$$\begin{aligned}\mathbf{L}_i^\top \tilde{\mathbf{v}}_i &= \mathbf{M}^\top \mathbf{e}, \\ \tilde{\mathbf{g}}_i &= \mathbf{S}_i \tilde{\mathbf{v}}_i,\end{aligned}\tag{5.20}$$

where

$$\mathbf{S}_i = -\left((\nabla_\sigma \mathbf{L}^i) \tilde{\boldsymbol{\varphi}}_i\right)^\top - k_i^2 \operatorname{diag}(\tilde{\boldsymbol{\varphi}}_i)^\top,\tag{5.21}$$

and similarly to equation 5.8 we have $\mathbf{J}_i = \mathbf{M} \mathbf{L}_i^{-1} \mathbf{S}_i^\top$. In conclusion, we compute the gradient \mathbf{g} of equation 5.15 by,

$$\mathbf{g} = \frac{2}{\pi} \sum_i \omega_i \tilde{\mathbf{g}}_i.\tag{5.22}$$

Figure 5.3 gives a summary for computing \mathbf{g} . An upper bound for the size of each \mathbf{S}_i is the size of \mathbf{S} plus one more band (see equation 5.21).

Updating the conductivity

Equation 5.22 gives the gradient \mathbf{g} for equation 5.15 with respect to $\boldsymbol{\sigma}$ for one source. In general, we regularize \mathbf{g} by adding the normalized residual of a reference conductivity $\boldsymbol{\sigma}_o$ and then smoothing in the space-frequency domain. After computing \mathbf{g} with equation 5.22 and normalizing by its largest magnitude we have,

$$\mathbf{g} \leftarrow \mathbf{g} + \beta \frac{\boldsymbol{\sigma} - \boldsymbol{\sigma}_o}{\max(\operatorname{abs}(\boldsymbol{\sigma} - \boldsymbol{\sigma}_o))},\tag{5.23}$$

ER 2.5d objective function gradient

1. compute the 2.5d forward model to get all $\tilde{\varphi}_i$ and \mathbf{e} ,
2. choose $k_i \in \mathbf{k}$,
3. build,

$$\begin{aligned}\mathbf{L}_i &= \mathbf{L}^i + k_i^2 \boldsymbol{\sigma}, \\ \mathbf{S}_i &= -((\nabla_{\boldsymbol{\sigma}} \mathbf{L}^i) \tilde{\varphi}_i)^{\top} - k_i^2 \operatorname{diag}(\tilde{\varphi}_i)^{\top},\end{aligned}$$

4. solve $\mathbf{L}_i^{\top} \tilde{\mathbf{v}}_i = \mathbf{M}^{\top} \mathbf{e}$ for $\tilde{\mathbf{v}}_i$,
5. compute and store $\tilde{\mathbf{g}}_i = \mathbf{S}_i \tilde{\mathbf{v}}_i$,
6. repeat 2–5 until all \mathbf{k} has been used,
7. $\mathbf{g} = \frac{2}{\pi} \sum_i \omega_i \tilde{\mathbf{g}}_i$.

Figure 5.3: Algorithm for finding the 2.5D gradient \mathbf{g} .

where β is a fixed number smaller than one. The gradient \mathbf{g} exhibits large values near the receiver locations. In order to suppress these artifacts, we smooth \mathbf{g} using a space-frequency low-pass filter (Taillandier *et al.*, 2009; Domenzain *et al.*, 2019a). In practice we use a gaussian of width λ ,

$$\lambda = \frac{1}{\Delta r \cdot a}, \quad (5.24)$$

where Δr is the electrode spacing in meters and a is close to one, loosely $0.5 \leq a \leq 1.5$. After smoothing the gradient and normalizing by its largest amplitude, we find the step size as proposed by Pica *et al.* (1990) and adapted for our ER inversion in Domenzain *et al.* (2019a).

In order to enforce positivity constraints on $\boldsymbol{\sigma}$ we do a logarithm change of variable on the objective function, $\Theta(\boldsymbol{\sigma}) = \Theta(\ln(\boldsymbol{\sigma}))$. Using the chain rule we have,

$$\mathbf{g}_{\boldsymbol{\sigma}} = \frac{1}{\boldsymbol{\sigma}} \odot \mathbf{g}_{\ln \boldsymbol{\sigma}}, \quad (5.25)$$

where the subscript denotes the variable under consideration and \odot denotes element wise multiplication. Computing the update, using equation 5.25 and taking the inverse of the logarithm we have,

$$\begin{aligned} \ln(\boldsymbol{\sigma}_{i+1}) &= \ln(\boldsymbol{\sigma}_i) - \alpha \mathbf{g}_{\ln \boldsymbol{\sigma}}, \\ \boldsymbol{\sigma}_{i+1} &= \boldsymbol{\sigma}_i \odot \exp(-\alpha \cdot \boldsymbol{\sigma}_i \odot \mathbf{g}_{\boldsymbol{\sigma}}). \end{aligned} \quad (5.26)$$

Equation 5.26 holds true for one source. In practice however, we update $\boldsymbol{\sigma}$ once all update directions $-\alpha \mathbf{g}$ for all sources in our survey have been computed. The global update $\Delta \boldsymbol{\sigma}$ is the average of all update directions over all sources. At late iterations

when the sensitivity of our data is weak, $\Delta\sigma$ might struggle to find a true descent direction. This issue can be addressed by using *momentum* (Rumelhart *et al.*, 1986) which only costs the storage of the previous iteration update, $\Delta\sigma_{dc\bullet}$. The final update for the conductivity is given by,

$$\begin{aligned}\Delta\sigma &\leftarrow \Delta\sigma + \beta_\bullet \Delta\sigma_{dc\bullet}, \\ \sigma &\leftarrow \sigma \odot \exp(\sigma \odot \Delta\sigma),\end{aligned}\tag{5.27}$$

where β_\bullet is a fixed number smaller than one. Figure 5.4 gives the full algorithm for our inversion.

Solution appraisal

Physically, the sensitivity at depth of the ER survey is given by the electric current density of all shot-receiver pairs in the survey. Depending on our initial model, each forward model in the ER inversion might have different electric current densities throughout iterations. Therefore, throughout the inversion the illumination of the subsurface changes as a function of the observed data and the initial conductivity model.

At each iteration i , we quantify the total electric current density in our inversion by summing the absolute value of the electric potentials φ given by our forward models (see equation 5.14),

$$\Psi_i = \sum_j |\varphi_j|,\tag{5.28}$$

where j runs through all forward models. As iterations proceed, we keep adding the previous Ψ_i to the new one to obtain a final measure of electric current density Ψ ,

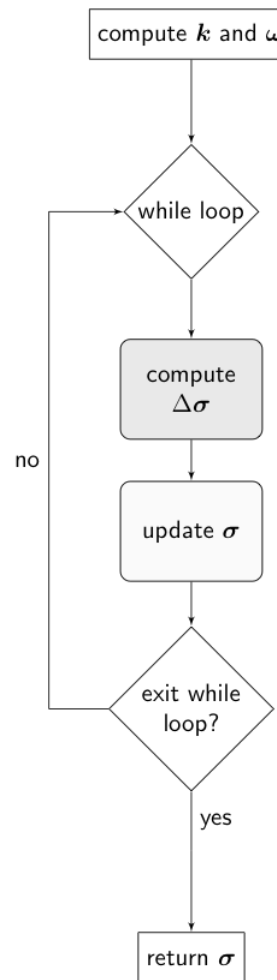


Figure 5.4: 2.5d inversion algorithm.

then we normalize Ψ by its largest amplitude,

$$\begin{aligned}\Psi &= \sum_i \Psi_i \\ \Psi &\leftarrow \frac{\Psi}{\max(\Psi)}.\end{aligned}\tag{5.29}$$

Given the harmonic nature of the electric potential, the field Ψ will have a level curve beyond which the electric current lines will no longer return to the surface. We choose this level curve as a cut-off for Ψ from which all level curves below this cut-off are considered to not contain relevant information. The resulting image for Ψ is then a collection of ones in the xz -plane above the cut-off value.

5.3 Examples

5.3.1 Synthetic data example

We test our algorithm on a synthetic scenario as shown in Figure 5.5-a. The model consists of a 20m by 4m subsurface domain with a 10mS/m cylindrical anomaly embedded in a 5mS/m background. We use 17 electrodes spaced 1m apart with all possible dipole-dipole, Wenner and Schlumberger arrays. The full discretized domain is of size 81×401 with a square pixel size of 0.05m.

Our initial model is a homogeneous conductivity equal to the background of our model. Besides smoothing the gradients \mathbf{g} , for this example we do not impose regularization on the inversion. We choose a smoothing factor of $a = 1.1$ (see equation 5.18) and a value of $\beta_\bullet = 0.02$.

In Figure 5.5-b we see the recovered conductivity in the entire computational domain, and in Figure 5.5-c we see the recovered conductivity with a current density

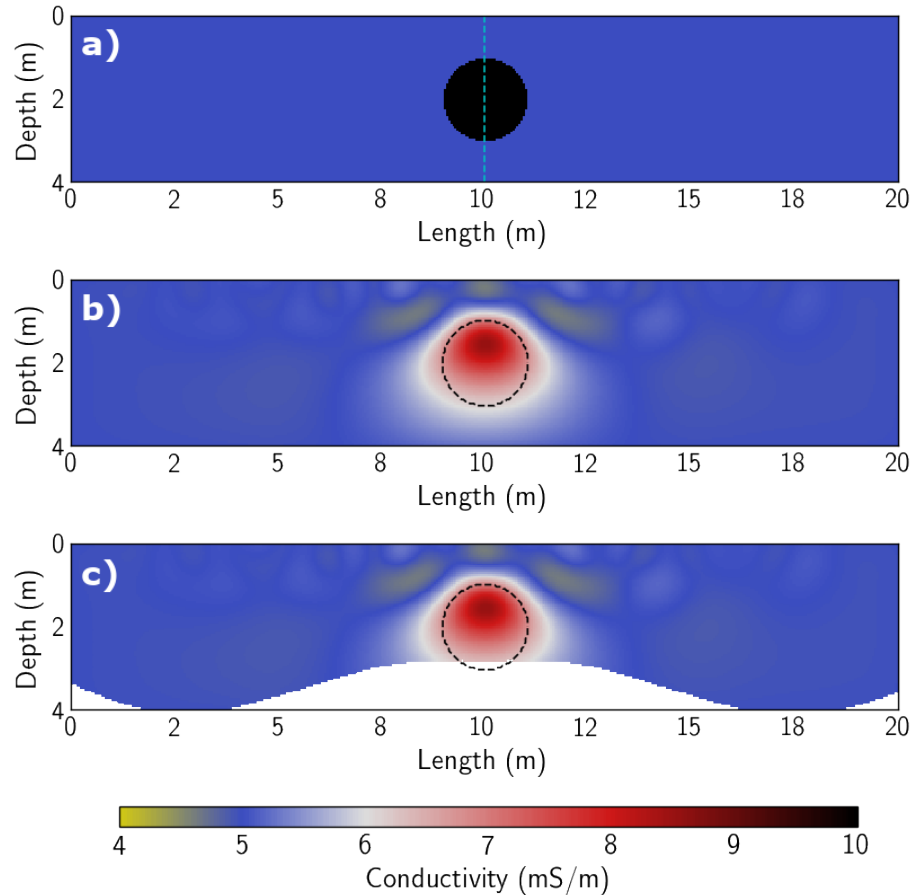


Figure 5.5: True a, recovered b and appraised c conductivity for the synthetic example. The dashed cyan line in a represents a borehole location. The dashed black line (in b and c) represents the contour of the cylinder.

cut-off of 0.025%. Our solution appraisal technique is able to remove parts of the domain where we have a poor constraint in our solution (bottom of the domain) but keep parts where the recovered conductivity remains close to the true model. We note that by choosing a cut-off that eliminates the electric current leaving the domain, we are conservatively assessing our solution.

In Figure 5.6 we show a borehole comparison along the center of the domain.

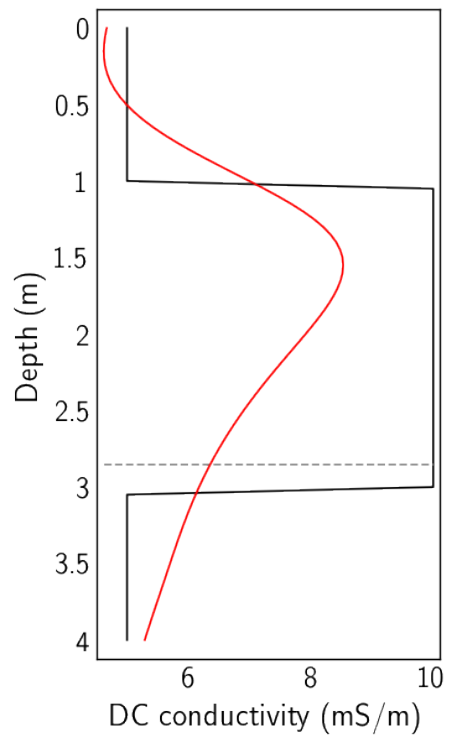


Figure 5.6: True (black) and recovered (red) conductivity at the center borehole for the synthetic example. The dashed gray line shows the cut-off for our appraised solution.

5.3.2 Field data example

We acquired field data at the Boise Hydrological Research Site (BHRS) in May 2019. The site is an alluvial aquifer next to the Boise river as seen in Figure 5.7. The water flow in the river is controlled by a nearby dam and is increased throughout spring as warmer temperatures thaw the snowpack in the nearby Sawtooth mountain range. We aimed our experiment to take place when the water table was at its highest point without the site being flooded. We used an *IRIS Syscal Pro* resistivity system with a total of 36 electrodes spaced 1m apart in a one dimensional line perpendicular to the river as shown in Figure 5.7. Our survey consisted of all possible dipole-dipole and Wenner arrays for a total of 1175 source-receiver pairs. Although flat, the survey line has a slight tilt ($\approx 0.4\text{m}$) in elevation going from low to high away from the river.

Based on knowledge of site stratigraphy (e.g. Bradford *et al.* (2009b)) the position of the line perpendicular to the river was chosen to enhance the variability of conductivity in the xz -plane while keeping the y coordinate variability of the conductivity constant. For each source-receiver pair the raw data recorded by the Syscal Pro is in units of volts, paired with readings of source current magnitude (positive and in units of Amperes), apparent resistivities computed by the system (in units of Ohm per meter), and a measure of standard deviation (each shot was performed eight times).

Preprocessing

For our inversion we take as data only the voltage readings. However, before performing our inversion we use all the Syscal Pro data to enhance the quality of our inversion in three steps. 1) Remove the negative apparent resistivities given by the Syscal Pro system since these data points are not physical and are contaminated by

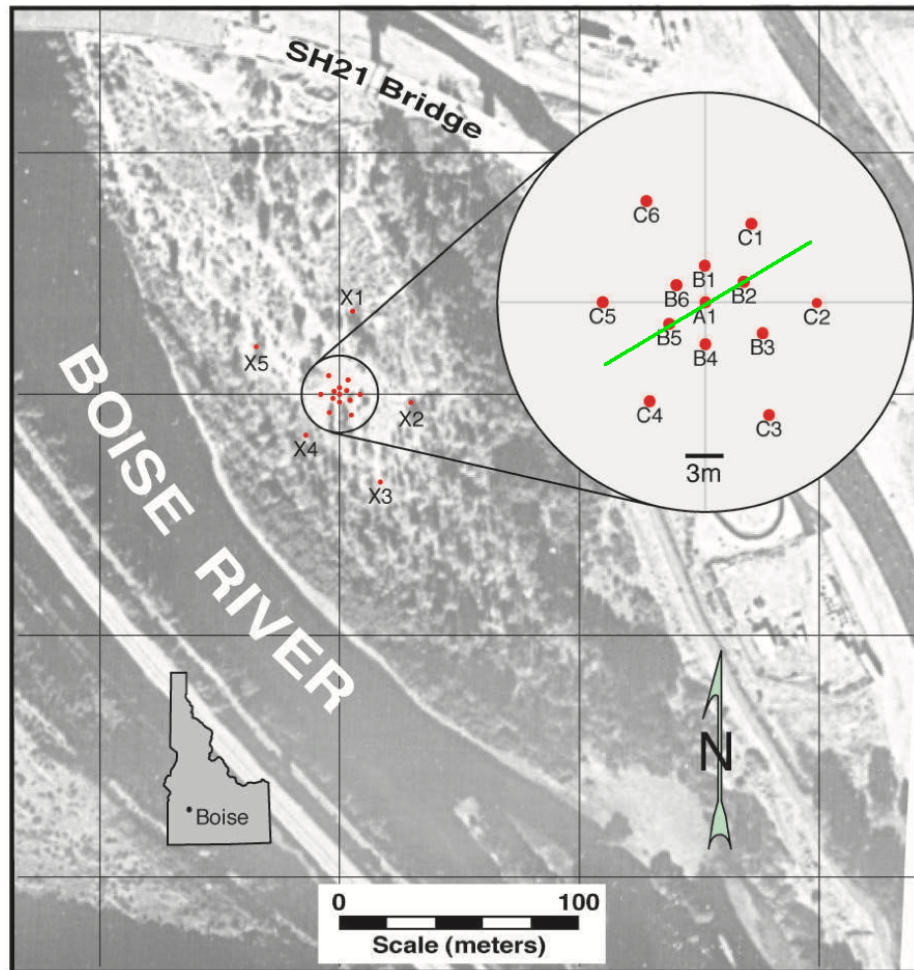


Figure 5.7: Geographic location of the Boise Hydrological Research Site (BHRS). The red dots denote the existing boreholes. Our survey line crossed boreholes B5, A1 and B2 as shown by the green line.

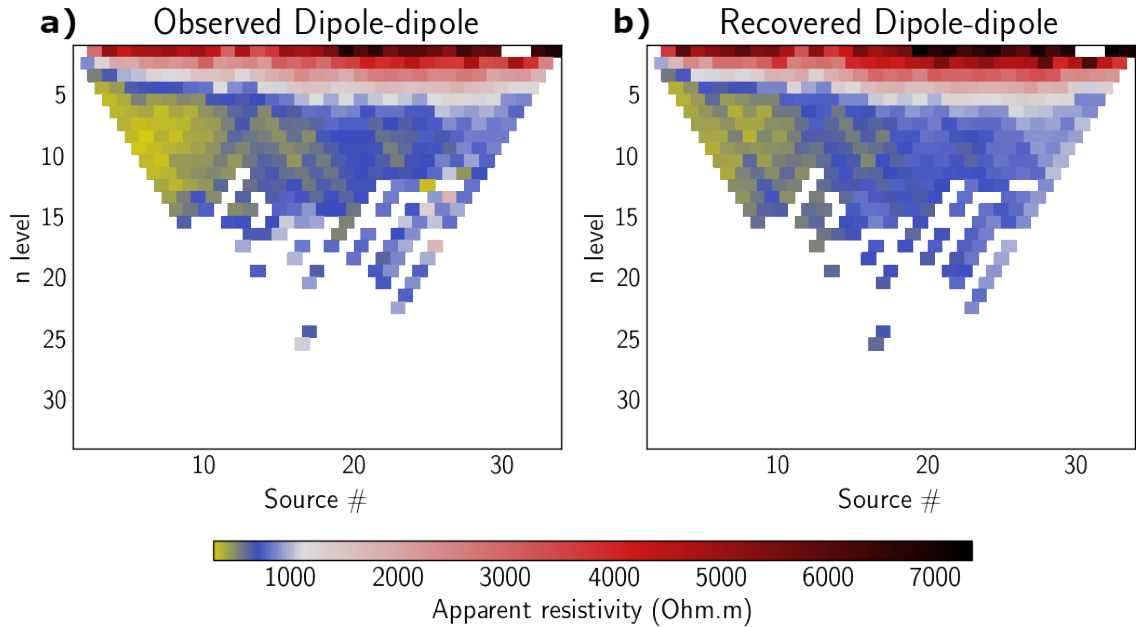


Figure 5.8: Dipole-dipole pseudo section with a-spacing equal to 1m from the BHRS.

noise. 2) Eliminate data points whose standard deviation is more than a fixed cut-off. In this case the cut-off was 5 standard deviations. 3) Divide the voltage readings by their respective source current magnitude. This last step is done to enable multi source-receiver pairs in each forward model of our inversion. We will refer to multi source-receiver pairs that share the same source as *shot-gathers*. Our data consists of 342 shot-gathers. The next step is to compute the weights \mathbf{k} and $\boldsymbol{\omega}$ (see Figure F.1). Figure 5.8-a and Figure 5.9-a give the observed but preprocessed apparent resistivities of the dipole-dipole with a-spacing equal to 1m and Wenner arrays respectively.

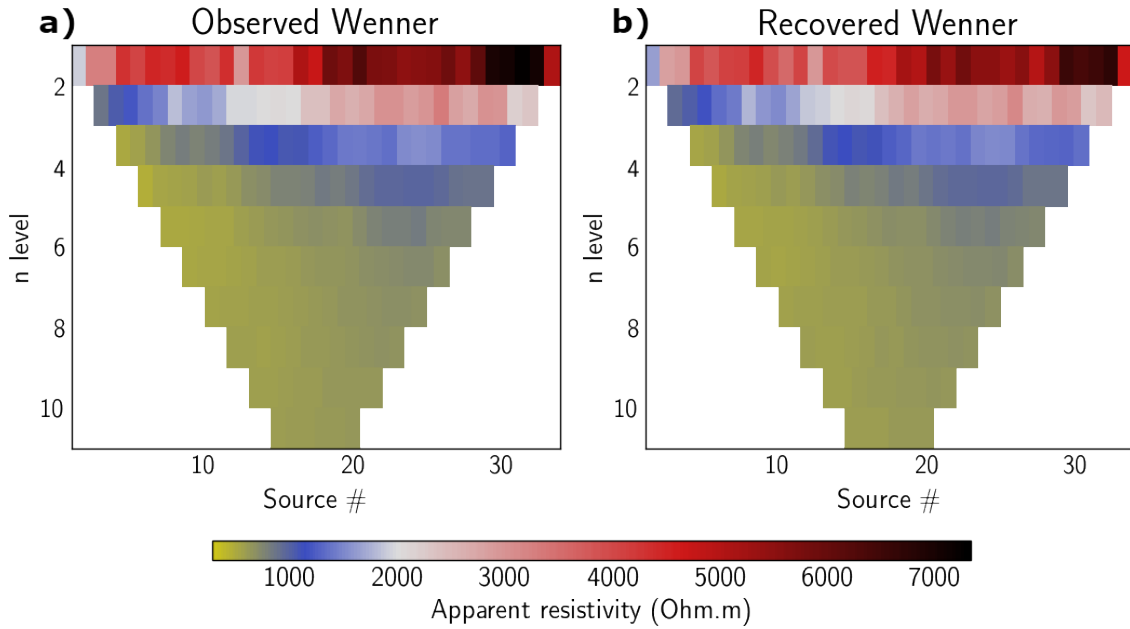


Figure 5.9: Wenner pseudo-section of the BHRS.

Inversion

Our initial model is a homogeneous subsurface with a conductivity equal to 2mS/m. We regularize the inversion using a homogeneous reference conductivity equal to our initial model, and weighting factors of $\beta = 0.001$ and $\beta_{\bullet} = 0.5$. The full discretized domain is of size 301×901 with a square pixel size of 0.05m. Figure 5.10 gives the recovered conductivity corrected for topography and with a current density cut-off equal to 0.002%. Figure 5.11 shows the observed vs recovered data.

We evaluate our results with water table depth, neutron porosity (Barrash & Clemo, 2002), and capacitive conductivity (Mwenifumbo *et al.*, 2009) taken from borehole measurements. For our borehole analysis we choose to use the full domain of our solution. We do this because as explained below we are still able to extract meaningful physical information of the subsurface, and as noted in the synthetic ex-

ample, our cut-off criteria can be overly conservative. The water table depth was 1m and measured the same day the survey was done. Figure 5.10 shows our recovered conductivity accurately images the water table boundary. We further note the wet inland intrusion of the river is accurately represented in our image.

Figure 5.12 shows the normalized porosity and recovered conductivity along the entire computational domain. Qualitatively, our recovered conductivity and measured porosity follow the same low-frequency trend. This trend is mostly appreciated in Figure 5.12-a for borehole B5, where the peak-trough-peak shape of the porosity is closely followed by the recovered conductivity beyond our solution appraisal cut-off.

Quantitatively, we compare our inversion results following Oldenborger *et al.* (2007) who perform a time lapse borehole ER monitoring of the same site in Summer of 2004. Their analysis uses Archie's law (Archie *et al.*, 1942) to compare the formation factor derived by ER recovered conductivity and the formation factor derived by the neutron porosity. For each borehole B5, A1 and B2 we compute the formation factor with our recovered conductivity,

$$F_{ER} = \frac{\sigma_f}{\sigma_z}, \quad (5.30)$$

where σ_z denotes our recovered conductivity along the borehole and σ_f is the fluid conductivity. We take $\sigma_f = 20\text{mS/m}$ as given by Oldenborger *et al.* (2007). We then invert in depth for the cementation factor m using the neutron porosity (ϕ) and the porosity derived from F_{ER} ,

$$\phi_{ER} = \left(\frac{1}{F_{ER}} \right)^{1/m}. \quad (5.31)$$

This gives us a depth profile for m . Using m we compute the formation factor from

Table 5.1: Formation and cementation factor appraisal for each borehole using recovered conductivity and neutron porosities. Our results correlate well to a previous borehole ER survey at the same site up to a standard deviation of at most ± 1 .

	B5	A1	B2
m	1.7 ± 0.3	1.8 ± 0.3	1.6 ± 0.1
F_{ER}	12.5 ± 3	13.3 ± 3	13.9 ± 3
F_ϕ	12.5 ± 3	13.3 ± 3	13.9 ± 3

the neutron porosity as,

$$F_\phi = \frac{1}{\phi^m}. \quad (5.32)$$

Oldenborger *et al.* (2007) give average values of $F_{ER} = 13 \pm 4$, $m = 1.7$ and $F_\phi = 13 \pm 4$.

In Table 5.1 we find similar values (within ± 1 standard deviation) for F_{ER} , F_ϕ and m with our recovered conductivity.

Figure 5.13 shows our recovered conductivity next to the capacitive conductivity as measured by Mwenifumbo *et al.* (2009). Their experiment was performed in the month of November, when the river water flow had significantly decreased to a 2m deep water table. Even though our experiments were performed with different ground water conditions, our recovered conductivity is within the same order of magnitude and follows close resemblance inside our appraised solution. Beyond our appraised solution near 10m in depth, both conductivity profiles show an up-ward trend that is also present in the neutron porosity (Figure 5.12).

5.4 Conclusions

We have developed an adjoint based method for inverting 2.5D electrical resistivity (ER) data. Our algorithm makes no assumption of the subsurface conductivity geom-

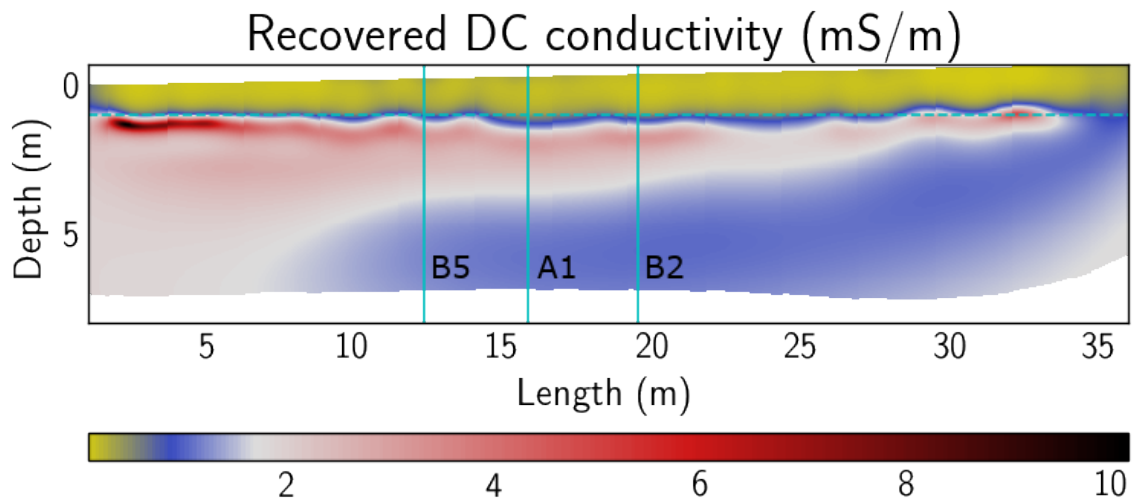


Figure 5.10: Recovered conductivity from the BHRs with topographic correction. The dashed cyan line represents the water table depth as measured on site (1m deep). The solid cyan lines represent the borehole positions.

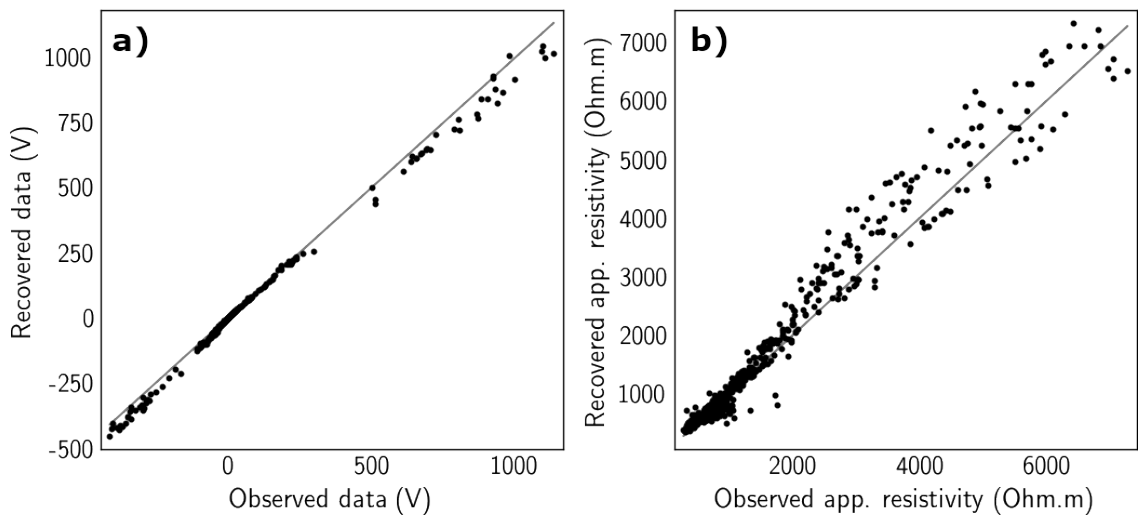


Figure 5.11: Observed vs recovered ER data acquired at the BHRs.

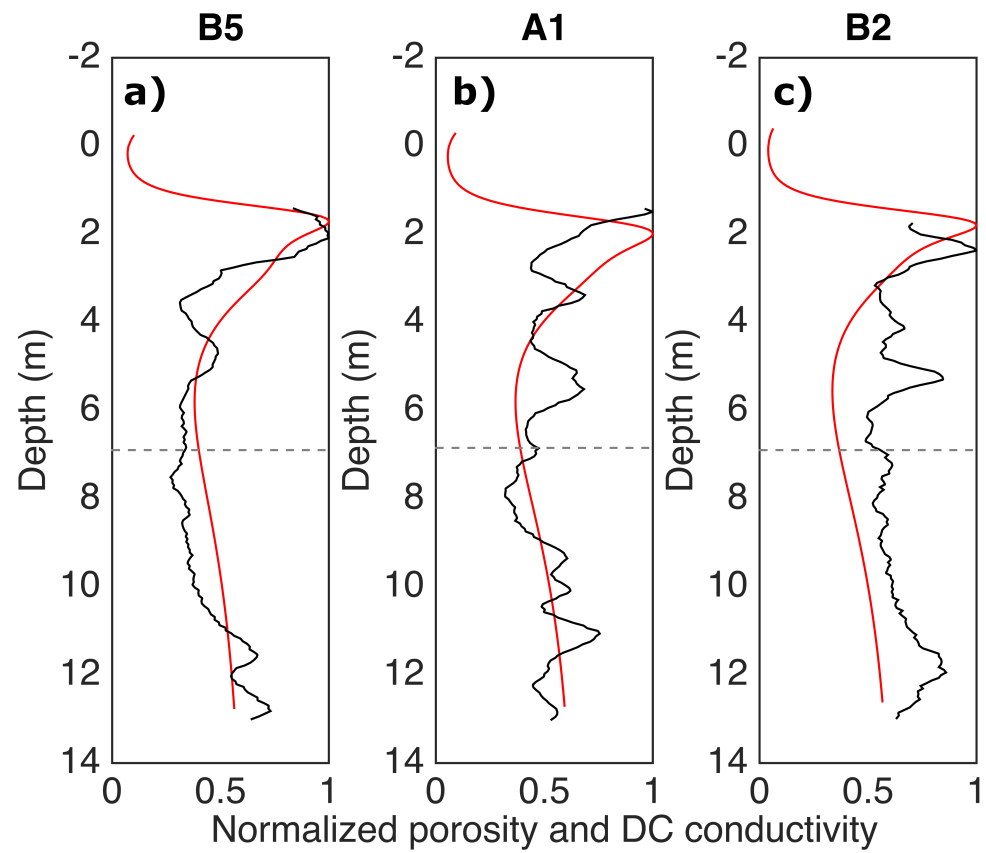


Figure 5.12: Normalized recovered conductivities (red) and borehole neutron porosity (black) at borehole locations in the BHRS. The dashed gray line shows the cut-off for our appraised solution.

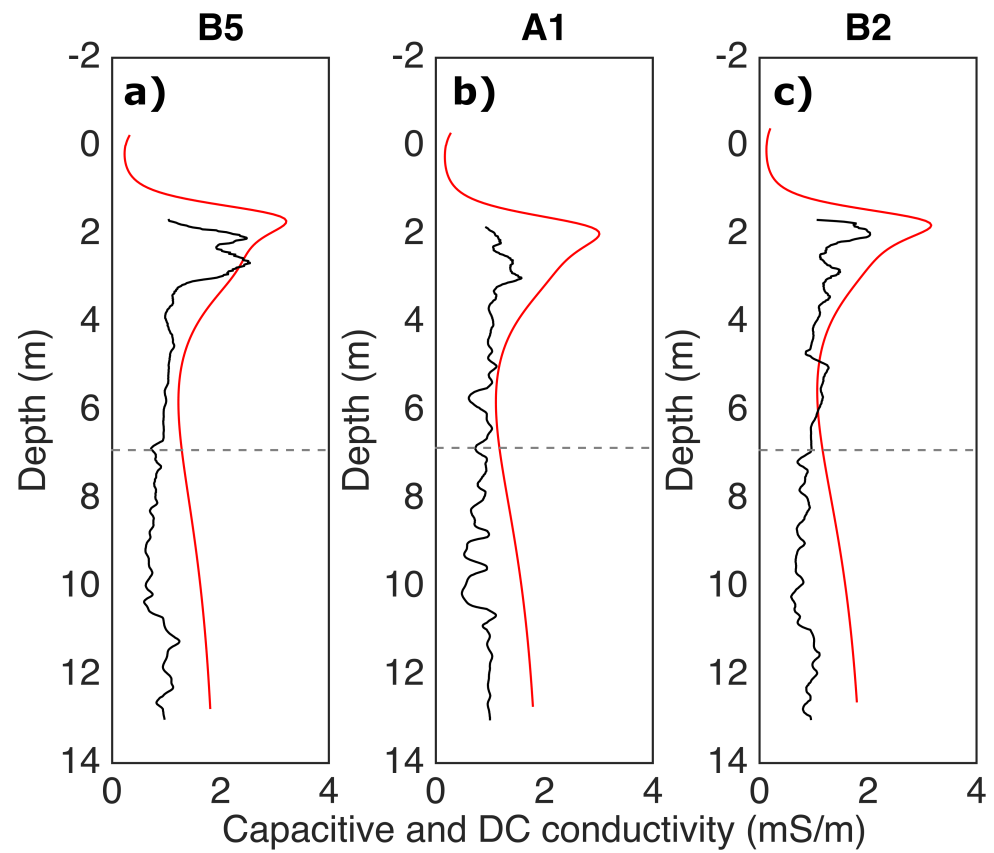


Figure 5.13: Recovered ER (with our method - in red) and capacitive conductivities (black) at borehole locations in the BHRS. The dashed gray line shows the cut-off for our appraised solution.

etry. We directly obtain the sensitivity of the data in the entire domain and do not need to approximate the Jacobian of the data using finite differences. Moreover, we take into account dissipating boundary conditions in the subsurface and do not need to store large dense matrixies (like the Jacobian of the data and the Hessian of the objective function). This enables us to very finely discretize the subsurface with feasible memory requirements. As a result, our algorithm can be used for joint inversion with data whose forward models impose finer grid constraints (for example, ground penetrating radar (GPR)) without the need to interpolate the model parameters.

In order to assess the quality of the recovered parameters, we use a measure of the electric current density present in our domain throughout iterations. This method for quality assessment takes into account the physics of the ER survey, the data, the model parameters throughout iterations and does not need extra inversions with different initial models. At worst our method is conservative in assessing the quality of the recovered parameters. However, it is less accurate than other existing methods that explore the model space in a more exhaustive way.

We tested our algorithm on a synthetic example and on field data aquired at an alluvial aquifer near Boise, Idaho USA. We find good correlation of our field data results with neutron porosity and capacitive conductivity borehole measurements taken on the site in previous surveys.

CHAPTER 6:

CONCLUSIONS

Recovering electrical properties of the subsurface is a valuable recourse for ground-water and geothermal exploration, contaminant and hazard mitigation, and carbon-dioxide sequestration. Given the increasing demand in water, non-fossil based energy, and carbon-dioxide mitigation, electrical methods prove to be an important tool for society as our planet enters an unprecedented age of rapid change in climate.

Full-waveform inversion (FWI) of ground penetrating radar (GPR) is a promising technique for recovering permittivity and conductivity values of the subsurface without imposing geometrical assumptions of their underground location. Current literature on FWI-GPR has mostly focused with transillumination surveys. When dealing with surface acquired data, using the full waveform in the GPR data can easily lead to local minima solutions due to the lack of transmission information, attenuation in the media, and lack of low frequencies.

Electrical resistivity (ER) is a common technique for recovering conductivity of the subsurface. Most ER inversion methods use the full response of the ER data and are able to recover conductivity at depth without imposing geometrical assumptions. However, when compared to GPR sensitivity, the resolution of the ER sensitivity is of lower spatial-frequency content. Fortunately ER and GPR hold complementary sensitivities to the subsurface. GPR is sensitive to conductivity through attenuation

and reflection while ER is directly sensitive to conductivity.

We exploit the complementary relationship of GPR and ER sensitivities in a joint inversion scheme that takes into account the full physical response of both GPR and ER data. Our algorithm makes no petrophysical assumptions enabling it to be site independent. Rather the two types of data are combined so that GPR effectively supports ER in regions of low conductivity while ER supports GPR in regions with strong attenuation. In cases where the attenuation is high we add structural similarity constraint so that the ER sensitivity to the conductivity can enhance the resolution and accuracy of the permittivity solution. Structural similarity constraints can also improve the recovered conductivity by letting the permittivity enhance high spatial-frequency content in the conductivity solution.

Existing methods for inverting ER data rely on the computation and storage of the Jacobian of the data and the Hessian of the objective function. The amount of memory needed by these methods can become unfeasible when using the fine discretization requirements of the GPR-FWI scheme. We have developed a 2.5D ER adjoint method inversion that is capable of recovering accurate subsurface conductivity from field data and relaxes the amount of required memory. Having feasible computational methods for both GPR and ER inversions is an important step for using our joint inversion algorithms on field data.

In Chapter 3 we develop the joint conductivity update that takes into account both the ER and GPR sensitivities. In this inversion approach, we assume electrical parameters are frequency independent. We note that for a variety of earth materials the DC and effective conductivity vary by a factor less than 5. In cases where the discrepancy is more than a factor of five, the attenuation might be too strong for

the GPR data to hold meaningful information about the subsurface. Although not true in general, assuming frequency independent parameters enables us to evaluate the algorithm and comprises a reasonable trade-off between computation cost, field applications, the full use of the GPR waveform, a lack of enforced assumptions of subsurface geometry and petrophysical models. We find that our joint inversion outperforms both GPR and ER separate inversions and determine that GPR effectively supports ER in regions of low conductivity while ER supports GPR in regions with strong attenuation.

In Chapter 4 we enhance our algorithm by incorporating the envelope of the GPR data as an extra objective function. Furthermore, we also impose an iterative structural constraint using the recovered parameters and the cross-gradients objective function. Contrary to the existing literature using cross-gradients, our enhanced algorithm is still based on gradient descent. This relaxes the computational memory cost and enables us to use cross-gradients while also using the full time response of the GPR data (as opposed to modeling the GPR experiment in the frequency domain and approximating the Hessian of the objective function). We find that exploiting low frequency content in the GPR data and assuming structural similarities between electrical permittivity and conductivity, we are able to recover subsurface parameters in regions where the GPR data has a signal-to-noise ratio close to one.

In Chapter 5 we develop a low storage 2.5d ER inversion algorithm that accurately describes field data in realistic scenarios. Our algorithm makes no assumption of the conductivity geometry, accurately models the boundary conditions in the subsurface and does not need the storage of large dense matrixies (like the Jacobian of the data and the Hessian of the objective function). We tested our algorithm on synthetic

and field data acquired at an alluvial aquifer near Boise, Idaho USA. We find good correlation of our field data results with porosity logs taken at the site. Given the low storage requirements, our algorithm can be used for joint inversion with data whose forward models impose finer grid constraints without the need to interpolate the model parameters.

6.1 Discussion

The work presented in this dissertation has been a growing seed that has fruitfully enriched the geophysical community through numerous conference presentations and two journal papers currently under review. In what follows, I will discuss the paths I see for continuing and enhancing our joint inversion algorithm.

For our initial models we demand long wavelength structure that could realistically be obtained from reflection tomography and analysis of direct arrivals. Such initial models require careful user input. While accurate velocity models can be obtained using these methods, the promise of relieving our inversions from a priori information is compromised. Another caveat of this approach is that conductivity would not be accounted for. It is my intuition that a more accurate method is yet to be invented.

If the GPR data exhibits air-wave refractions it is usually because there is a strong shallow reflector. In general, we do not know neither the depth or velocity of this reflector. A possible path for building a better initial model could be using the idea introduced in the *virtual refraction* method (Mikesell *et al.*, 2009). This method exploits artifacts in the virtual shot gather given by seismic interferometry in order to obtain information about the subsurface. In particular, the method uses an artifact caused by having sparse illumination and a shallow in-depth refractor. Our case is different since the refractor is the air layer. We would have to analyze the virtual shot

gather and discover a new type of artifact caused by having such a shallow reflector. It would be a method inspired by the virtual refraction but different overall - a *virtual reflectio-refraction*. Since this method was developed for wavefields traveling in media where velocity increases in depth and our case is the opposite we would have to modify it. Such a method would also have to account for attenuation in the media, which could be done with the interferometric multi-dimensional deconvolution method (Snieder *et al.*, 2007).

Another approach for relaxing the initial model could be to further enhance our FWI-GPR objective function by 1) a frequency stepping scheme and 2) variable weights for the envelope sensitivity. It has been shown in the literature (Meles *et al.*, 2012) that a frequency stepping approach can benefit the resolution of the recovered parameters. Allowing the envelope sensitivity to resolve long wavelength structure at early iterations, and then letting the higher frequency sensitivities take over the inversion might help resolve regions of the subsurface located next to sharp impedance boundaries.

Lastly, I believe that building a scientific technology is half the path, the other half is applying it. I would be delighted to see how researchers from other disciplines embrace our work for answering questions we have not thought about. Personally, I would like to try using lower frequency GPR antennas to solve for deeper subsurface features. Depending on the subsurface properties, the diffusion limit of electromagnetic propagation might be met with lower frequency antennas, so we would have to account for that either in our algorithm or in choosing the right field antennas. Some colleagues believe longer antennas (8m at most in length) might be cumbersome to move in the field. Perhaps attaching the antennas to a zip line that gets taut when

moving and loose when acquiring the data would solve the problem.

REFERENCES

- Archie, Gustave E, *et al.* 1942. The electrical resistivity log as an aid in determining some reservoir characteristics. *Transactions of the AIME*, **146**(01), 54–62.
- Babcock, Esther, & Bradford, John H. 2015. Reflection waveform inversion of ground-penetrating radar data for characterizing thin and ultrathin layers of nonaqueous phase liquid contaminants in stratified media. *Geophysics*, **80**(2), H1–H11.
- Baeten, Guido, de Maag, Jan Willem, Plessix, René-Edouard, Klaassen, Rini, Qureshi, Tahira, Kleemeyer, Maren, Kroode, Fons ten, & Ruijie, Zhang. 2013. The use of low frequencies in a full-waveform inversion and impedance inversion land seismic case study. *Geophysical Prospecting*, **61**(4), 701–711.
- Barrash, Warren, & Clemo, Tom. 2002. Hierarchical geostatistics and multifacies systems: Boise hydrogeophysical research site, Boise, Idaho. *Water Resources Research*, **38**(10), 14–1.
- Beff, Laure, Günther, Thomas, Vandoorne, Bertrand, Couvreur, Valentin, & Javaux, Mathieu. 2013. Three-dimensional monitoring of soil water content in a maize field using Electrical Resistivity Tomography. *Hydrology and Earth System Sciences*, **17**(2), 595–609.
- Benedetto, Andrea. 2010. Water content evaluation in unsaturated soil using GPR

- signal analysis in the frequency domain. *Journal of Applied Geophysics*, **71**(1), 26–35.
- Berenger, J-P. 1996. Perfectly matched layer for the FDTD solution of wave-structure interaction problems. *IEEE Transactions on antennas and propagation*, **44**(1), 110–117.
- Bergmann, Peter, Schmidt-Hattenberger, Cornelia, Kiessling, Dana, Rücker, Carsten, Labitzke, Tim, Henninges, Jan, Baumann, Gunther, & Schütt, Hartmut. 2012. Surface-downhole electrical resistivity tomography applied to monitoring of CO₂ storage at Ketzin, Germany. *Geophysics*, **77**(6), B253–B267.
- Binley, Andrew, Cassiani, Giorgio, Middleton, Roy, & Winship, Peter. 2002. Vadose zone flow model parameterisation using cross-borehole radar and resistivity imaging. *Journal of Hydrology*, **267**(3-4), 147–159.
- Bozdağ, Ebru, Trampert, Jeannot, & Tromp, Jeroen. 2011. Misfit functions for full waveform inversion based on instantaneous phase and envelope measurements. *Geophysical Journal International*, **185**(2), 845–870.
- Bradford, John H. 2006. Applying reflection tomography in the postmigration domain to multifold ground-penetrating radar data. *Geophysics*, **71**(1), K1–K8.
- Bradford, John H. 2007. Frequency-dependent attenuation analysis of ground-penetrating radar data. *Geophysics*, **72**(3), J7–J16.
- Bradford, John H, & Deeds, Jacob C. 2006. Ground-penetrating radar theory and application of thin-bed offset-dependent reflectivity. *Geophysics*, **71**(3), K47–K57.

- Bradford, John H, Harper, Joel T, & Brown, Joel. 2009a. Complex dielectric permittivity measurements from ground-penetrating radar data to estimate snow liquid water content in the pendular regime. *Water resources research*, **45**(8).
- Bradford, John H, Clement, William P, & Barrash, Warren. 2009b. Estimating porosity with ground-penetrating radar reflection tomography: A controlled 3-D experiment at the Boise Hydrogeophysical Research Site. *Water Resources Research*, **45**(4).
- Brunet, Pascal, Clément, Rémi, & Bouvier, Christophe. 2010. Monitoring soil water content and deficit using Electrical Resistivity Tomography (ERT)–A case study in the Cevennes area, France. *Journal of Hydrology*, **380**(1-2), 146–153.
- Bunks, Carey, Saleck, Fatimetou M, Zaleski, S, & Chavent, G. 1995. Multiscale seismic waveform inversion. *Geophysics*, **60**(5), 1457–1473.
- Carrigan, Charles R, Yang, Xianjin, LaBrecque, Douglas J, Larsen, Dennis, Freeman, David, Ramirez, Abelardo L, Daily, William, Aines, Roger, Newmark, Robin, Friedmann, Julio, *et al.* 2013. Electrical resistance tomographic monitoring of CO₂ movement in deep geologic reservoirs. *International Journal of Greenhouse Gas Control*, **18**, 401–408.
- Courant, Richard, Friedrichs, Kurt, & Lewy, Hans. 1967. On the partial difference equations of mathematical physics. *IBM journal of Research and Development*, **11**(2), 215–234.
- Cucker, Felipe, & Smale, Steve. 2007. Emergent behavior in flocks. *IEEE Transactions on automatic control*, **52**(5), 852–862.

- Dey, Abhijit, & Morrison, HF. 1979. Resistivity modelling for arbitrarily shaped two-dimensional structures. *Geophysical Prospecting*, **27**(1), 106–136.
- Doetsch, Joseph, Linde, Niklas, & Binley, Andrew. 2010. Structural joint inversion of time-lapse crosshole ERT and GPR traveltime data. *Geophysical Research Letters*, **37**(24).
- Dogan, Mine, Van Dam, Remke L, Bohling, Geoffrey C, Butler, James J, & Hyndman, David W. 2011. Hydrostratigraphic analysis of the MADE site with full-resolution GPR and direct-push hydraulic profiling. *Geophysical Research Letters*, **38**(6).
- Domenzain, Diego, Bradford, John, & Mead, Jodi. 2017. Imaging by joint inversion of electromagnetic waves and DC currents. In: *SIAM Mathematical and Computational issues in the Geosciences*.
- Domenzain, Diego, Bradford, John, & Mead, Jodi. 2019a. Joint inversion of full-waveform GPR and ER data. Part 1. *In review*.
- Domenzain, Diego, Bradford, John, & Mead, Jodi. 2019b. Joint inversion of full-waveform GPR and ER data. Part 2: enhancing low frequencies with the envelope transform and cross-gradients. *In review*.
- Ernst, Jacques R, Green, Alan G, Maurer, Hansruedi, & Holliger, Klaus. 2007a. Application of a new 2D time-domain full-waveform inversion scheme to crosshole radar data. *Geophysics*, **72**(5), J53–J64.
- Ernst, Jacques R, Maurer, Hansruedi, Green, Alan G, & Holliger, Klaus. 2007b. Full-waveform inversion of crosshole radar data based on 2-D finite-difference time-

- domain solutions of Maxwell's equations. *IEEE transactions on geoscience and remote sensing*, **45**(9), 2807–2828.
- Fikos, I, Vargemezis, G, Zlotnicki, Jacques, Puertollano, JR, Alanis, PB, Pigtain, RC, Villacorte, EU, Malipot, GA, & Sasai, Y. 2012. Electrical resistivity tomography study of Taal volcano hydrothermal system, Philippines. *Bulletin of Volcanology*, **74**(8), 1821–1831.
- Fregoso, Emilia, & Gallardo, Luis A. 2009. Cross-gradients joint 3D inversion with applications to gravity and magnetic data. *Geophysics*, **74**(4), L31–L42.
- Friel, Richard, & Or, Dani. 1999. Frequency analysis of time-domain reflectometry (TDR) with application to dielectric spectroscopy of soil constituents. *Geophysics*, **64**(3), 707–718.
- Gallardo, Luis A, & Meju, Max A. 2003. Characterization of heterogeneous near-surface materials by joint 2D inversion of dc resistivity and seismic data. *Geophysical Research Letters*, **30**(13).
- Gallardo, Luis A, & Meju, Max A. 2007. Joint two-dimensional cross-gradient imaging of magnetotelluric and seismic traveltimes for structural and lithological classification. *Geophysical Journal International*, **169**(3), 1261–1272.
- Ghose, R, & Slob, EC. 2006. Quantitative integration of seismic and GPR reflections to derive unique estimates for water saturation and porosity in subsoil. *Geophysical Research Letters*, **33**(5).
- Giannakis, Iraklis, Giannopoulos, Antonios, & Warren, Craig. 2015. A realistic FDTD numerical modeling framework of ground penetrating radar for landmine detection.

IEEE journal of selected topics in applied earth observations and remote sensing, **9**(1), 37–51.

Gross, L. 2019. Weighted Cross–Gradient Function for Joint Inversion with the Application to regional 3D Gravity and Magnetic Anomalies. *Geophysical Journal International*.

Gueting, Nils, Vienken, Thomas, Klotzsche, Anja, van der Kruk, Jan, Vanderborght, Jan, Caers, Jef, Vereecken, Harry, & Englert, Andreas. 2017. High resolution aquifer characterization using crosshole GPR full-waveform tomography: Comparison with direct-push and tracer test data. *Water Resources Research*, **53**(1), 49–72.

Günther, Thomas, Rücker, Carsten, & Spitzer, Klaus. 2006. Three-dimensional modelling and inversion of DC resistivity data incorporating topography—II. Inversion. *Geophysical Journal International*, **166**(2), 506–517.

Ha, Taeyoung, Pyun, Sukjoon, & Shin, Changsoo. 2006. Efficient electric resistivity inversion using adjoint state of mixed finite-element method for Poisson’s equation. *Journal of Computational Physics*, **214**(1), 171–186.

Haber, E, & Oldenburg, D. 1997. Joint inversion: a structural approach. *Inverse problems*, **13**(1), 63.

Haber, Eldad, & Gazit, Michal Holtzman. 2013. Model fusion and joint inversion. *Surveys in Geophysics*, **34**(5), 675–695.

Hauck, Christian, Mühll, Daniel Vonder, & Maurer, Hansruedi. 2003. Using DC resistivity tomography to detect and characterize mountain permafrost. *Geophysical prospecting*, **51**(4), 273–284.

- Hermans, Thomas, Vandenbohede, Alexander, Lebbe, Luc, & Nguyen, Frédéric. 2012. A shallow geothermal experiment in a sandy aquifer monitored using electric resistivity tomography. *Geophysics*, **77**(1), B11–B21.
- Hetrick, Hank, & Mead, Jodi. 2018. Geophysical imaging of subsurface structures with least squares estimates. *Inverse Problems in Science and Engineering*, 1–20.
- Holliger, K, Musil, M, & Maurer, HR. 2001. Ray-based amplitude tomography for crosshole georadar data: A numerical assessment. *Journal of Applied Geophysics*, **47**(3-4), 285–298.
- Hu, Wenyi, Abubakar, Aria, & Habashy, Tarek M. 2009. Joint electromagnetic and seismic inversion using structural constraints. *Geophysics*, **74**(6), R99–R109.
- Johnson, Timothy C, Routh, Partha S, Barrash, Warren, & Knoll, Michael D. 2007. A field comparison of Fresnel zone and ray-based GPR attenuation-difference tomography for time-lapse imaging of electrically anomalous tracer or contaminant plumes. *Geophysics*, **72**(2), G21–G29.
- Jomard, H, Lebourg, T, Guglielmi, Y, & Tric, Emmanuel. 2010. Electrical imaging of sliding geometry and fluids associated with a deep seated landslide (La Clapière, France). *Earth Surface Processes and Landforms: The Journal of the British Geomorphological Research Group*, **35**(5), 588–599.
- Kjær, Kurt H, Larsen, Nicolaj K, Binder, Tobias, Bjørk, Anders A, Eisen, Olaf, Fahnestock, Mark A, Funder, Svend, Garde, Adam A, Haack, Henning, Helm, Veit, *et al.* 2018. A large impact crater beneath Hiawatha Glacier in northwest Greenland. *Science advances*, **4**(11), eaar8173.

- Klotzsche, Anja, van der Kruk, Jan, Bradford, John, & Vereecken, Harry. 2014. Detection of spatially limited high-porosity layers using crosshole GPR signal analysis and full-waveform inversion. *Water Resources Research*, **50**(8), 6966–6985.
- Knight, Rosemary. 2001. Ground penetrating radar for environmental applications. *Annual Review of Earth and Planetary Sciences*, **29**(1), 229–255.
- Kurzmann, A, Przebindowska, A, Köhn, D, & Bohlen, T. 2013. Acoustic full waveform tomography in the presence of attenuation: a sensitivity analysis. *Geophysical Journal International*, **195**(2), 985–1000.
- Lavoué, Francois, Brossier, Romain, Métivier, Ludovic, Garambois, Stéphane, & Virieux, Jean. 2014. Two-dimensional permittivity and conductivity imaging by full waveform inversion of multioffset GPR data: A frequency-domain quasi-Newton approach. *Geophysical Journal International*, **197**(1), 248–268.
- Linde, Niklas, & Vrugt, Jasper A. 2013. Distributed soil moisture from crosshole ground-penetrating radar travel times using stochastic inversion. *Vadose Zone Journal*, **12**(1).
- Linde, Niklas, Binley, Andrew, Tryggvason, Ari, Pedersen, Laust B, & Revil, Andre. 2006. Improved hydrogeophysical characterization using joint inversion of cross-hole electrical resistance and ground-penetrating radar traveltimes data. *Water Resources Research*, **42**(12).
- Liu, Zhiyang, & Zhang, Jie. 2017. Joint traveltimes and waveform envelope inversion for near-surface imaging. *Pure and Applied Geophysics*, **174**(3), 1269–1289.

- Loewer, M, Günther, T, Igel, J, Kruschwitz, Sabine, Martin, T, & Wagner, N. 2017. Ultra-broad-band electrical spectroscopy of soils and sediments—A combined permittivity and conductivity model. *Geophysical Journal International*, **210**(3), 1360–1373.
- Loke, Meng Heng, & Barker, RD. 1996. Rapid least-squares inversion of apparent resistivity pseudosections by a quasi-Newton method 1. *Geophysical prospecting*, **44**(1), 131–152.
- Marescot, Laurent, Lopes, Sérgio Palma, Rigobert, Stéphane, & Green, Alan G. 2008. Nonlinear inversion of geoelectric data acquired across 3D objects using a finite-element approach. *Geophysics*, **73**(3), F121–F133.
- Meles, Giovanni, Greenhalgh, Stewart, Van der Kruk, Jan, Green, Alan, & Maurer, Hansruedi. 2012. Taming the non-linearity problem in GPR full-waveform inversion for high contrast media. *Journal of Applied Geophysics*, **78**, 31–43.
- Meles, Giovanni Angelo, Van der Kruk, Jan, Greenhalgh, Stewart A, Ernst, Jacques R, Maurer, Hansruedi, & Green, Alan G. 2010. A new vector waveform inversion algorithm for simultaneous updating of conductivity and permittivity parameters from combination crosshole/borehole-to-surface GPR data. *IEEE Transactions on geoscience and remote sensing*, **48**(9), 3391–3407.
- Mikesell, Dylan, van Wijk, Kasper, Calvert, Alexander, & Haney, Matt. 2009. The virtual refraction: Useful spurious energy in seismic interferometry. *Geophysics*, **74**(3), A13–A17.
- Moorkamp, Max. 2017. Integrating electromagnetic data with other geophysical ob-

- servations for enhanced imaging of the earth: a tutorial and review. *Surveys in Geophysics*, **38**(5), 935–962.
- Mwenifumbo, C Jonathan, Barrash, Warren, & Knoll, Michael D. 2009. Capacitive conductivity logging and electrical stratigraphy in a high-resistivity aquifer, Boise Hydrogeophysical Research Site. *Geophysics*, **74**(3), E125–E133.
- Ogunbo, Jide Nosakare, Marquis, Guy, Zhang, Jie, & Wang, Weizhong. 2018. Joint inversion of seismic traveltimes and frequency-domain airborne electromagnetic data for hydrocarbon exploration. *Geophysics*, **83**(2), U9–U22.
- Oldenborger, Greg A, Routh, Partha S, & Knoll, Michael D. 2007. Model reliability for 3D electrical resistivity tomography: Application of the volume of investigation index to a time-lapse monitoring experiment. *Geophysics*, **72**(4), F167–F175.
- Oldenburg, Douglas W, & Li, Yaoguo. 1999. Estimating depth of investigation in dc resistivity and IP surveys. *Geophysics*, **64**(2), 403–416.
- Parsekian, Andrew D, Slater, Lee, & Giménez, Daniel. 2012. Application of ground-penetrating radar to measure near-saturation soil water content in peat soils. *Water Resources Research*, **48**(2).
- Perrone, A, Lapenna, V, & Piscitelli, S. 2014. Electrical resistivity tomography technique for landslide investigation: A review. *Earth-Science Reviews*, **135**, 65–82.
- Pica, A, Diet, JP, & Tarantola, A. 1990. Nonlinear inversion of seismic reflection data in a laterally invariant medium. *Geophysics*, **55**(3), 284–292.
- Pidlisecky, Adam, & Knight, Rosemary. 2008. FW2_5D: A MATLAB 2.5-D electrical resistivity modeling code. *Computers & Geosciences*, **34**(12), 1645–1654.

- Pidlisecky, Adam, Haber, Eldad, & Knight, Rosemary. 2007. RESINVM3D: A 3D resistivity inversion package. *Geophysics*, **72**(2), H1–H10.
- Pratt, R Gerhard, Shin, Changsoo, & Hick, GJ. 1998. Gauss–Newton and full Newton methods in frequency–space seismic waveform inversion. *Geophysical Journal International*, **133**(2), 341–362.
- Rödder, Tobias, & Kneisel, Christof. 2012. Permafrost mapping using quasi-3D resistivity imaging, Murtèl, Swiss Alps. *Near Surface Geophysics*, **10**(2), 117–127.
- Rumelhart, David E, Hinton, Geoffrey E, & Williams, Ronald J. 1986. Learning representations by back-propagating errors. *nature*, **323**(6088), 533.
- Scapozza, Cristian, Lambiel, Christophe, Baron, Ludovic, Marescot, Laurent, & Reynard, Emmanuel. 2011. Internal structure and permafrost distribution in two alpine periglacial talus slopes, Valais, Swiss Alps. *Geomorphology*, **132**(3-4), 208–221.
- Schmid, Lino, Heilig, Achim, Mitterer, Christoph, Schweizer, Jürg, Maurer, Hansruedi, Okorn, Robert, & Eisen, Olaf. 2014. Continuous snowpack monitoring using upward-looking ground-penetrating radar technology. *Journal of Glaciology*, **60**(221), 509–525.
- Snieder, Roel, Wapenaar, Kees, & Wegler, Ulrich. 2007. Unified Green’s function retrieval by cross-correlation; connection with energy principles. *Physical Review E*, **75**(3), 036103.
- Sold, Leo, Huss, Matthias, Hoelzle, Martin, Anderegg, Hubert, Joerg, Philip C, & Zemp, Michael. 2013. Methodological approaches to infer end-of-winter snow distribution on alpine glaciers. *Journal of Glaciology*, **59**(218), 1047–1059.

- Spichak, Viacheslav V, & Zakharova, Olga K. 2015. *Electromagnetic geothermometry*. Elsevier.
- Spitzer, Klaus. 1998. The three-dimensional DC sensitivity for surface and subsurface sources. *Geophysical Journal International*, **134**(3), 736–746.
- Taherian, MR, Kenyon, WE, & Safinya, KA. 1990. Measurement of dielectric response of water-saturated rocks. *Geophysics*, **55**(12), 1530–1541.
- Taillandier, Cédric, Noble, Mark, Chauris, Hervé, & Calandra, Henri. 2009. First-arrival traveltime tomography based on the adjoint-state method. *Geophysics*, **74**(6), WCB1–WCB10.
- Tarantola, Albert. 1984. Inversion of seismic reflection data in the acoustic approximation. *Geophysics*, **49**(8), 1259–1266.
- Virieux, Jean, & Operto, Stéphane. 2009. An overview of full-waveform inversion in exploration geophysics. *Geophysics*, **74**(6), WCC1–WCC26.
- Wright, Stephen, & Nocedal, Jorge. 1999. Numerical optimization. *Springer Science*, **35**(67-68), 7.
- Xue, Zhiguang, Sun, Junzhe, Fomel, Sergey, & Zhu, Tieyuan. 2017. Accelerating full-waveform inversion with attenuation compensation. *Geophysics*, **83**(1), A13–A20.
- Yee, Kane. 1966. Numerical solution of initial boundary value problems involving Maxwell's equations in isotropic media. *IEEE Transactions on antennas and propagation*, **14**(3), 302–307.

Zhu, Tieyuan, & Harris, Jerry M. 2014. Modeling acoustic wave propagation in heterogeneous attenuating media using decoupled fractional Laplacians. *Geophysics*, **79**(3), T105–T116.

Appendices

APPENDIX A: OPTIMALLY PERTURBING

Given a descent direction, finding the right step size is equivalent to traversing the objective function hyper-surface in the direction of the gradient ($-a \mathbf{g}_\varepsilon$) starting from our current value of $\boldsymbol{\varepsilon}$ and finding the value $a = \alpha_\varepsilon$ which minimizes the objective function (Wright & Nocedal, 1999). Traversing the objective function hyper-surface is done by perturbing the current value for $\boldsymbol{\varepsilon}$ with a collection of real numbers a_i . In equation 3.11 we used the notation $a_i = p_i \kappa_\varepsilon$ and gave empirical values for p_i . In this section we find κ_ε .

To speed-up convergence but maintain stability we perform a descending search for κ_ε . We start with a large value of κ_ε and compute the perturbation $\hat{\boldsymbol{\varepsilon}}$,

$$\hat{\boldsymbol{\varepsilon}} = \boldsymbol{\varepsilon} \odot \exp(-\boldsymbol{\varepsilon} \odot \kappa_\varepsilon \mathbf{g}_\varepsilon). \quad (\text{A.1})$$

We then check if the minimum and maximum value of $\hat{\boldsymbol{\varepsilon}}$ lie within our stability velocity region: if they do we have found κ_ε , if they do not we decrease κ_ε until they do. In practice once we have found a value of κ_ε that lies within our stability region, we repeat the search with finer ascending values of κ_ε to make sure $\hat{\boldsymbol{\varepsilon}}$ is as snug as possible in our velocity interval.

APPENDIX B:
ER GRADIENT

Taking the derivative with respect to $\boldsymbol{\sigma}$ and using the chain rule on the ER objective function for one source location,

$$\Theta_{dc}^s(\boldsymbol{\sigma}; \mathbf{s}_{dc}, \mathbf{d}_{dc}^{o,s}) = \frac{\|\mathbf{d}_{dc}^s - \mathbf{d}_{dc}^{o,s}\|_2^2}{\|\mathbf{d}_{dc}^{o,s}\|_2^2}, \quad (\text{B.1})$$

we have,

$$\nabla_{\boldsymbol{\sigma}} \Theta_{dc}^s = \nabla_{\mathbf{d}_{dc}} \Theta_{dc}^s \cdot \nabla_{\boldsymbol{\sigma}} \mathbf{d}_{dc}^s, \quad (\text{B.2})$$

where $\nabla_{\boldsymbol{\sigma}} \Theta_{dc}^s$ and $\nabla_{\mathbf{d}_{dc}} \Theta_{dc}^s$ are vectors of size $1 \times n_x n_z$ and $1 \times n_{\mathbf{d}_{dc}^s}$ respectively (where $n_{\mathbf{d}_{dc}^s}$ is the number of entries in the data) and $\nabla_{\boldsymbol{\sigma}} \mathbf{d}_{dc}$ is the Jacobian \mathbf{J}_{dc} of \mathbf{d}_{dc} , a matrix of size $n_{\mathbf{d}_{dc}^s} \times n_x n_z$. Because of our choice of Θ_{dc}^s to be the sum of square errors, $\nabla_{\mathbf{d}_{dc}} \Theta_{dc}^s$ is equal to \mathbf{e}_{dc}^\top . We make the convention of calling \mathbf{g}_{dc} the vertical vector whose entries are the partial derivatives of Θ_{dc}^s with respect to $\boldsymbol{\sigma}$, i.e. $\mathbf{g}_{dc} = (\nabla_{\boldsymbol{\sigma}} \Theta_{dc}^s)^\top$. We now take the transpose of equation B.2,

$$\mathbf{g}_{dc} = \mathbf{J}_{dc}^\top \mathbf{e}_{dc}. \quad (\text{B.3})$$

Our task will be to find a different expression for the right-hand side of equation B.3, (Domenzain *et al.*, 2017; Pratt *et al.*, 1998).

Using the product rule on equation 3.16, we have

$$\mathbf{L}_{dc} \nabla_{\boldsymbol{\sigma}} \boldsymbol{\varphi} + (\nabla_{\boldsymbol{\sigma}} \mathbf{L}_{dc}) \boldsymbol{\varphi} = 0. \quad (\text{B.4})$$

We now transpose equation B.4,

$$(\nabla_{\boldsymbol{\sigma}} \boldsymbol{\varphi})^\top \mathbf{L}_{dc}^\top = \mathbf{S}_{dc}, \quad (\text{B.5})$$

where $\mathbf{S}_{dc} = -((\nabla_\sigma \mathbf{L}_{dc})\boldsymbol{\varphi})^\top$ is a matrix of size $n_x n_z \times n_x n_z$ whose entries are explicitly calculated as a function of $\boldsymbol{\sigma}$, the spacial discretization and $\boldsymbol{\varphi}$. We define the adjoint field \mathbf{v}_{dc} to satisfy,

$$\mathbf{L}_{dc}^\top \mathbf{v}_{dc} = \mathbf{M}_{dc}^\top \mathbf{e}_{dc}, \quad (\text{B.6})$$

and multiply equation B.5 on the right side by \mathbf{v}_{dc} ,

$$\begin{aligned} (\nabla_\sigma \boldsymbol{\varphi})^\top \mathbf{L}_{dc}^\top \mathbf{v}_{dc} &= \mathbf{S}_{dc} \mathbf{v}_{dc}, \\ (\nabla_\sigma \boldsymbol{\varphi})^\top \mathbf{M}_{dc}^\top \mathbf{e}_{dc} &= \mathbf{S}_{dc} \mathbf{v}_{dc}, \\ (\nabla_\sigma \mathbf{d}_{dc}^s)^\top \mathbf{e}_{dc} &= \mathbf{S}_{dc} \mathbf{v}_{dc}, \\ \mathbf{J}_{dc}^\top \mathbf{e}_{dc} &= \mathbf{S}_{dc} \mathbf{v}_{dc}, \end{aligned} \quad (\text{B.7})$$

where in the second to last equality we have used $\nabla_\sigma \mathbf{d}_{dc}^s = \mathbf{M}_{dc} \nabla_\sigma \boldsymbol{\varphi}$. Finally we write,

$$\mathbf{g}_{dc} = \mathbf{S}_{dc} \mathbf{v}_{dc}. \quad (\text{B.8})$$

We note that this approach is similar to Pidlisecky *et al.* (2007), although we have explicitly written an expression for \mathbf{L}_{dc} and \mathbf{S}_{dc} entry by entry rather than as a multiplication of discretized differential operators, which yields full rank on \mathbf{L}_{dc} and \mathbf{S}_{dc} because of the used boundary conditions.

APPENDIX C:
ENVELOPE GPR GRADIENT

In order to apply the FWI scheme with the modified envelope data, we first need to deduce a new adjoint source as a result of the chain rule on our objective function. We follow Bozdağ *et al.* (2011) and define the adjoint source of equation 3.6 in the continuous case and then bring it back to the discrete case. Let u denote the y component of the electromagnetic wavefield defined in space and time for a given source. We denote the analytical representation of u by,

$$\tilde{u} = u + i\hat{u}, \quad (\text{C.1})$$

where the hat denotes the Hilbert transform of u . We will also refer to the Hilbert transform of u by $\{u\}_H$. We will modify the objective function Θ_w , and that will modify the adjoint source because of the chain rule on Θ_w .

The instantaneous amplitude of the wavefield (i.e. envelope) is,

$$u_a = \sqrt{u^2 + \hat{u}^2}. \quad (\text{C.2})$$

In what follows we will define new objective functions and find the new adjoint source for them. We will denote d_u the derivative with respect to u and use this identity derived from the definition of the Hilbert transform,

$$\int f \cdot d_u \hat{g} \, dt = - \int \hat{f} \cdot d_u g \, dt. \quad (\text{C.3})$$

Let the instantaneous amplitude objective function be,

$$\Theta_{w,a} = \frac{1}{2} \int_0^T e_{w,a}^2 \, dt, \quad e_{w,a} = u_a - u_a^o, \quad (\text{C.4})$$

where the superscript o denotes observed data. We need the derivative of $\Theta_{w,a}$ with respect to the parameters, and for that we also need $d_u \Theta_{w,a}$ since u depends on the parameters. We have,

$$\begin{aligned} d_u \Theta_{w,a} &= \int_0^T e_{w,a} \cdot d_u e_{w,a} dt, \\ d_u e_{w,a} &= d_u u_a, \\ &= \frac{u + \hat{u} \cdot d_u \hat{u}}{u_a^2}. \end{aligned} \tag{C.5}$$

We now invoke identity C.3 in $d_u \Theta_{w,a}$,

$$d_u \Theta_{w,a} = \int_0^T \underbrace{\frac{e_{w,a} \cdot u}{u_a} - \left\{ \frac{e_{w,a} \cdot \hat{u}}{u_a} \right\}_H}_{\text{adjoint source}} dt. \tag{C.6}$$

From equation C.6 we have that in the discrete case for an observed shot-gather $\mathbf{d}_w^{o,s}$ the adjoint source for the envelope transformed data is,

$$\mathbf{s}_{w,a} = \frac{\mathbf{e}_{w,a} \cdot \mathbf{d}_w^{o,s}}{\mathbf{d}_{w,a}^{o,s}} - \left\{ \frac{\mathbf{e}_{w,a} \cdot \{\mathbf{d}_w^{o,s}\}_H}{\mathbf{d}_{w,a}^{o,s}} \right\}_H, \tag{C.7}$$

where $\mathbf{d}_{w,a}^{o,s}$ denotes the envelope of the observed data and $\mathbf{e}_{w,a}$ denotes the residual of the observed envelope data and the synthetic envelope data. The gradients $\mathbf{g}_{\sigma,a}$ and $\mathbf{g}_{\varepsilon,a}$ are,

$$\mathbf{v}_w = \mathbf{L}_w \mathbf{s}_{w,a}(-t), \tag{C.8}$$

$$\mathbf{g}_{\sigma,a} = - \sum_t \mathbf{u}(-t) \odot \mathbf{v}_w(t) \cdot \Delta t, \tag{C.9}$$

$$\mathbf{g}_{\varepsilon,a} = - \sum_t \dot{\mathbf{u}}(-t) \odot \mathbf{v}_w(t) \cdot \Delta t. \tag{C.10}$$

APPENDIX D:
MINIMIZING Θ_τ

We present a Gauss-Newton algorithm for optimizing Θ_τ that enables our joint inversion scheme to independently weigh the structure of $\boldsymbol{\sigma}$ over $\boldsymbol{\varepsilon}$ (or vice-versa).

Let \mathbf{D}_x and \mathbf{D}_z be the discretized differential operators in the x and z directions written as matrixies of size $n_x n_z \times n_x n_z$,

$$\tau = \mathbf{D}_x \boldsymbol{\varepsilon} \odot \mathbf{D}_z \boldsymbol{\sigma} - \mathbf{D}_z \boldsymbol{\varepsilon} \odot \mathbf{D}_x \boldsymbol{\sigma}. \quad (\text{D.1})$$

The derivatives of τ with respect to $\boldsymbol{\varepsilon}$ and $\boldsymbol{\sigma}$ are,

$$\begin{aligned} \nabla_{\boldsymbol{\varepsilon}} \tau &= \mathbf{D}_x \odot [\mathbf{D}_z \boldsymbol{\sigma}] - \mathbf{D}_z \odot [\mathbf{D}_x \boldsymbol{\sigma}], \\ \nabla_{\boldsymbol{\sigma}} \tau &= \mathbf{D}_z \odot [\mathbf{D}_x \boldsymbol{\varepsilon}] - \mathbf{D}_x \odot [\mathbf{D}_z \boldsymbol{\varepsilon}], \end{aligned} \quad (\text{D.2})$$

where brackets indicate a matrix of size $n_x n_z \times n_x n_z$ and all columns of a matrix $[\mathbf{a}]$ are the column vector \mathbf{a} . Let $\mathbf{J}_{\tau,\circ}^\top = \nabla_{\circ} \tau$, then the gradients of Θ_τ are,

$$\begin{aligned} \mathbf{g}_{\tau,\varepsilon} &= \mathbf{J}_{\tau,\varepsilon} \tau, \\ \mathbf{g}_{\tau,\sigma} &= \mathbf{J}_{\tau,\sigma} \tau. \end{aligned} \quad (\text{D.3})$$

We compute the updates of $\boldsymbol{\varepsilon}$ and $\boldsymbol{\sigma}$ by,

$$\begin{aligned} \Delta \boldsymbol{\varepsilon}_\tau &= -(\mathbf{J}_{\tau,\varepsilon} \mathbf{J}_{\tau,\varepsilon}^\top + \alpha_{\tau,\varepsilon} \mathbf{I})^{-1} \mathbf{g}_{\tau,\varepsilon}, \\ \Delta \boldsymbol{\sigma}_\tau &= -(\mathbf{J}_{\tau,\sigma} \mathbf{J}_{\tau,\sigma}^\top + \alpha_{\tau,\sigma} \mathbf{I})^{-1} \mathbf{g}_{\tau,\sigma}, \end{aligned} \quad (\text{D.4})$$

where \mathbf{I} is the identity matrix of size $n_x n_z \times n_x n_z$, and $\alpha_{\tau,\varepsilon}$ and $\alpha_{\tau,\sigma}$ are step-sizes for the optimal descent direction for the previous iteration gradients and are computed with an n-point parabola approximation. We then normalize the updates by their largest amplitude and scale them with their respective current step-sizes. At each

iteration, either $\boldsymbol{\varepsilon}$ and $\boldsymbol{\sigma}$ are updated by,

$$\begin{aligned}\boldsymbol{\varepsilon} &\leftarrow \boldsymbol{\varepsilon} + \Delta\boldsymbol{\varepsilon}_\tau, \\ \boldsymbol{\sigma} &\leftarrow \boldsymbol{\sigma} + \Delta\boldsymbol{\sigma}_\tau.\end{aligned}\tag{D.5}$$

In order to control the weigh of either structures $\boldsymbol{\varepsilon}$ or $\boldsymbol{\sigma}$ in our joint inversion, at each iteration we store the update information of $\Delta\boldsymbol{\varepsilon}_\tau$ and $\Delta\boldsymbol{\sigma}_\tau$ in the *master* updates $\Delta\boldsymbol{\varepsilon}_{\tau,o}$ and $\Delta\boldsymbol{\sigma}_{\tau,o}$,

$$\Delta\boldsymbol{\varepsilon}_{\tau,o} \leftarrow \Delta\boldsymbol{\varepsilon}_{\tau,o} + \Delta\boldsymbol{\varepsilon}_\tau,\tag{D.6}$$

$$\Delta\boldsymbol{\sigma}_{\tau,o} \leftarrow \Delta\boldsymbol{\sigma}_{\tau,o} + \Delta\boldsymbol{\sigma}_\tau.\tag{D.7}$$

We note that in our inversion scheme presented in the section **Joint inversion with cross-gradients** we first optimize Θ_τ modifying $\boldsymbol{\sigma}$ and keeping $\boldsymbol{\varepsilon}$ fixed, and then we optimize Θ_τ modifying $\boldsymbol{\varepsilon}$ and keeping $\boldsymbol{\sigma}$ fixed.

APPENDIX E:
INITIAL MODELS FOR THE SYNTHETIC
ALLUVIAL AQUIFER

For the first initial model (see Figure E.1-**a**), we smooth the true permittivity with a low-pass gaussian filter as to only allow two characteristic wavelengths in the space-frequency domain (a gaussian with a half-width of 0.8 1/m). For the second initial model (see Figure E.1-**b**), we first remove the top layer from the true permittivity model, we then smooth analogously as for the first initial model, and then we return the first layer without smoothing. In order to keep the location of the shallow reflector equal in both initial permittivity and conductivity, we interpolate permittivities to obtain Figure E.1-**c** and Figure E.1-**d**.

Two main differences between the first and second initial models are that the first initial model does not have an accurate amplitude in the first layer and does not follow the low velocity region in length. As a result, when compared to the inversions of the first initial model (Figures E.1-**e** and **g**), the second model is visibly able to resolve all layers in the model with minimal artifacts in the first layer (Figures E.1-**f** and **h**). We note however, that the first initial model is able to correctly identify the location of the first-second layer boundary.

We choose the initial model for the inversions presented in the main text as a perturbed true model between the two initial models presented in this Appendix. First we remove the top layer from the true permittivity model, and then smooth with a low-pass gaussian filter as to only allow two characteristic wavelengths in the space-frequency domain (a gaussian with a half-width of 0.8 1/m). Then we decrease the values by 4% of the true values, return the first layer and smooth again as to only allow six characteristic wavelengths in the space-frequency domain (a gaussian with a half-width of 2.5 1/m). The initial model for the conductivity is achieved by interpolation of the permittivity. The result is a smooth initial model with values 4%

less than the true model but with a not-so-smooth first layer interface.

Such a smooth initial velocity model can be achieved by following the inversion procedure of Bradford *et al.* (2009b). This method for estimating an initial velocity model is robust when air-wave refractions are present in the data, and resolves the subsurface in a top-down approach. We conclude that if the GPR field data exhibits air-wave refractions, the better the initial model fits these events in the data, the better the inversion results will be.

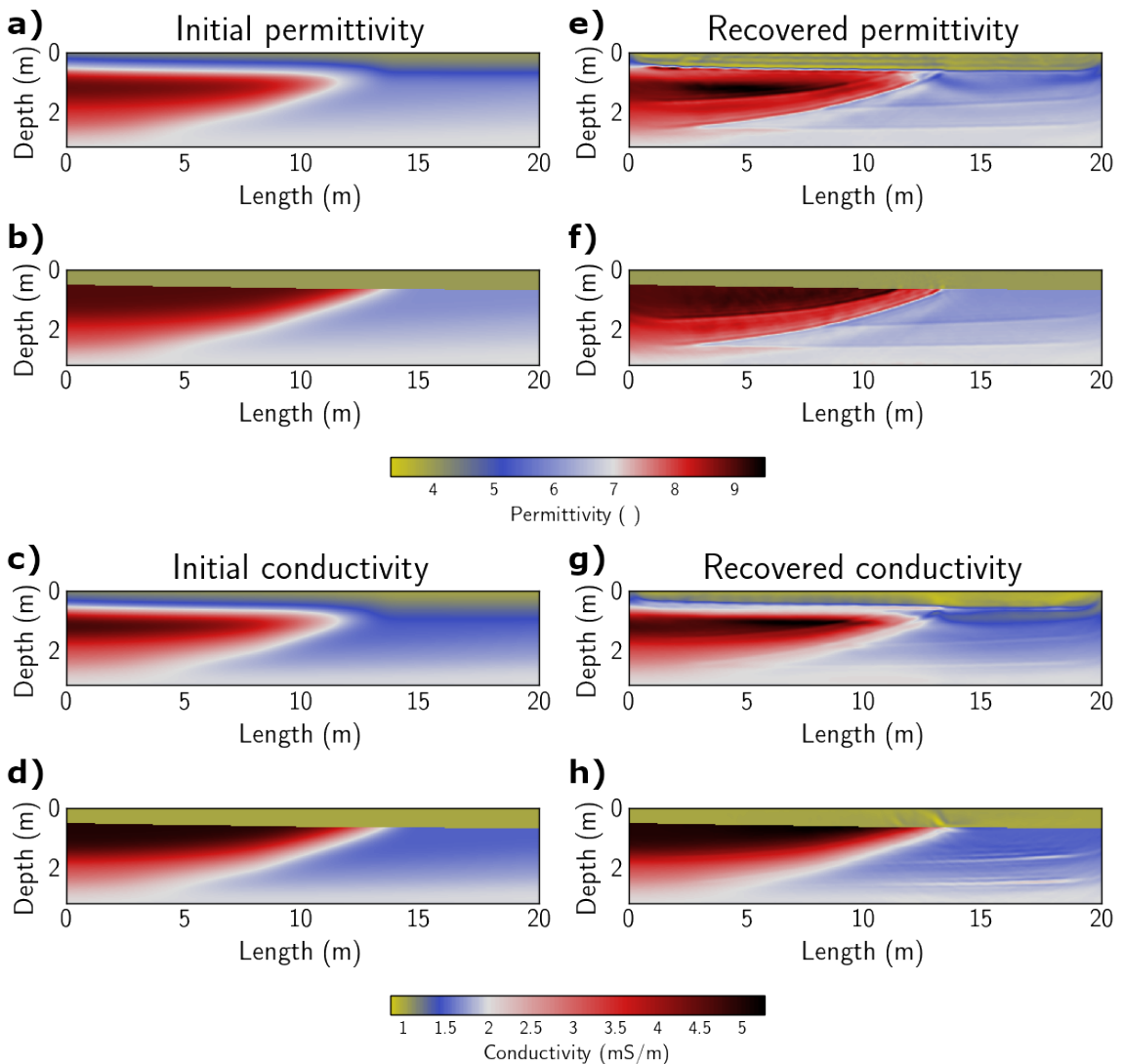


Figure E.1: Sensitivity analysis of the initial model for the synthetic alluvial aquifer. In a), b), c) and d) we have the first and second initial model for permittivity and conductivity. In e), f), g) and h) we have their respective recovered parameters by using the JOIX method.

APPENDIX F:
FOURIER COEFFICIENTS FOR 2.5D
TRANSFORM

In order to solve equation 5.14 we must find weights \mathbf{k} and $\boldsymbol{\omega}$ to accurately approximate the integral in equation 5.11. We follow Pidlisecky & Knight (2008) and note that the Green's function solution for homogeneous σ of equation 5.9 on the half xz -plane is,

$$\varphi(x, y = 0, z) = \frac{\mathbf{i}}{2\pi\sigma} \underbrace{\left(\underbrace{\frac{1}{\|x - s_+\|_2}}_{r_+} - \underbrace{\frac{1}{\|x - s_-\|_2}}_{r_-} \right)}_{1/R}. \quad (\text{F.1})$$

Applying the forward Fourier-cosine transform,

$$\tilde{\varphi} = \int_0^\infty \varphi \cos(y k_y) dy = \frac{\mathbf{i}}{2\pi\sigma} (B_o(k_y r_+) - B_o(k_y r_-)), \quad (\text{F.2})$$

where B_o is the zero order modified Bessel function of the second kind. By plugging in equations F.1 and F.2 into equation 5.14 we discretize by

$$\begin{aligned} 1 &\approx \sum_j \underbrace{\frac{2R}{\pi} \{B_o(k_j r_+) - B_o(k_j r_-)\}}_{K_{ij}} \omega_j \\ \mathbf{K} &= \frac{2R}{\pi} \{B_o(\mathbf{k} r_+) - B_o(\mathbf{k} r_-)\} \\ \mathbf{f} &\approx \mathbf{K}\boldsymbol{\omega}, \end{aligned} \quad (\text{F.3})$$

where $\mathbf{K} = \mathbf{K}(\mathbf{k}, \mathbf{s})$ is a matrix of size $n_R \times n_k$, n_R and n_k are the size of R and \mathbf{k} respectively, \mathbf{f} is a vector of length n_R whose entries should approximate 1, and $\mathbf{k} = (k_{yi})$, $\boldsymbol{\omega} = (\omega_i)$ are vectors of length n_k . We minimize

$$\Phi(\mathbf{k}) = \|\mathbf{1} - \underbrace{\mathbf{K} \underbrace{(\mathbf{K}^\top \mathbf{K})^{-1} \mathbf{K}^\top}_{\boldsymbol{\omega}}}_{\mathbf{f}(\mathbf{k})} \mathbf{f}(\mathbf{k})\|_2^2 = \|\mathbf{1} - \mathbf{f}(\mathbf{k})\|_2^2, \quad (\text{F.4})$$

ER 2.5d \mathbf{k} and $\boldsymbol{\omega}$ computation

1. initial guess for $\mathbf{k} = (n_k \text{ real numbers}) \cdot \Delta x$,
2. build $\mathbf{K}(\mathbf{k}, \mathbf{s})$,
3. $\mathbf{f} \leftarrow \mathbf{K}(\mathbf{K}^\top \mathbf{K})^{-1} \mathbf{K}^\top \cdot \mathbf{1}$,
4. compute $\mathbf{J} = \nabla_{\mathbf{k}} \mathbf{f}$ using n_k finite differences,
5. $\nabla_{\mathbf{k}} \Phi^\top \leftarrow \mathbf{J}^\top (\mathbf{1} - \mathbf{f}) + \beta \mathbf{k}$ for a fixed real number β ,
6. $\Delta \mathbf{k} = (\mathbf{J}^\top \mathbf{J} + \beta \mathbf{I})^{-1} \cdot \nabla_{\mathbf{k}} \Phi^\top$,
7. $\mathbf{k} \leftarrow \mathbf{k} + \alpha \Delta \mathbf{k}$ for a fixed real number α ,
8. build $\mathbf{K}(\mathbf{k}, \mathbf{s})$
9. check if \mathbf{f} is almost $\mathbf{1}$,
10. repeat 3–9,
11. $\boldsymbol{\omega} = (\mathbf{K}^\top \mathbf{K})^{-1} \mathbf{K}^\top \cdot \mathbf{1}$,
12. return \mathbf{k} and $\frac{2}{\pi} \boldsymbol{\omega}$.

Figure F.1: Algorithm for finding the 2.5D transformatin weights $\boldsymbol{\omega}$.

using a regularized Newton method. The vector of all ones is denoted $\mathbf{1}$. Note that both \mathbf{k} and $\boldsymbol{\omega}$ are geometry dependent and not parameter dependent. Lastly, we follow Pidlisecky & Knight (2008) and use a small number for n_k , usually $n_k = 4$. Figure gives the full optimization algorithm (Pidlisecky & Knight, 2008) for computing \mathbf{k} and $\boldsymbol{\omega}$.